

AD-770 601

**CATALYTIC BEHAVIOR IN COMPOSITE SOLID
PROPELLANT COMBUSTION**

Warren C. Strahle, et al

Georgia Institute of Technology

Prepared for:

Office of Naval Research

1 November 1973

DISTRIBUTED BY:

NTIS

**National Technical Information Service
U. S. DEPARTMENT OF COMMERCE
5285 Port Royal Road, Springfield Va. 22151**

Unclassified
Security Classification

AD-770601

DOCUMENT CONTROL DATA - R & D

(Security classification of title, body of abstract and indexing annotation must be entered when the overall report is classified)

ORIGINATING ACTIVITY (Corporate author)

Georgia Institute of Technology
Atlanta, Georgia 30332

22. REPORT SECURITY CLASSIFICATION

Unclassified

23. GROUP

1. REPORT TITLE

Catalytic Behavior in Composite Solid Propellant Combustion

4. DESCRIPTIVE NOTES (Type of report and inclusive dates)

Annual Summary September 1, 1972 - August 31, 1973

7. AUTHOR(S) (First name, middle initial, last name)

Warren C. Strahle, John C. Handley, Narendra Kumar

8. REPORT DATE

November 1, 1973

79. TOTAL NO OF PAGES

~~130~~ 135

78. NO OF REFS

11

12. CONTRACT OR GRANT NO

N00014-67-A-0159-0016

6. PROJECT NO

99. ORIGINATOR'S REPORT NUMBER(S)

c.

98. OTHER REPORT NO(S) (Any other numbers that may be assigned this report)

d.

10. DISTRIBUTION STATEMENT

Approved for public release; distribution unlimited

11. SUPPLEMENTARY NOTES

13. SPONSORING MILITARY ACTIVITY

Office of Naval Research
Arlington, Virginia 22217

14. ABSTRACT

This report describes experiments and theoretical analysis concerned with sandwich combustion. The ingredients used in the experiment are compacted polycrystalline ammonium perchlorate as the oxidizer, hydroxyl terminated polybutadiene as the binder and four catalysts: Harshaw catalyst CU-0202, Fe₂O₃, ferrocene, and iron blue. The pressure range studied is 600-2000 psia. The experimental techniques used are cinephoto-macrography for sample observation during burning and burn rate determination, scanning electron microscopy for observation of quenched samples, and electron microprobing for an exploratory study of surface composition. A theoretical solution to a simple sandwich deflagration problem is attained. The probable sites of catalytic activity are determined, results are compared with actual propellant experience, and the analysis is used to clarify experimental results.

Reproduced by
NATIONAL TECHNICAL
INFORMATION SERVICE
U.S. Department of Commerce
Springfield VA 22151

DD FORM 1473
1 NOV 68

Unclassified
Security Classification

135

14. KEY WORDS	LINK A		LINK B		LINK C	
	ROLE	WT	ROLE	WT	ROLE	WT
Combustion						
Solid Propellants						
Catalysts						
Theoretical Analysis						
Scanning Electron Microscope						
Cinephotomacrography						
Electron Microprobe						
Ammonium Perchlorate						
Hydroxyl terminated Polybutadiene						

ia

CATALYTIC BEHAVIOR IN
SOLID PROPELLANT COMBUSTION

W. C. Strahle
J. C. Handley
N. Kumar

November 1, 1973

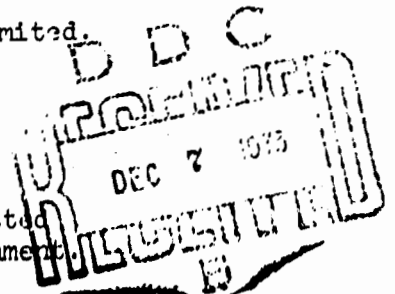
Details of illustrations in
this document may be better
studied on microfiche

Annual Summary Report - Research Sponsored by
The Office of Naval Research

ONR Contract No. N00014-67-A-0159-0016
Requisition Purchase Request NR 092-543

Approved for Public Release; Distribution Unlimited.

Reproduction in whole or in part is permitted
for any purpose of the United States Government



ib

ABSTRACT

This report describes experiments and theoretical analysis concerned with sandwich combustion. The ingredients used in the experiment are compacted polycrystalline ammonium perchlorate as the oxidizer, hydroxyl terminated polybutadiene as the binder and four catalysts: Harshaw catalyst CU-0202, Fe_2O_3 , ferrocene, and iron blue. The pressure range studied is 600-2000 psia. The experimental techniques used are cinephotomacrography for sample observation during burning and burn rate determination, scanning electron microscopy for observation of quenched samples, and electron microprobing for an exploratory study of surface composition. A theoretical solution to a simple sandwich deflagration problem is attained. The probable sites of catalytic activity are determined, results are compared with actual propellant experience, and the analysis is used to clarify experimental results.

TABLE OF CONTENTS

	<u>Page</u>
ABSTRACT	ii
CHAPTERS	
I. Introduction	1
II. Cinephotomacrography with Iron Blue and Ferrocene	3
III. Scanning Electron Microscopy with Four Catalysts	13
IV. Electron Microprobe Exploratory Studies	69
V. Relevance of Sandwich Results to Composite Propellant Behavior	75
VI. Sandwich Analysis	80
VII. Conclusions	111
REFERENCES	114
APPENDIX A	
Catalysts Located at the Binder-Oxidizer Interface	115

I. INTRODUCTION

Under a previous contract NO0123-72-C-242 to the Naval Weapons Center, China Lake, California, a study was initiated of sandwich combustion when catalysts were present in sandwiches. The results are described in Reference (1). The sandwiches used compacted polycrystalline ammonium perchlorate (AP) as the oxidizer, hydroxyl terminated polybutadiene (HTPB) as the binder, and the catalysts Harshaw Catalyst CU-0202 (CC) and Fe_2O_3 (IO). The pressure range studied was 600-3200 psia and catalytic effects were studied when the catalyst was placed in either the AP, the binder, or along the binder-AP interface. The technique used was cinephotomacrography for sample observation during burn and for burn rate determination. This work was an outgrowth of the work of Reference (2), using the same ingredients but CTPB binder.

The results of the previous program indicated that at all pressures CC appeared to primarily catalyze the AP deflagration process with a minor effect upon the oxidizer-binder gas phase reactions, and at pressures below 1000 psia the IO had a primary catalysis effect upon the binder-oxidizer gas phase reactions while inhibiting AP deflagration, but at pressures above 1000 psia the IO catalyses primarily the AP deflagration process but not the oxidizer-binder gas phase reactions. In all cases there appeared no evidence that these two catalysts modified the pyrolysis mechanism of the binder.

It is known, however, that extensive melt flows exist with CTPB and HTPB binders during sandwich deflagration (as well as with other binders).^(3,4,5) Cinephotomacrography has insufficient resolution to investigate the interface processes or melt flows in any detail and it was not clear what catalytic effects might be taking place near the interface of the binder and oxidizer.

Consequently, it was desired to use high resolution microscopy on quenched samples to view any differences in surface structure and melt behavior in the presence of catalysis as compared with known results^(3,4,5) for uncatalyzed cases. It was furthermore desired to investigate more catalysts than previously used and to compare sandwich results with known propellant results.

Accordingly, the current study is concerned with two additional catalysts - iron blue (IB), a complex ammonium iron hexacyanoferrate, and ferrocene (F), biscyclopentadienyl iron. The burn rate behavior is obtained by cinephotomacrography over the pressure range 600-2000 psia, using AP and HTPB. The range 2000-3200 psia is not studied in this work, because it is excluded from the quenched combustion studies by reason of equipment capability. Furthermore, the AP deflagration process is not understood above 2000 psia (as compared with better knowledge below 2000 psia).⁽⁶⁾ Quenched samples with all four catalysts are then investigated by scanning electron microscopy to look at surface structure and melt behavior. Analysis is performed on the sandwich deflagration process to aid in interpretation of the experimental results.

II. CINEPHOTOMACROGRAPHY WITH IRON BLUE AND FERROCENE

The composite, two dimensional sandwich samples for this phase of the investigation were prepared by the method outlined in Reference (1). The binder thickness was controlled by Teflon spacers to a nominal 150 μm . The catalysts used were IB and F and were supplied by the Thiokol Chemical Corporation.

Iron Blue is commercially used as a pigment. It is a complex ammonium iron hexacyanoferrate with the chemical formula, $\text{Fe}(\text{NH}_4)\text{Fe}(\text{CN})_6$. It has a cubic crystalline structure. The iron is present as both ferric and ferrous ions in the lattice and they are indistinguishable. Ferrocene is an organometallic compound for which the chemical name is biscyclopentadienyl iron, $(\text{C}_5\text{H}_5)_2\text{Fe}$. It is a yellow crystalline solid with relatively high thermal stability for an organometallic compound.

The catalysts used were loaded into either the oxidizer, the binder, or at the binder-oxidizer interface. For dispersal in the oxidizer, 2% by weight of catalyst was added to the AP prior to grinding and pressing. For loading in the binder, the same volumetric loading as occurred in the AP was mixed into the binder prior to curing. For HTPB this was 4.37% by weight. When the catalyst was located at the binder-oxidizer interface, the same amount of catalyst as was added to the ammonium perchlorate, 2% by weight, was mixed with 2% AP and pressed onto the surface of a prepressed AP disc.

The prepared samples were mounted in the pressurized combustion apparatus of Jones⁽²⁾. Motion pictures of the burning sample were obtained at a rate of either 1600 or 3200 frames per second, at a latent image

magnification of 2 to 1. A summary film of this phase of the investigation is available on loan from the senior author of the report. Two frames from the motion pictures of ferrocene and iron blue added to the AP are reproduced in Figure II-1.

These motion pictures were used to obtain an accurate value of the sample burning rate. The sandwich vertical burn rate and the burn rate normal to the oxidizer surface, as defined in Reference (1), were obtained for the three types of catalyst addition at four pressures, 600, 1000, 1500 and 2000 psi. Burning rate data were taken only after a steady profile had been achieved and the surface was clearly visible over a substantial portion of the run. For the steady profile the sandwich vertical burn rate is the same regardless of the perpendicular distance from the binder-oxidizer interface. The burn rate normal to the oxidizer surface must be taken at a distance sufficiently far away from the interface for the oxidizer to have a definable, constant slope. These results are summarized in Table II-1.

The burn rates for the case of catalyst added to the oxidizer are shown in Figure II-2. The data indicated by CC and IO were obtained earlier and reported in Reference (1). The catalysts indicated are Harshaw Catalyst CuO2O2 (CC) and Fe_2O_3 , ferric oxide (iron III oxide - IO). The data of Friedman⁽⁷⁾ for CC are also shown in this figure. The burn rates are presented as a ratio to the burn rates of an AP-HTPB sandwich with no catalyst present, presented in Reference (1). The solid curves are the ratio of the sandwich vertical burn rates. The dashed curves are the ratio for the burn rates normal to the oxidizer surface. The dashed curves represent the effect of the catalyst addition to pure ammonium perchlorate



Figure 11-1 a. AP and IB-HTPB-AP, 600 psia.



Figure 11-1 b. AP and F-HTPB-AP, 1000 psia.

Table II-1

Summary of Results from Cinephotomacrography of Composite
Ammonium Perchlorate-HTPB Sandwiches with Catalysts.

Catalyst	Location	Pressure psia	Sandwich Vertical Burn Rate in/sec	Burn Rate Normal to the Oxidizer Surface in/sec
none		600	.237	.237
		1000	.360	.360
		1500	.386	.386
		2000	.351	.339
CuO ₂ O ₂	in AP	600	.405	.260
		1000	.612	.501
		1500	1.100	1.035
		2000	1.330	1.250
Ferric Oxide	in AP	600	.255	.137
		1000	.376	.203
		1500	.686	.540
		2000	.740	.695
Ferrocene	in AP	600	.269	.183
		1000	.359	.208
		1500	.450	.278
		2000	.524	.300
Iron Blue	in AP	600	.263	.182
		1000	.375	.246
		1500	.536	.234
		2000	.556	.379
CuO ₂ O ₂	in HTPB	600	.262	.246
		1000	.370	.345
		1500	.404	.404
		2000	.386	.386
Ferric Oxide	in HTPB	600	.208	.180
		1000	.337	.335
		1500	.320	.320
		2000	.415	.415

Table II-1 (Continued)

Catalyst	Location	Pressure psia	Sandwich Vertical Burn Rate in/sec	Burn Rate Normal to the Oxidizer Surface in/sec
Ferrocene	in HTPB	600	.293	.290
		1000	.318	.318
		1500	.357	.357
		2000	.383	.378
Iron Blue	in HTPB	600	.367	.367
		1000	.345	.345
		1500	.390	.330
		2000	.333	.322
CuO ₂ O ₂	on Interface	600	.323	.248
		1000	.562	.441
		1500	.360	.232
		2000	.543	.230
Ferric Oxide	on Interface	600	.221	.117
		1000	.368	.346
		1500	.645	.273
		2000	.758	.320
Ferrocene	on Interface	600	.342	.246
		1000	.521	.336
		1500	.310	.302
		2000	1.137	.480
Iron Blue	on Interface	600	.300	.197
		1000	.585	.338
		1500	.801	.413
		2000	1.068	.403

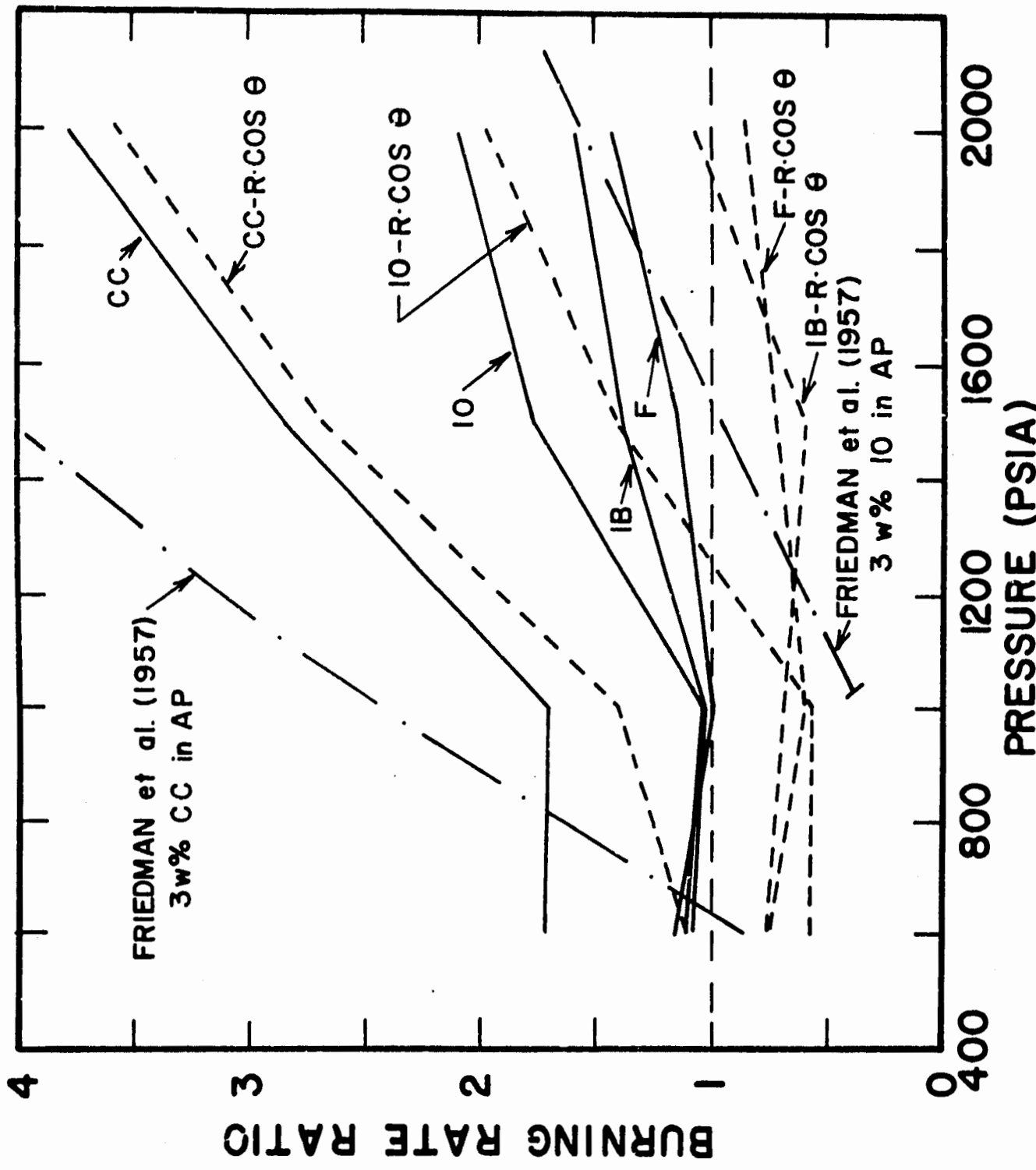


Figure II-2. Ratio of Catalyzed Sandwich Vertical Burn Rate and Burn Rate Normal to the Oxidizer Surface to the Burn Rate of an AP-HTPB Sandwich. Catalyst in AP Alone.

burn rates. Both IB and F retard the burn rate normal to the oxidizer surface for the pressure range investigated. This is in contrast to CC which augments the AP burn rate for the entire pressure range. The IO augments the burn rate for pressures greater than 1200 psi. The separation between the dashed and solid curves is representative of the amount of catalytic activity taking place in the binder-oxidizer reactions. This separation should be directly applicable to real propellant results and will be discussed in Chapter V.

The burn rates for the case of catalyst added to the binder are shown in Figure II-3. Within the accuracy of the experimental techniques there were no detectable angles from the horizontal present in the oxidizer to indicate any alteration of the burn rate normal to the oxidizer surface. Considering the absence of this difference, as was discussed above, this would indicate very little catalytic activity taking place in the vicinity of the binder-oxidizer interface. An exception to the foregoing is seen at 600 psia in the case of F and IB. The scatter of the sandwich vertical burning rate ratios about a ratio of unity in the 1000 to 2000 psi range is indicative of the experimental accuracy, since there is no significant visible effect upon the sandwich deflagration process with catalyst as opposed to an AP-HTPB sandwich. At 600 psia, however, there is a distinct catalytic effect with F and IB.

The burn rate data for the case of catalyst located at the binder-oxidizer interface are shown in Figure II-4. These data were obtained from the motion pictures. After examining scanning electron microscope pictures which are included in Appendix A, it was felt that these interface samples

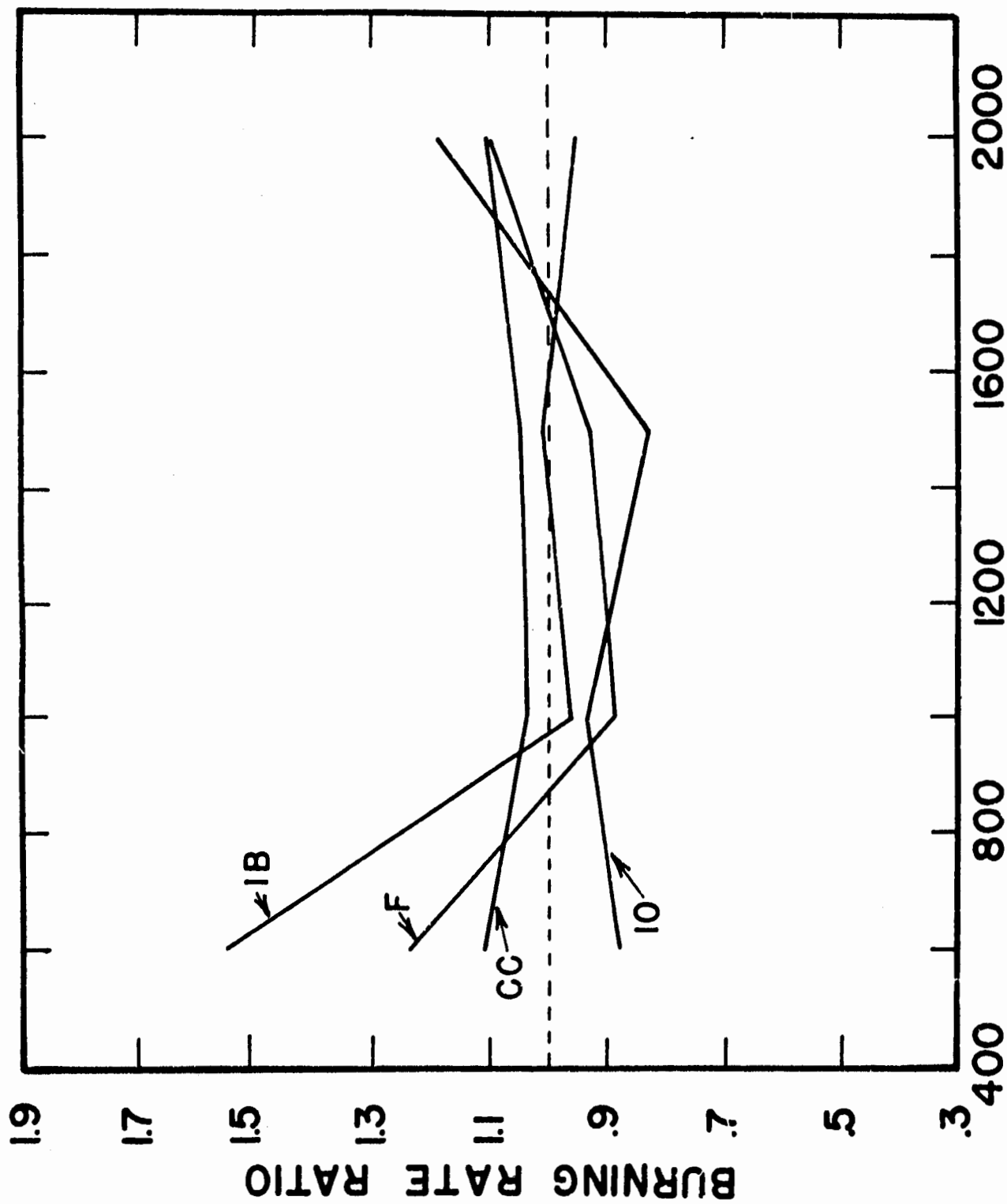


Figure II-3. Ratio of Catalyzed Sandwich Vertical Burn Rate to the Burn Rate of an AP-HTPB Sandwich Catalyst in Binder Alone.

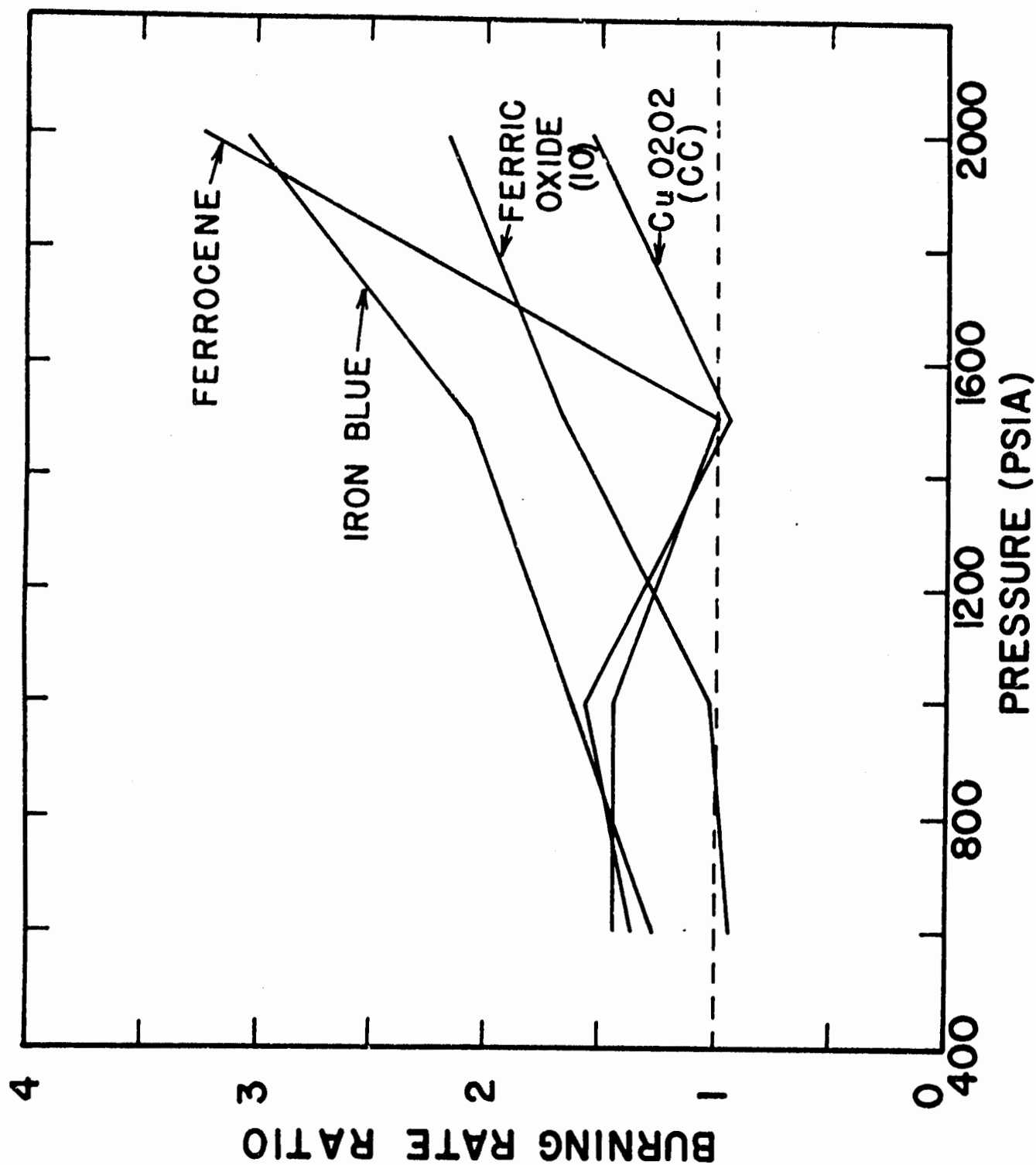


Figure II-4. Ratio of Catalyzed Sandwich Vertical Burn Rate to the Burn Rate of an AP-HTPB Sandwich Catalyst on Binder-Oxidizer Interface.

do not behave uniformly; therefore burn rate data obtained by observing only one edge of the sample may be in considerable error. The data presented in Figure II-4 shows augmentation of burning rates for all catalysts at 2000 psi. Again IO appears to retard the burning for 600 and 1000 psi. Both F and CC show retardation at 1500 psi. This is not in agreement with the observed behavior of quenched samples for these cases. Consequently, the burn rate data for interface samples are suspect and are presented here for interest and completeness only.

Concluding from the motion picture runs, a) there is very little burn rate or visible effect upon placing any of the catalysts in the binder with the exception of IB and F at low pressures, b) CC is the strongest catalyst for the AP deflagration process, c) below 1000 psia all four catalysts show roughly equal effectiveness in augmenting rate processes in the vicinity of the binder-oxidizer interface, d) IB and F show the strongest behavior near the interface above 1000 psia followed by IO and CC and e) IB and F inhibit the AP deflagration process over the entire pressure range studied while IO is an AP inhibitor below 1200 psia.

III. SCANNING ELECTRON MICROSCOPY WITH FOUR CATALYSTS

The samples for this phase of the investigation were prepared in the same manner as those for the cinephotomacrography experiments. In addition to IB and F the catalysts CuO₂O₂ (CC) and Ferric Oxide (IO) were loaded in the oxidizer, binder and at the binder-oxidizer interface. Partially burned samples were obtained for scanning electron microscopy by terminating combustion by rapid depressurization using the burst diaphragm method⁽⁴⁾. An electronic timer circuit was used to obtain accurate, reproducible time delays between the ignition of the sample and interruption of burning of the sample. The timer was modified to allow delays of from 22 milliseconds to three seconds. The initial estimates for the time delays were obtained from the cinephotomacrography burn rate data of Chapter II .

The sample observation was carried out in the Physical Science Division of the Engineering Experiment Station of the Georgia Institute of Technology. A Cambridge Stereoscan Scanning Electron Microscope, Mark IIa, was used for all observations in this chapter. Magnifications from x18 to x50,000 were available. A focused electron beam of .01 μm in diameter was used to scan the samples which were placed in the specimen holder under a high vacuum. The high energy beam stimulates the emission of secondary electrons or backscattered electrons, x-rays and, sometimes, light photons from the sample surface. If the sample is electrically non-conducting, it will gradually accumulate an electrical charge and cause an additional scattering of the electron beam. Since the composite propellant samples were non-conducting, they had to be coated with a conducting coating before the surface could be examined with the scanning electron microscope. A combined

coating of carbon and gold-palladium (60-40) was placed on the samples by vacuum deposition. This coating varied from 300 to 400 Å in thickness. It would not be detected unless magnifications in excess of 50,000 were used.

The electrical signal generated by the collected secondary or back-scattered electrons is used to control the brightness of a cathode ray tube which is synchronized to the scan of the electron beam. The photograph of the cathode ray tube is referred to as the electron micrograph. The x-rays emitted by the sample are characteristic of the elements present in the sample and can be collected and analyzed. Both the chemical identity and spatial distribution of the elements in the region of the electron beam can be determined. Iron is always indicated due to the magnet pole pieces. For non-conducting samples the coating materials are also detected. This analysis was used to determine the high iron content of particles visible in the AP-IO samples. The spatial resolution of this measurement is 10^4 times better than the electron microprobe investigation described in Chapter IV, but the number of elements that can be detected is limited and the quantitative results are not as accurate as with the microprobe.

The results of this investigation are presented in a series of 66 micrographs covering the surface details of 21 partially burned samples with catalysts in either the binder or the oxidizer. These samples were partially burned at 600, 1000, 1500 and 2000 psia, in a dry nitrogen atmosphere. A series of 27 micrographs are included in Appendix A covering 7 samples with the catalyst located at the binder-oxidizer interface. These samples were not included in this chapter because of the erratic behavior of these samples. The cine-photomacrography of these samples indicated some

questionable data at 1500 psia. Six attempts were made with F and IB at the interface for 1500 psia to obtain a quenched sample. No satisfactory sample was obtained for this case. Furthermore, even if satisfactory reproducible results could be obtained, there is question in interpretation of the results.

Uncatalyzed Sandwiches

A set of four AP-HTPB sandwiches were included in the study for comparison purposes. These micrographs are shown in Figures III-1 through 13 and the results are summarized in Table III-1. The observations are in accord with those of Boggs and Zurn⁽⁵⁾, where experiments are common to both works. The determination of the extent of the binder melt flow is arbitrary. It has been included for comparison with the catalyzed samples. It is a representative value, as is the tabulated binder height. But it is a meaningless observation when trying to generalize results to real propellant behavior. It is known from the cinephotomacrography that there is a substantial binder char layer, which is apparently removed during the quench process. There is a high probability that less viscous binder is also ejected. This would alter the binder height. Nevertheless, the increase of binder height with pressure increase is consistent with the higher AP burn rate at higher pressure. This allows less time for the binder to decompose.

AP-HTPB.

600 psia. Figures 1 and 2 -- The entire oxidizer surface shows evidence of having been covered with a frothy structure. There is a visible binder melt flow out over the oxidizer surface to approximately 140 μm from

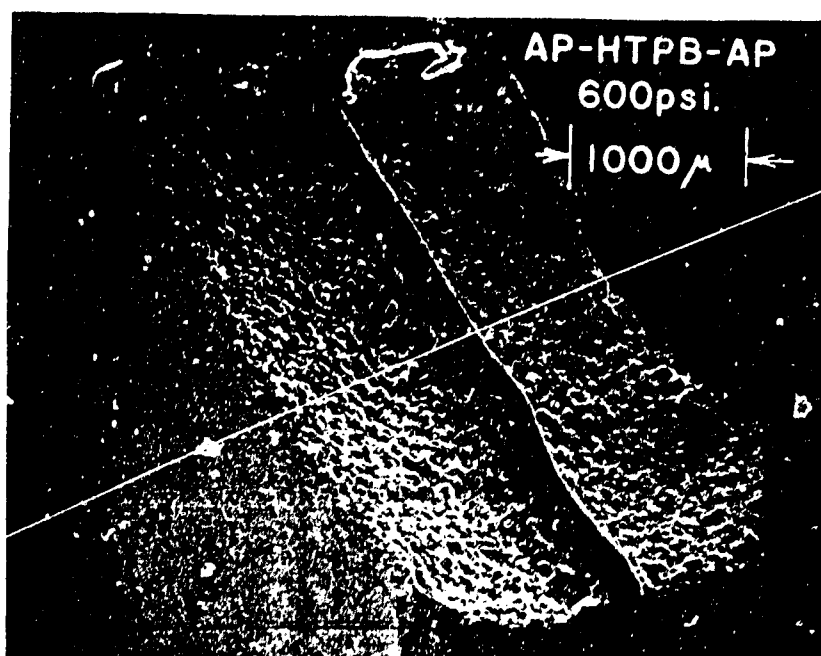


Figure III-1. AP-HTPB-AP 600 psia (x24.3).

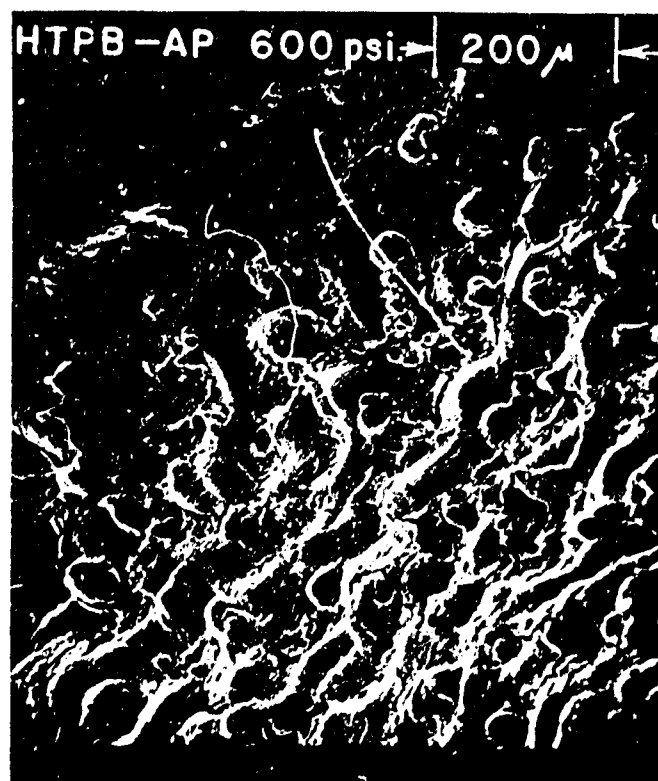


Figure III-2. AP-HTPB 600 psia (x121).

Table III-1

Summary of Results from Scanning Electron Microscopy of Uncatalyzed Composite Solid Propellant Sandwiches

Pressure psia	Figure No. III-	Binder Melt Flow μm	Binder Height μm
600	1,2	140	300
1000	3,4,5,6	150	450
1500	7,8,9,10	200	400
2000	11,12,13	350	500

th. interface. This flow has retarded the oxidizer regression rate causing the point of maximum regression to be well into the oxidizer layer. The binder height is approximately 300 μm . There is a continuous slope at the binder-oxidizer interface. There is no significant visible edge cooling effect shown by the sample.

1000 psia. Figures III-3 through 6 -- The entire oxidizer surface is covered with ridges and valleys of uniform density. The binder melt flow extends 150 μm over the oxidizer surface. The binder height is 450 μm . There is a continuous slope at the binder oxidizer interface and the point of maximum sandwich regression is at the mid point of the oxidizer layer. Note that in Figure III-6 the cracks in the binder melt flow reveal a porous AP structure. This flow is approximately one μm thick.

1500 psia. Figures III-7 through 10 -- The density of the ridges and valleys has decreased. The distribution of these ridges and valleys is

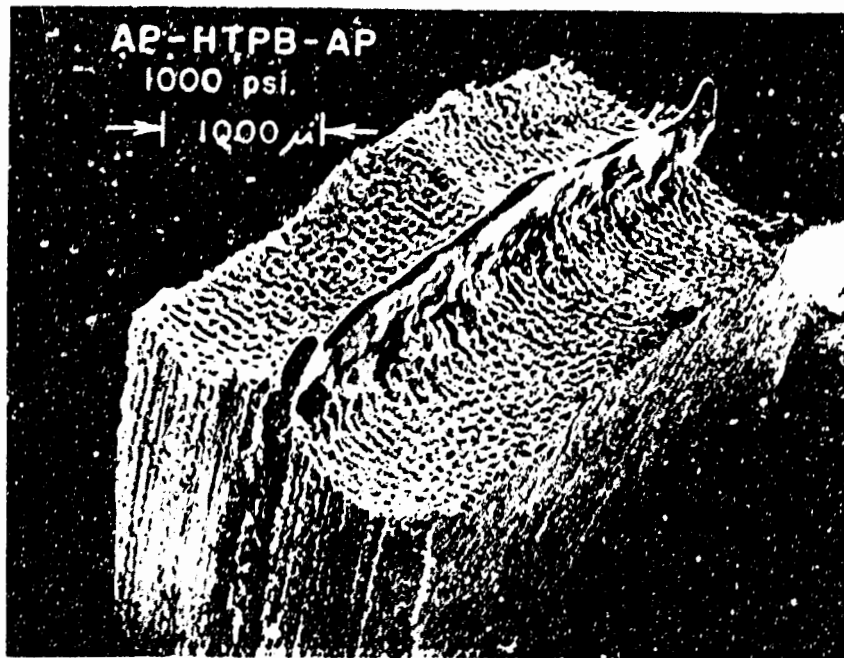


Figure III-3. AP-HTPB-AP 1000 psia (x21.2).



Figure III-4. AP-HTPB 1000 psia (x106).

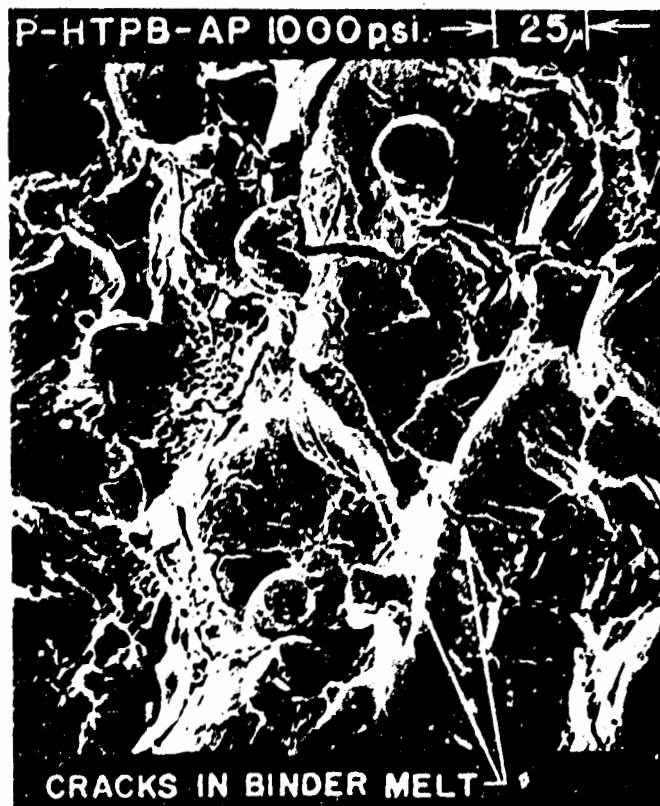


Figure III-5. AP-HTPB 1000 psia (x110).



Figure III-6. AP-HTPB 1000 psia (x510).

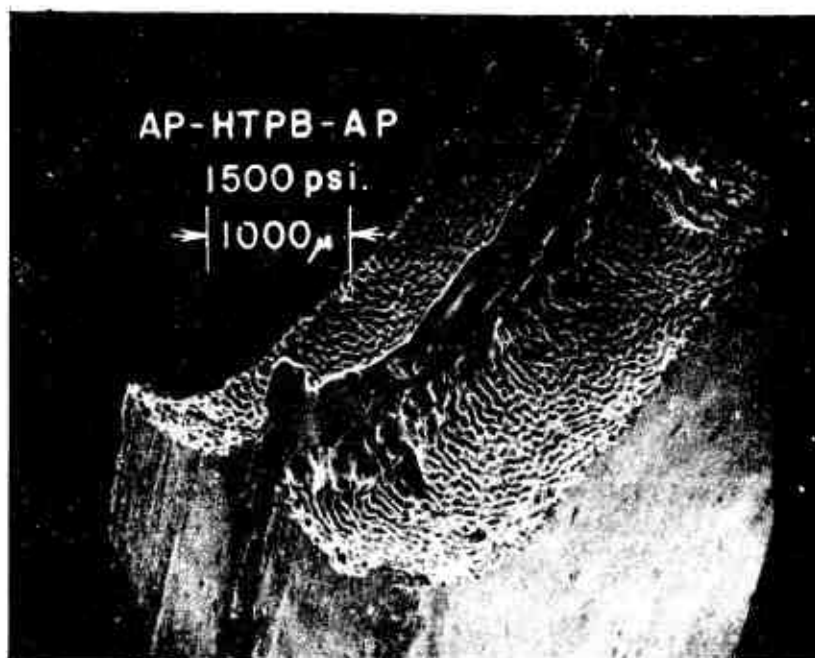


Figure III-7. AP-HTPB-AP 1500 psia (x20.8).

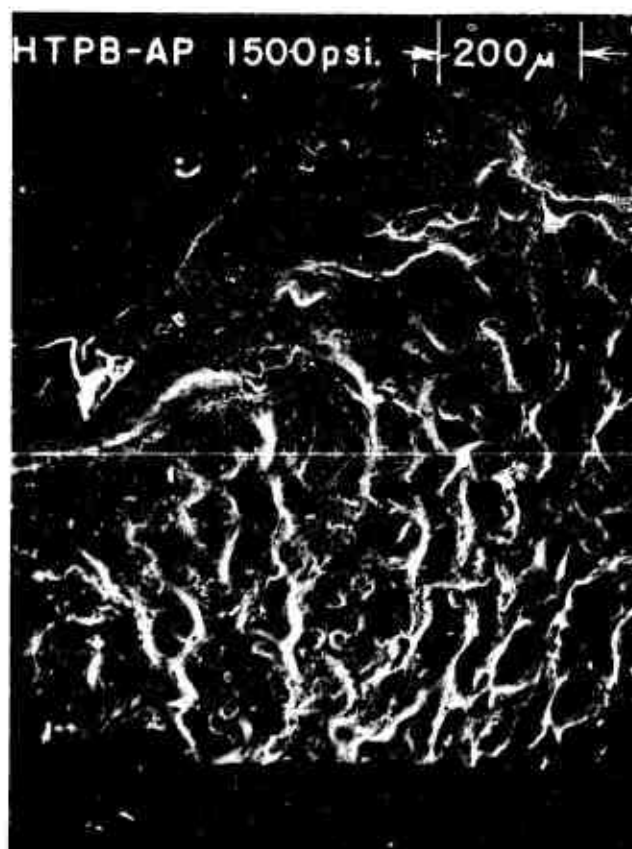


Figure III-8. HTPB-AP 1500 psia (x102).

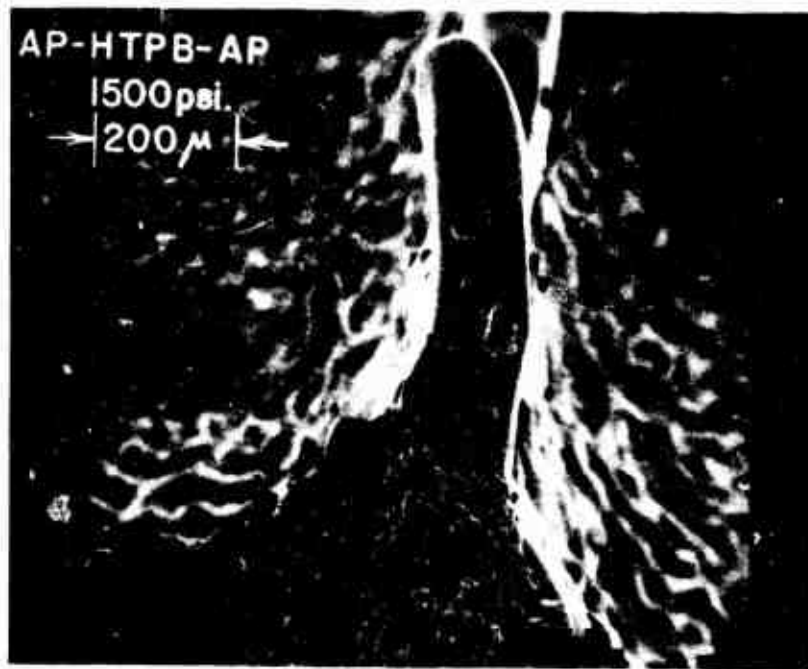


Figure III-9. AP-HTPB-AP 1500 psia (x102).

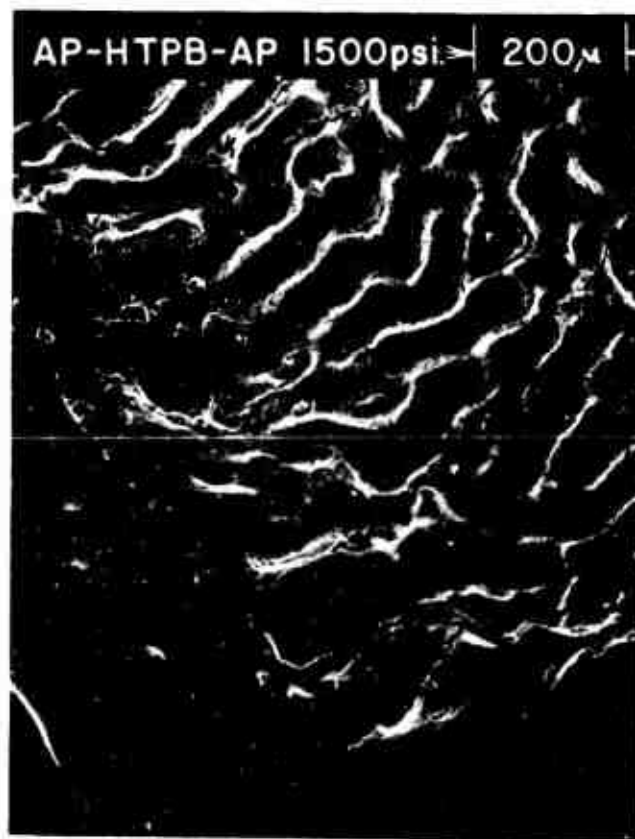


Figure III-10. HTPB-AP 1500 psia (x106).

uniform over the entire AP surface. The binder melt flow extends 200 μm over the oxidizer surface. The binder height is 400 μm . There is a continuous slope at the binder-oxidizer interface and the point of maximum regression has been displaced further from the interface than at lower pressures.

2000 psia. Figures III-11 through 13 -- The surface is still covered with ridges and valleys but in several areas a region of hemispherical protrusions with radii of 50 μm were observed. The binder melt flow is more irregular. It extends up to 350 μm onto the AP in some areas and is non-existent in other areas. The binder height is 500 μm . The location of the point of maximum regression varies with the binder melt flow. At one section it is located near the interface while at another section it has moved to the free edge of the oxidizer. There is also some indication of an edge cooling effect at one free edge, but it is not uniform and none was observed with the previous three samples. Therefore retardation of oxidizer burning rates near the free edges due to cooling effects has been considered unimportant.

In summary, for the pure AP-HTPB sandwiches, it can be said that as the pressure increases the mean surface irregularities increase. As the binder height increases, the binder melt flow does exist and its extent tends to increase. The point of maximum regression is always in the oxidizer and tends to move away from the binder as the pressure increases. There is no substantial cooling effect noted. These observations are in accord with the results of Boggs and Zurn.

Catalysts in the Oxidizer

The following section is devoted to a discussion of the electron

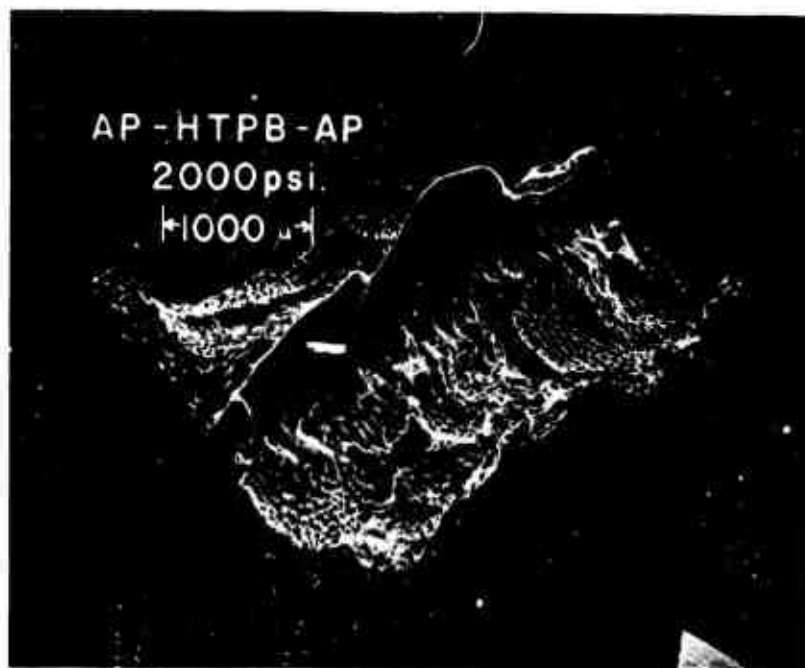


Figure III-11. AP-HTPB-AP 2000 psia (x20.4).

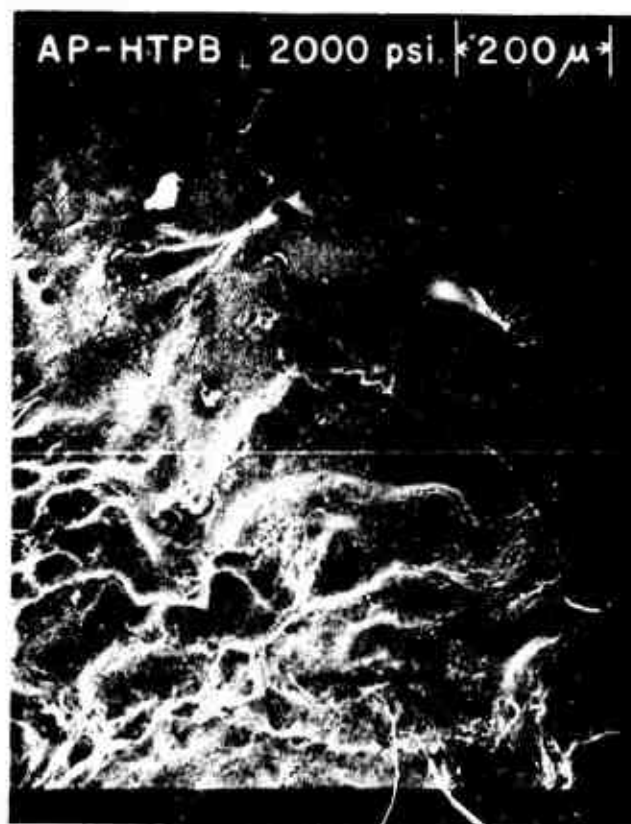


Figure III-12. A-HTPB 2000 psia (x106).

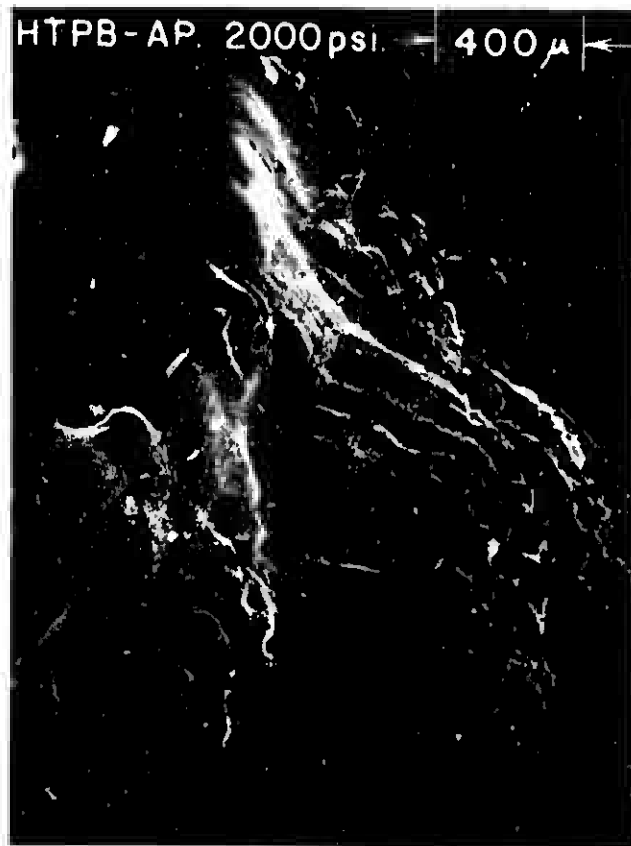


Figure III-13. HTPB-AP 2000 psia (x102).

micrographs from the samples containing the catalyst in the ammonium perchlorate. They were compared to each other and to the pure sandwiches just discussed. The micrographs are included in Figures III-14 through 52. These micrographs cover 13 samples and they are summarized in Table III-2.

Table III-2

Summary of Results from Scanning Electron Microscopy of Composite Solid Propellant Sandwiches with Catalyst in the Oxidizer

Catalyst	Location	Pressure psia	Figure No. III-	Binder Melt Flow μm	Binder-Oxidizer Interface Slope
CuO ₂ O ₂ (CC)	in AP	600	14,15	30	continuous
		1000	16,17,18	25-50	sections continuous
		1500	19,20	10-40	sections continuous
		2000	21,22	25	nearly discontinuous
Ferric Oxide (IO)	in AP	600	23,24,25	60-80	nearly discontinuous
		1000	26,27,28	none	discontinuous
		1500	29,30,31	<50	double dip
		2000	32,33,34	<25	double dip
Ferrocene (F)	in AP	600	35,36, 37,38	50	continuous
		1000	39,40	60	continuous
		1500	41,42,43	<50	continuous
		2000	44,45	<40	continuous
Iron Blue (IB)	in AP	600	35,46	<30	continuous
		1000	39,47,48	<10	continuous
		1500	41,49,50	30	continuous
		2000	51,52	none	slight undercutting or sag

AP and CC - HTPB.

600 psia. Figures III-14 and 15 -- The surface of the ammonium perchlorate with 2% by weight of CC is relatively smooth and uniform. There is a porous structure of holes of diameter less than 4 μm . The oxidizer surface with catalyst has a slope of between 40° and 48° . There is a slight binder melt flow over the oxidizer surface of 30 μm . The maximum regression is in the oxidizer. Some particles have been deposited on the binder, probably during the quench process.

1000 psia. Figures III-16 through 18 -- The surface of the oxidizer with catalyst resembles the 600 psia sample. The slope of this surface lies between 40° and 45° . It does not appear to be as steep as the previous case. The binder melt flow varies from 25 to 50 μm . There is a continuous slope at the interface at specific locations as shown in Figure III-18. The maximum regression point appears to be at the edge of the binder melt flow.

1500 psia. Figures 19 and 20 -- The surface of the oxidizer with catalyst continues to be relatively smooth. The slope of this surface is almost 49° . The binder melt flow has been reduced to between 10 μm and 40 μm . Again, the slope at the interface is continuous at specific locations where the binder melt flow is the most extensive.

2000 psia. Figures 21 and 22 -- The surface of the oxidizer with catalyst is relatively smooth and the slope of this surface has increased to 64° . The melt flow appears to extend approximately 25 μm . The maximum regression point occurs within 25 μ of the interface.

These four samples were very consistent; the AP with 2% by weight of CC exhibited a relatively smooth surface for the four pressures. The slope of

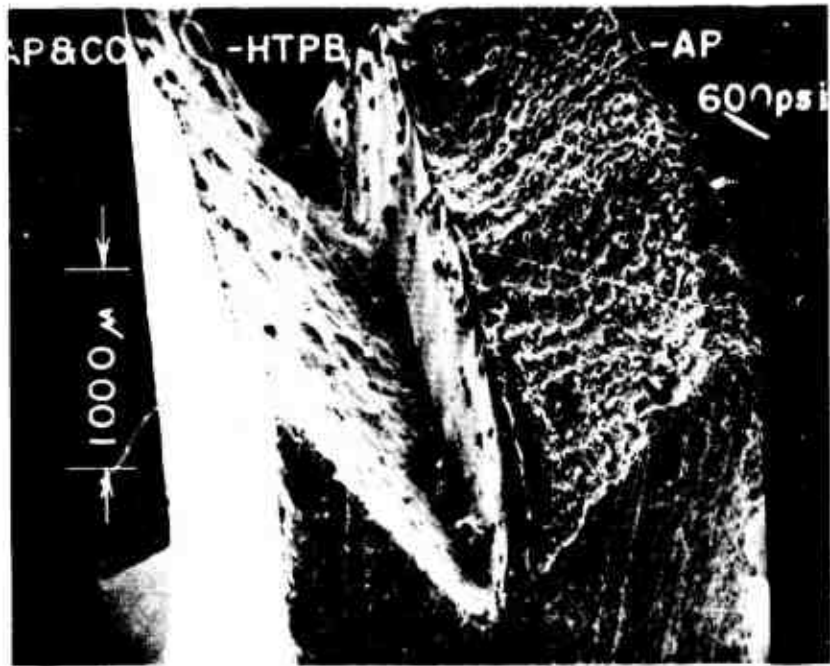


Figure III-14. AP and CuO₂O₂(CC)-HTPB-AP 600 psia (x27).

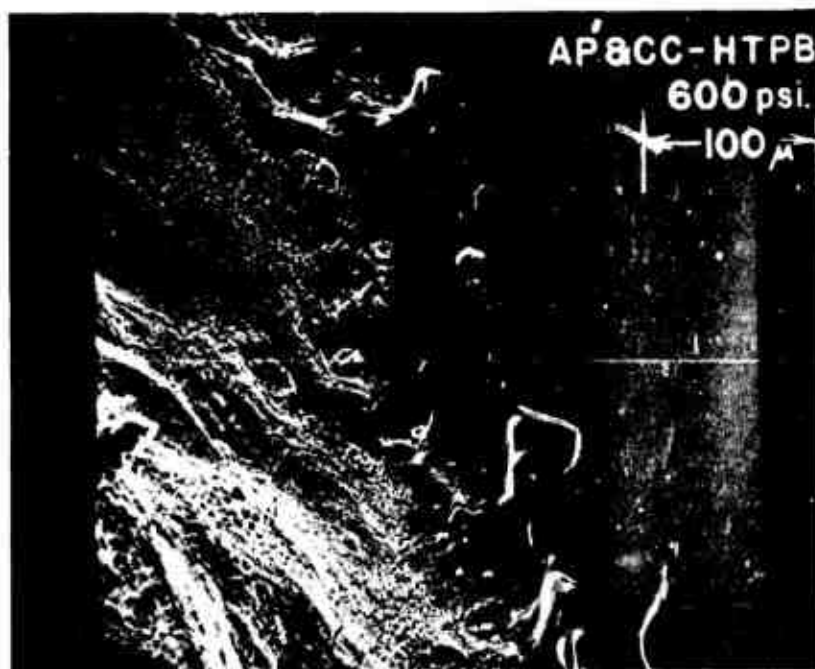


Figure III-15. AP and CuO₂O₂(CC)-HTPB 600 psia (x240).

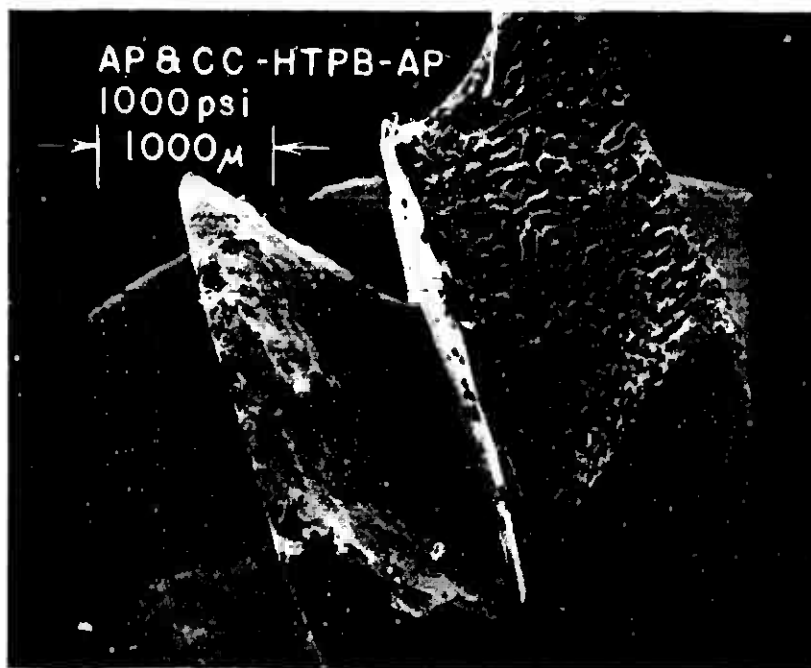


Figure III-16. AP and CuO₂(CC)-HTPB-AP 1000 psia (x24.6).

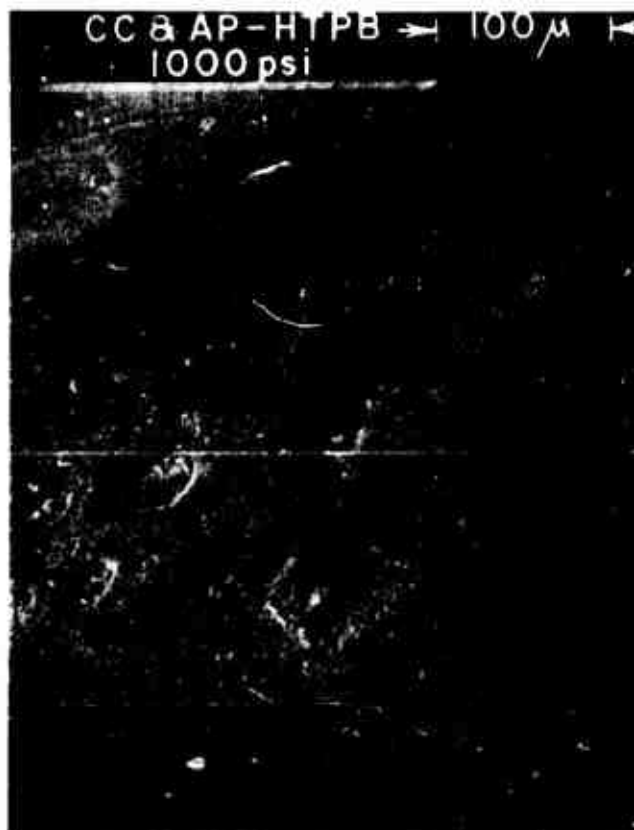


Figure III-17. HTPB-AP and CuO₂(CC) 1000 psia (x238).



Figure III-18. AP and CuO₂ (CC)-HTPB-AP 1000 psia (x49.3).

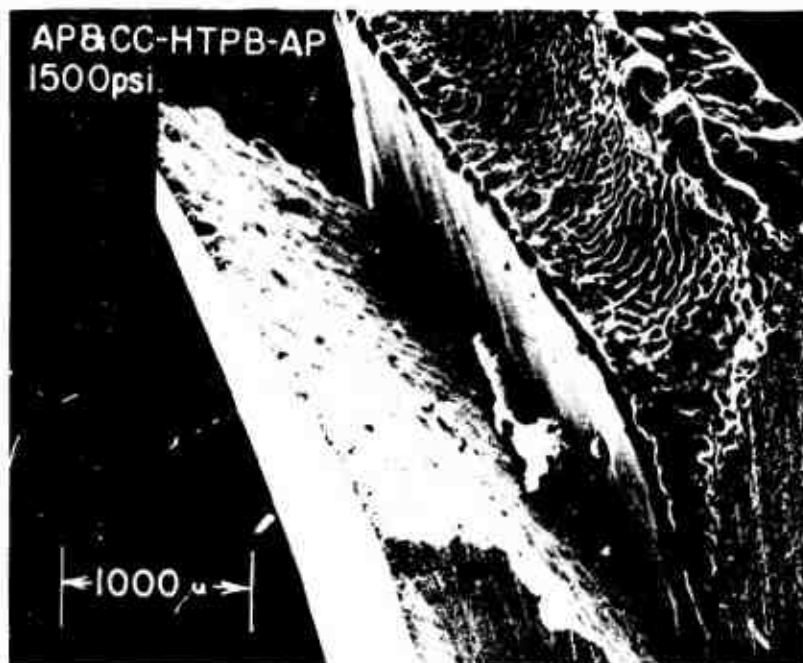


Figure III-19. AP and CuO₂ (CC)-HTPB-AP 1500 psia (x26.5).

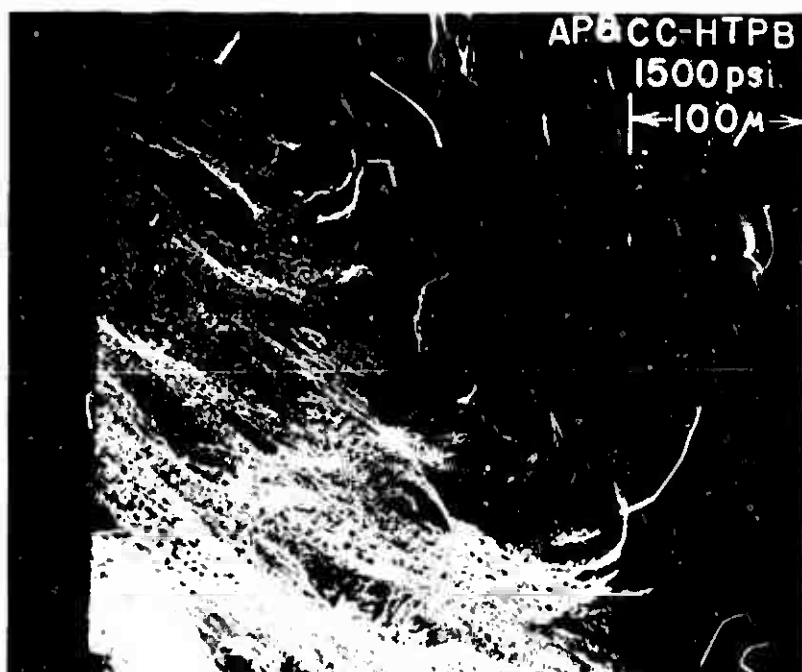


Figure III-20. AP and CuO₂ (CC)-HTPB 1500 psia (x250).

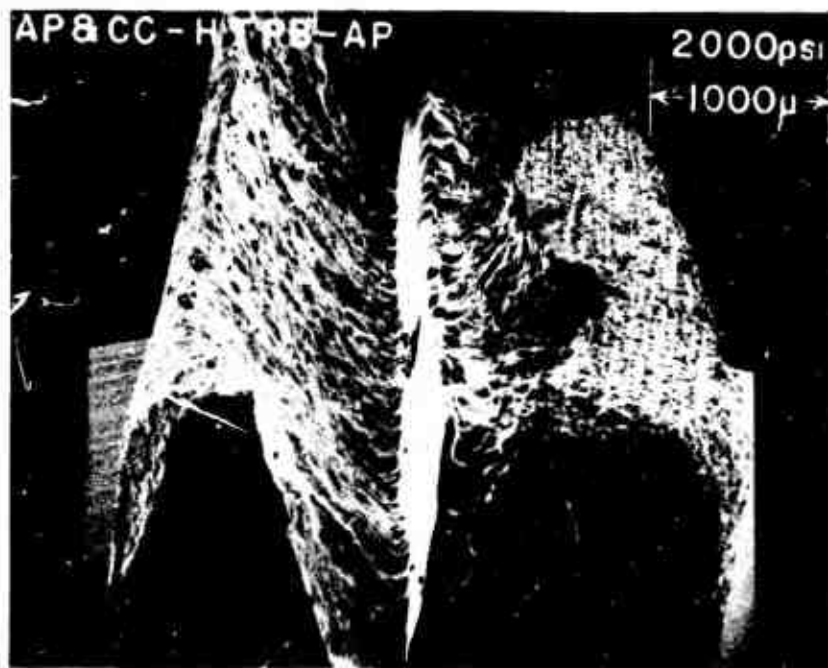


Figure III-21. AP and CuO₂ (CC)-HTPB-AP 2000 psia (x25).

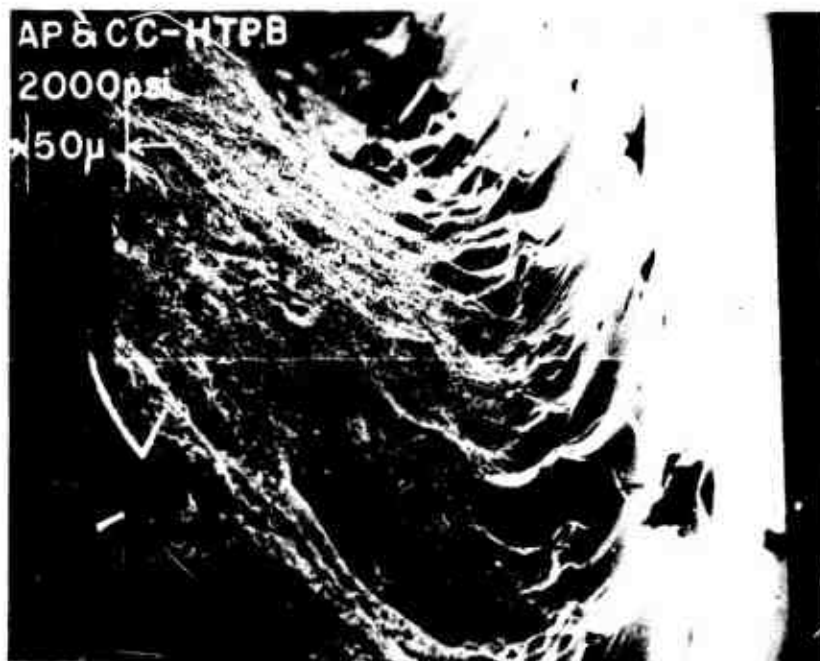


Figure III-22. AP and CuO₂ (CC)-HTPB 2000 psia (x280).

the oxidizer with catalyst surface appears to increase as the pressure increases. This was inconsistent with the results obtained from cinephotomacrography. The surface slope decreased as the pressure increased from 50° to 20°. There is a virtual discontinuity in slope at the interface, but the leading edge of regression, while appearing to be at the binder-oxidizer interface, is actually displaced outward by the slight melt flow.

AP and IO - HTPB.

600 psia. Figures III-23 through 25 -- The surface of the oxidizer, AP with 2% by weight of IO, consists of a smooth background with flakes of approximately 50 μm in diameter scattered over the entire surface. This flake structure is also visible on the solidified binder. There is a mild slant at the binder-oxidizer interface with evidence of retardation of the oxidizer at this interface due to a binder melt flow of 60 to 80 μm . There is a slope discontinuity indicated at this interface in Figures III-24 and 25.

1000 psia. Figures III-26 through 38 -- The flake structure is observed on the oxidizer surface. The size of individual particles has increased slightly to 60-100 μm . The structure of these flakes seems to be small petaloid structures of 10 μm diameter. The background oxidizer is still relatively smooth. There was no obvious binder melt flow. The maximum regression appears to be at the binder oxidizer interface where there is a definite discontinuity in slope.

1500 psia. Figures III-29 through 31 -- The entire oxidizer surface has been covered with a layer of particles probably related to a further coalescing of the flake structure observed at lower pressures. There are large cracks in this coating and sections missing, probably

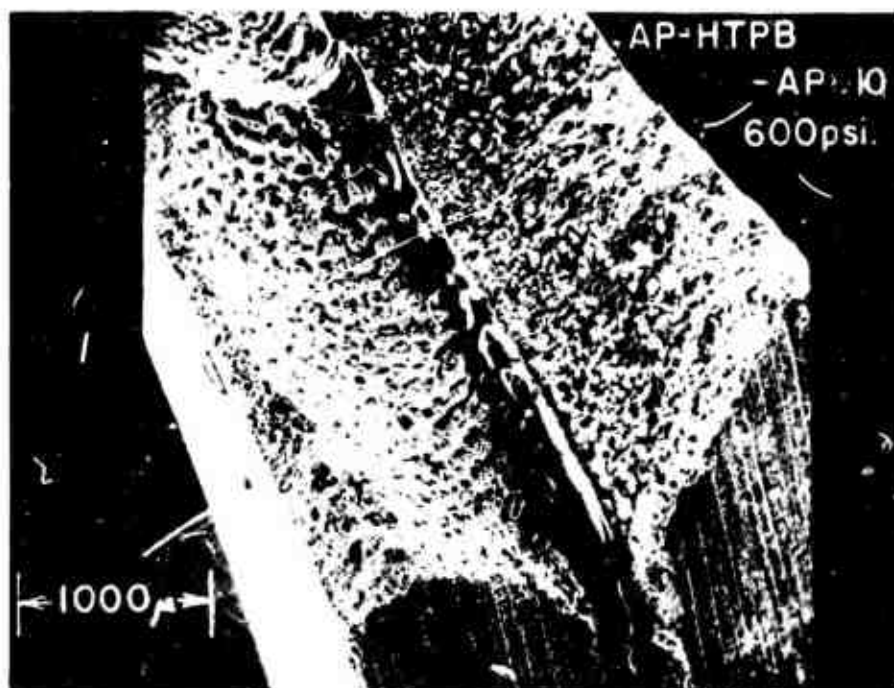


Figure III-23. AP-HTPB-AP and Ferric Oxide (IO) 600 psia (x27).



Figure III-24. HTPB-AP and Ferric Oxide (IO) 600 psia (x260).

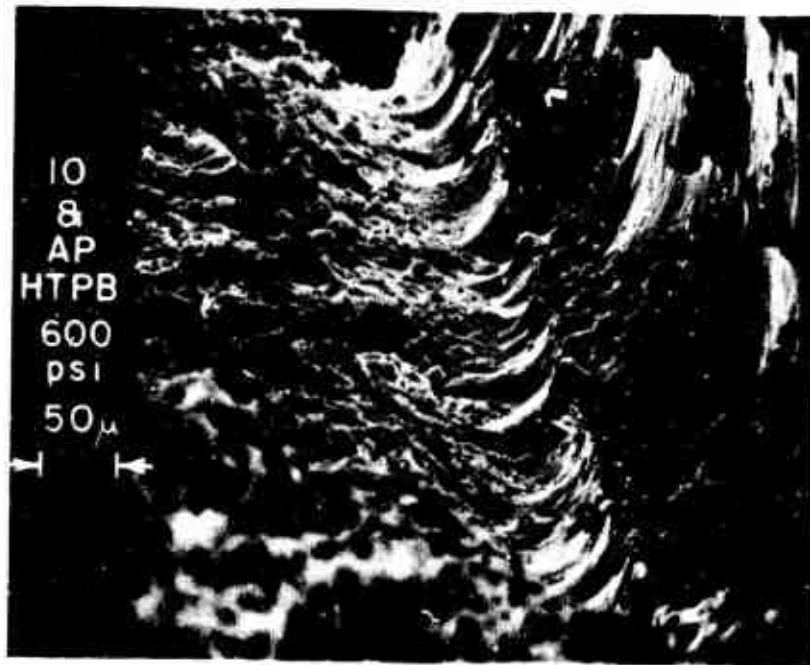


Figure III-25. AP and Ferric Oxide (IO)-HTPB 600 psia (x220).



Figure III-26. AP and Ferric Oxide (IO)-HTPB-AP 1000 psia (x21.2).



Figure III-27. AP and Ferric Oxide (IO)-HTPB 1000 psia (x204).



Figure III-28. HTPB-AP and Ferric Oxide (IO) 1000 psia (x204).

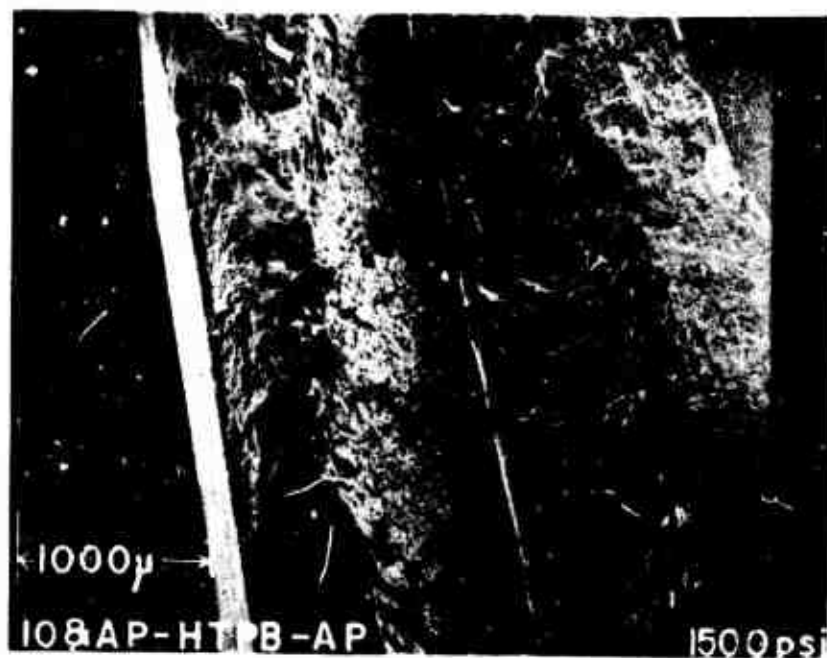


Figure III-29. AP and Ferric Oxide (IO)-HTPB-AP 1500 psia (x27).



Figure III-30. AP and Ferric Oxide (IO)-HTPB 1500 psia (x240).



Figure III-31. AP and Ferric Oxide (IO)-HTPB-AP 1500 psia (x230).

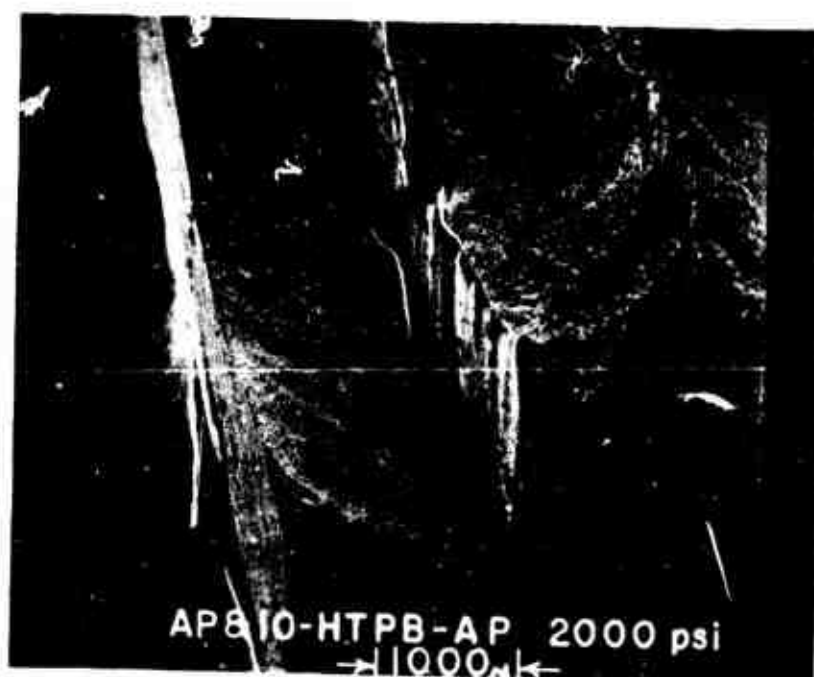


Figure III-32. AP and Ferric Oxide (IO)-HTPB-AP 2000 psia (x19.6).

removed by the rapid depressurization. There is an indication of a binder melt flow of less than 50 μm with a definite cusp or double dip of the binder surface visible in Figures III-30 and 31. Molten binder could be ejected during the quench process to form this double dip.

2000 psia. Figures III-32 through 34 -- Again the entire oxidizer surface has been covered with a definite crust-like structure. This has no resemblance to the flakes observed at lower pressures. The difference is easily seen in Figure III-34. The surface where the crust has been removed is similar to the background surface observed at lower pressures in Figures III-24 and 28. Large sections of this crust have been removed, probably in the quench process. The binder melt flow is intermittent and less than 25 μm in extent when it occurs. Again there is a relative maximum of the binder height giving the appearance of a cusp at the binder oxidizer interface. The leading edge of regression appears to be located at the binder-oxidizer interface or slightly into the binder; however, the latter possibility is doubtful.

There is a definite similarity of the background surface of the AP and IO for all pressures. From the cinephotomacrography for this series of experiments, the formation of a large scale frothy structure was indicated. The formation of this froth increased as the pressure increased. Sections of this structure can be observed to break off as the sample continues to burn. The flakes and the crust of the quenched samples are the only remnants of this frothy structure. The binder-oxidizer interface slope is not continuous and the slope of the oxidizer surface is similar for all pressures. This was not consistent with the cinephotomacrography results. The sample slopes varied from 55° to 60° at 600 psia to 20° at 2000 psia in the movies.

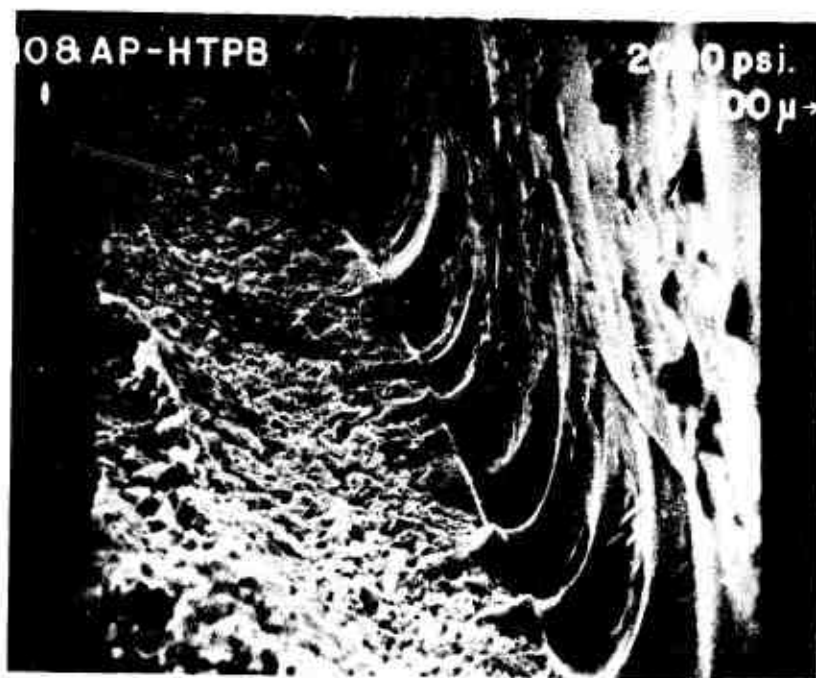


Figure III-33. AP and Ferric Oxide (IO)-HTPB 2000 psia (x195).



Figure III-34. AP and Ferric Oxide (IO) 2000 psia (x484).

AP and F - HTPB.

600 psia. Figures III-35 through 38 -- The surface of the oxidizer, AP with 2% by weight of F, is uneven and frothy. There is a resemblance to that of the pure AP. There appears to be a scattering of additional particles resting on the surface of the oxidizer. These particles do not appear to be in the binder melt flow. There is a definite binder flow of at least 50 μm in extent. The binder appears to sag more than in previous samples. This sag leads to the dark lines of Figures III-37 and 38.

1000 psia. Figures III-39 and 40 -- The surface continues to resemble that of pure AP with additional particles observed on the uneven surface. An optical microscopic investigation showed that these particles were red and black. The binder melt flow was 60 μm . The maximum regression is occurring at the edge of the binder melt flow. The slope is continuous at the interface.

1500 psia. Figures III-41 through 43 -- The appearance of the entire surface is slightly smoother than for the pure AP above. The ridges and valleys structure is apparent but the density of roughness is greater than with pure AP. Red and black particles again are obvious on the surface. The binder melt flow is less than 50 μm in extent; this is retarding the AP regression at the interface and displacing the point of maximum regression slightly to the oxidizer.

2000 psia. Figures III-44 and 45 -- The binder melt flow has been reduced to less than 40 μm . The oxidizer surface has lost any similarity with the pure AP case. The surface is irregular and frothy in appearance. Particles are still visible on the surface but their diameters have decreased.

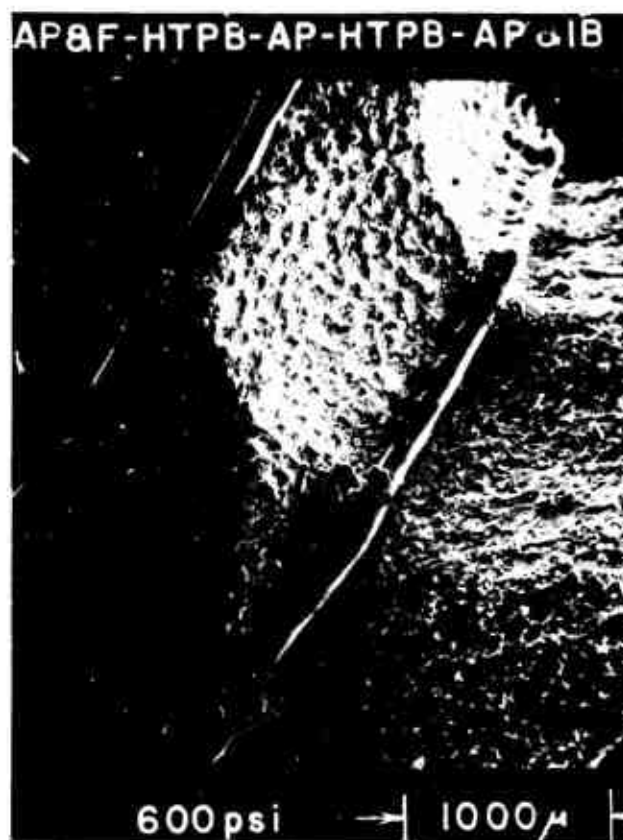


Figure III-35. AP and Ferrocene (F)-HTPB-AP-HTPB-AP and Iron Blue (IB) 600 psia (x28).



Figure III-36. HTPB-AP and Ferrocene (F) 600 psia (x262).

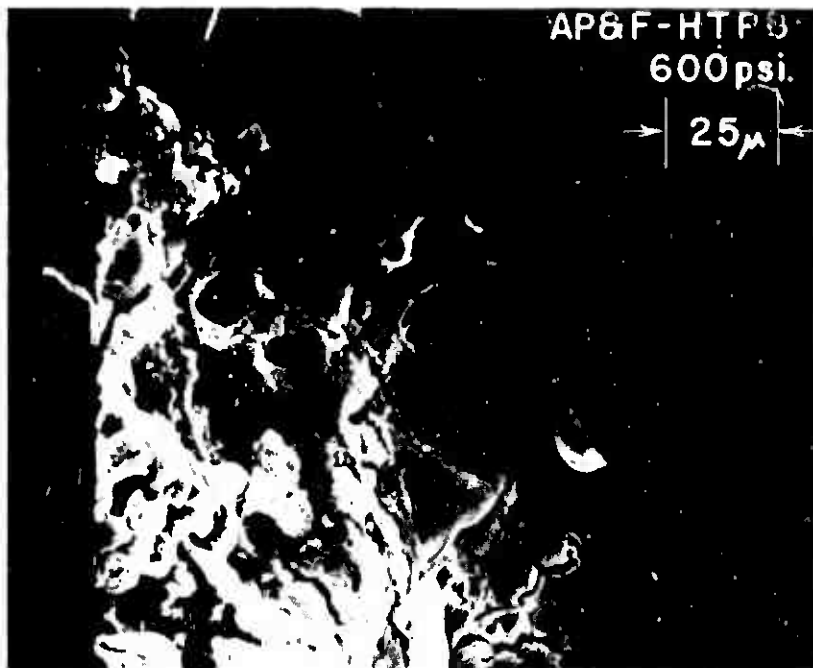


Figure III-37. AP and Ferrocene (F)-HTPB 600 psia (x650).

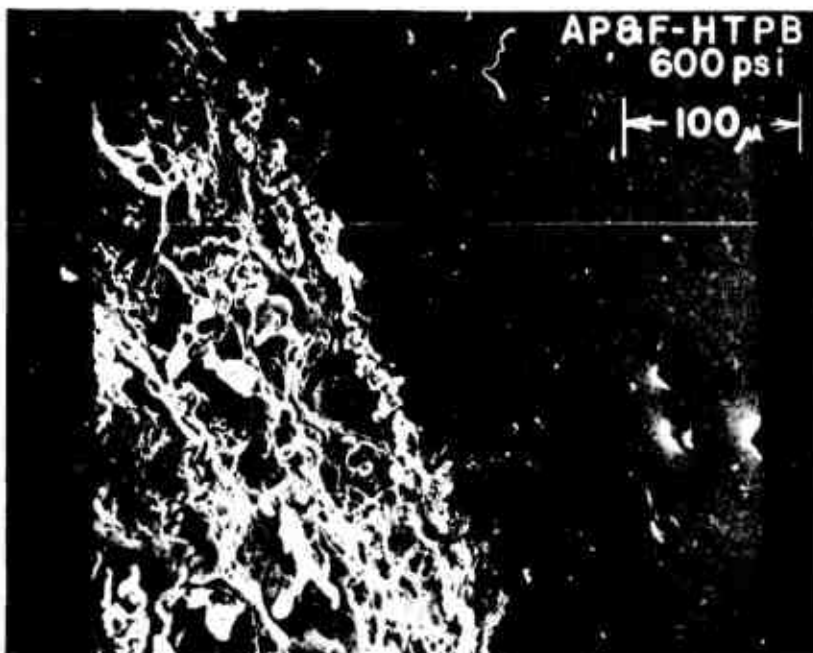


Figure III-38. AP and Ferrocene (F)-HTPB 600 psia (x250).

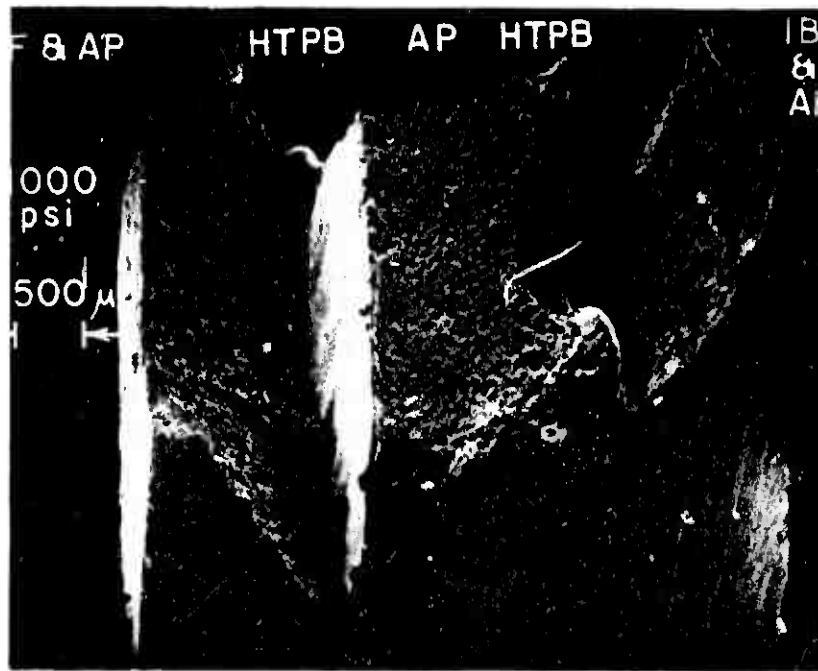


Figure III-39. AP and Ferrocene (F)-HTPB-AP-HTPB-AP and Iron Blue (IB) 1000 psia (x18.7).



Figure III-40. HTPB-AP and Ferrocene (F) 1000 psia (x221).

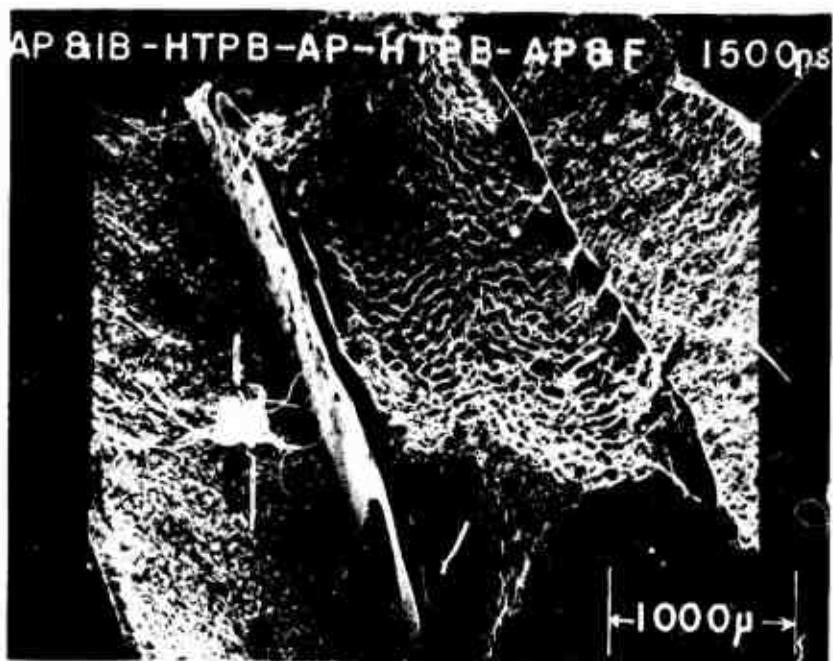


Figure III-41. AP and Iron Blue (IB)-HTPB-AP-HTPB-AP and Ferrocene (F) 1500 psia (x28.7).

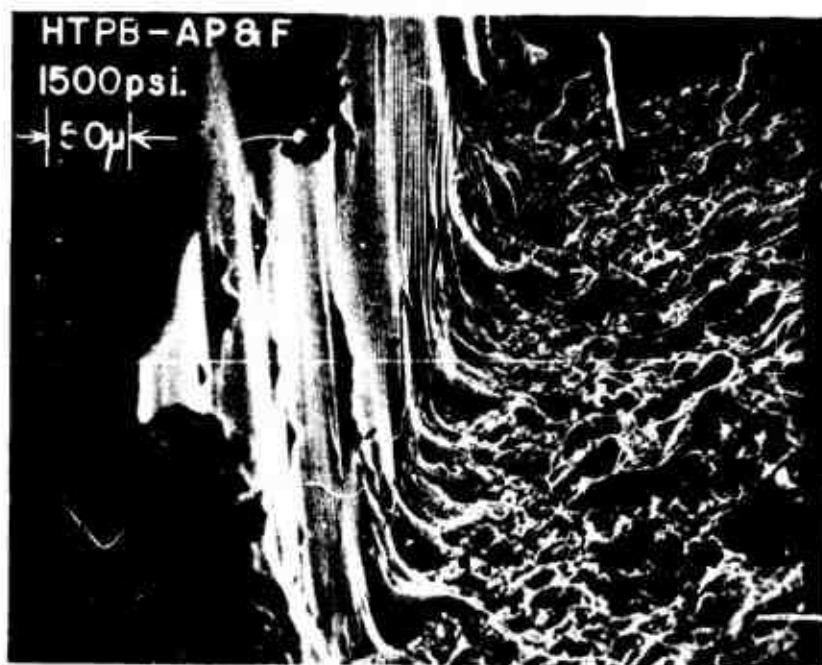


Figure II - . . . HTPB-AP and Ferrocene (F) 1500 psia (x240).

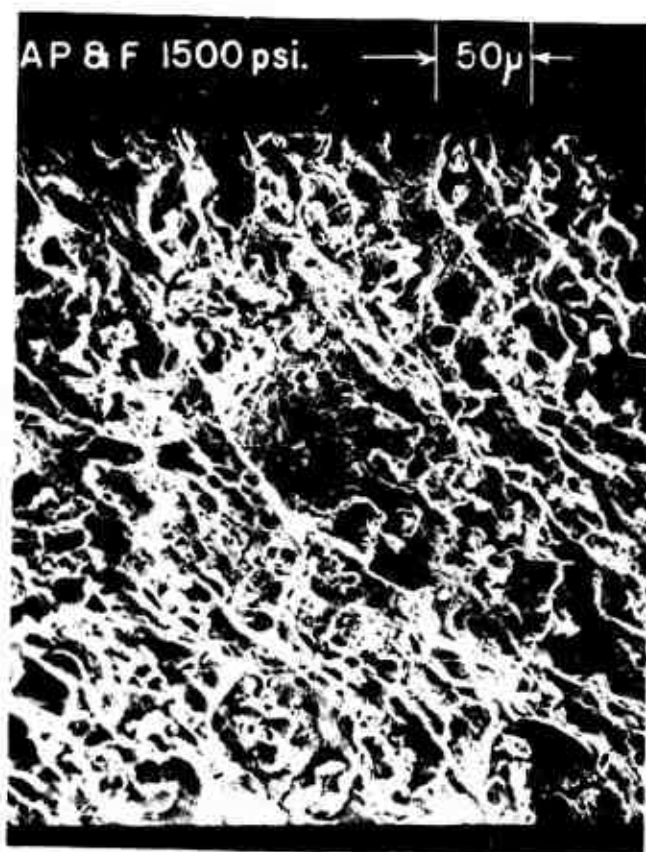


Figure III-43. AP and Ferrocene (F) 1500 psia (x260).

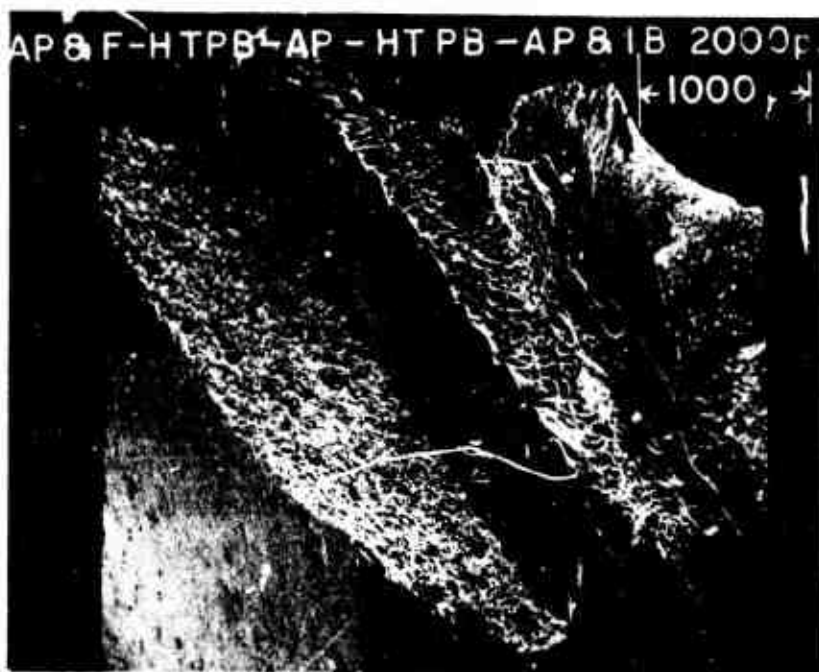


Figure III-44. AP and Ferrocene (F)-HTPB-AP-HTPB-AP and Iron Blue (IB) 2000 psia (x24.3).

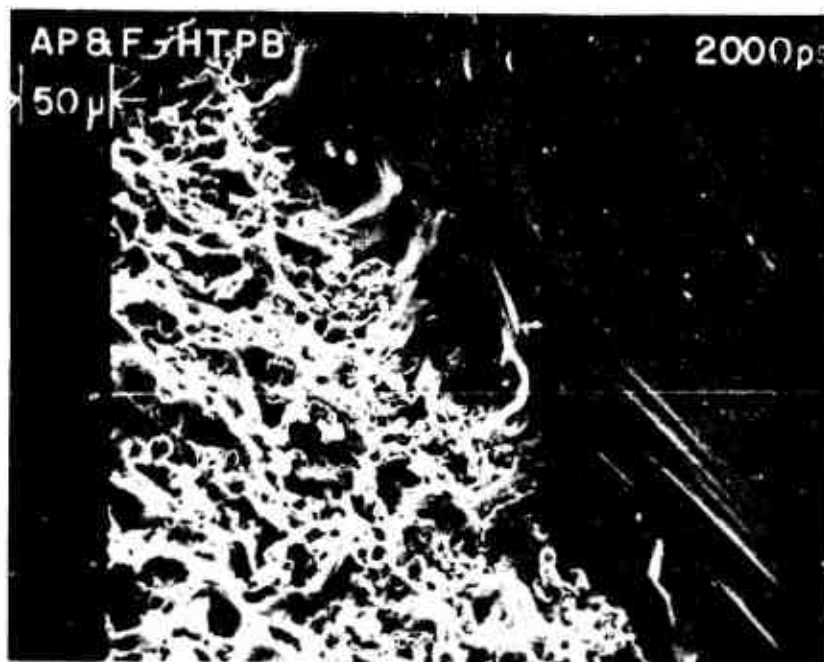


Figure III-45. AP and Ferrocene (F)-HTPB 2000 psia (x255).

There is a definite change in the surface composition for these cases as the pressure increases. Initially there seems to be little effect, while at the highest pressure the surface is completely different. The surface slope has remained essentially constant. This is in agreement with the cinephotomacrography results. The binder melt flow decreased as the pressure increased. This has allowed the point of maximum regression to be located very close to the binder-oxidizer interface at higher pressures.

AP and IB - HTPB.

600 psia. Figures III-35 and 46 -- Due to the use of triple sandwiches these micrographs are not in the proper order. The surface of the oxidizer appears to be very porous for this case. Again, particles of 20 μm diameter are visible on the surface. These appear red when viewed with the optical microscope. The binder melt flow is less than 30 μm . The slope at the binder oxidizer interface is continuous. There is indication of binder sag upon cooling.

1000 psia. Figures III-39, 47 and 48 -- The surface in this case closely resembles that of AP and F; the particles appear to be about the same size. There was a definite red residue on this sample, visible to the eye. The binder melt flow is less than 10 μm in extent. The slope is continuous at the interface and the radius of curvature of the surface is small.

1500 psia. Figures III-41, 49 and 56 -- The surface has a very porous appearance, again covered with a red residue. The binder melt flow extends up to 30 μm in sections, but is non-existent in others. The slope of the oxidizer surface has decreased as the pressure increased. There is no indication of cooling sags.



Figure III-46. HTPB-AP and Iron Blue (IB) 600 psia (x260).

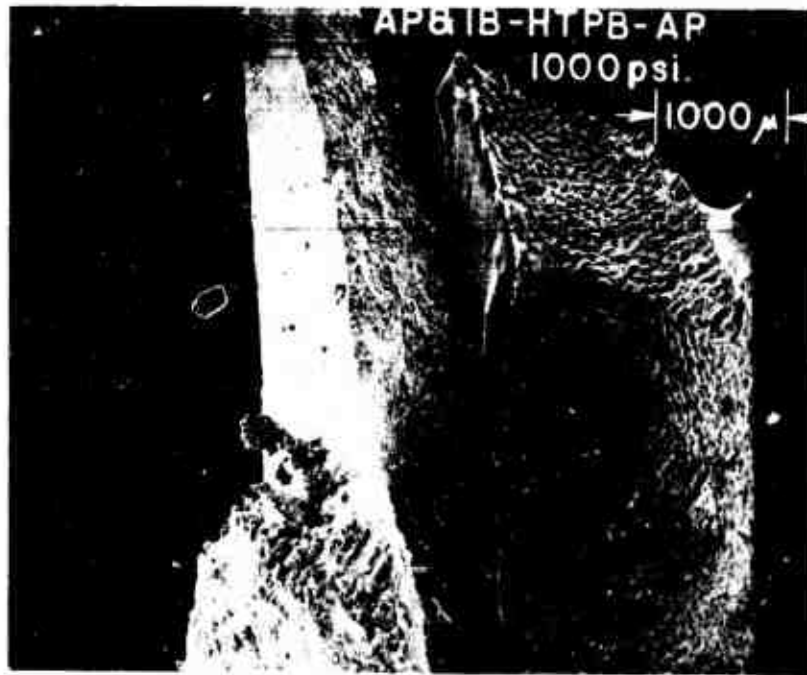


Figure III-47. AP and Iron Blue (IB)-HTPB-AP 1000 psia (x18.7).

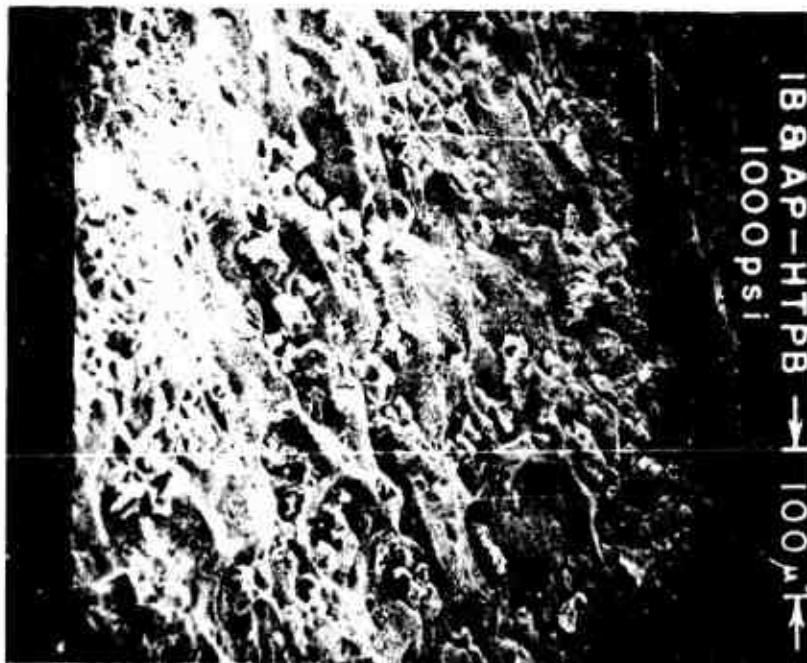


Figure III-48. AP and Iron Blue (IB)-HTPB 1000 psia (x196).

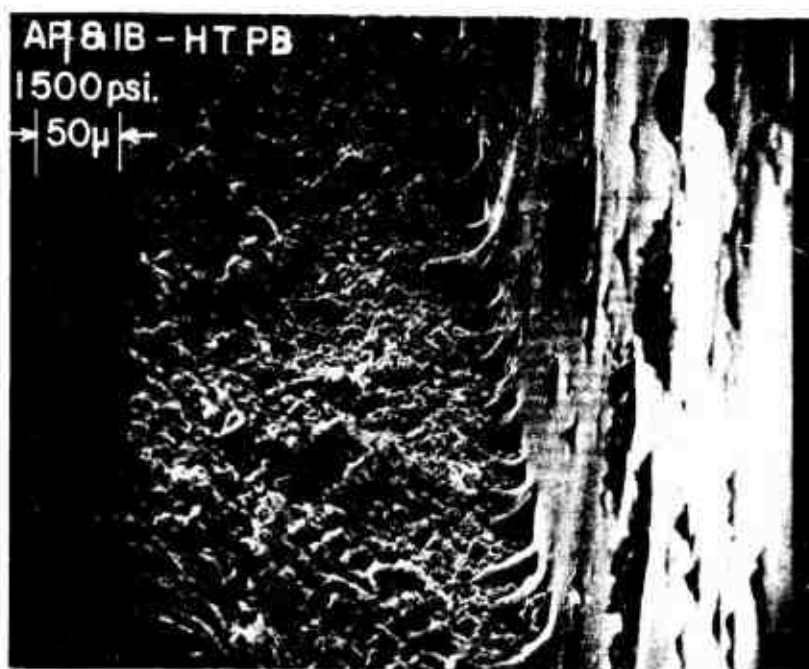


Figure III-49. AP and Iron Blue (IB)-HTPB 1500 psia (x230).

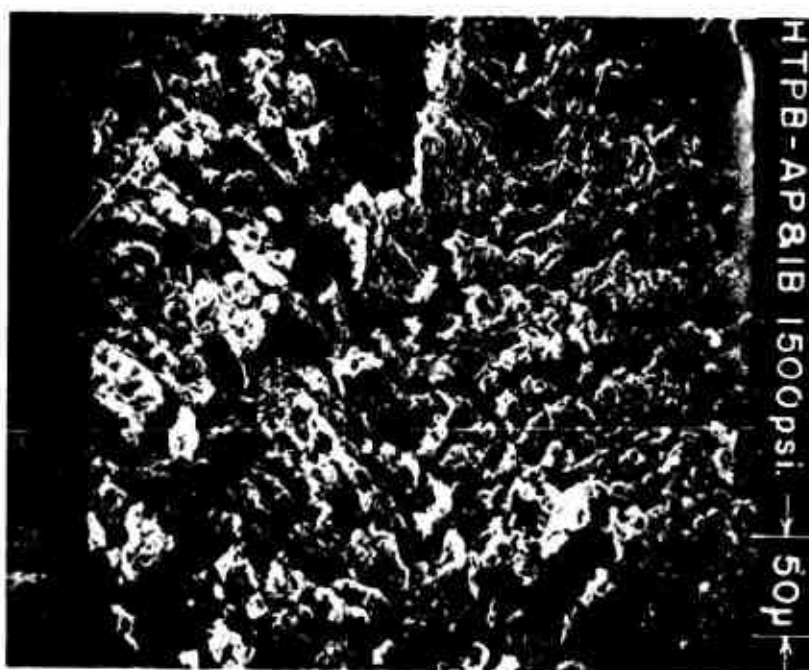


Figure III-50. AP and Iron Blue (IB)-HTPB 1500 psia (x270).

2000 psia. Figures III-51 and 52 -- The surface appears very porous with the indication of a crust coating which has been removed due to the depressurization process. There is no binder melt flow. There is considerable binder sag upon cooling with a possible indication of maximum regression in the binder. The surface slope has decreased for this case.

The surface of the AP and IB becomes smoother as the pressure increases. A surface coating of particles also increases. The slope of the surface decreases as the pressure increases and this was contrary to the cinephotomacrography results. A maximum slope of 64° was reached at 1500 psia for the movies.

Catalysts in the Binder

The following micrographs (Figures 53 through 79) show the details of the samples containing catalyst in the binder. All samples in this section were triple sandwiches allowing the comparison of two catalysts per run. A summary of these tests is given in Table III-3.

Several statements can be made which cover all four catalysts used in this phase of the investigation. There was no obvious change of the AP surface structure of these samples as compared to the pure AP-HTPB-AP sandwiches, which are used as standards of comparison. The binder melt flows are reduced or eliminated completely. The binder heights are reduced. In some cases it was impossible to determine a binder height due to the extensive sagging of the binder. The sagging and wrinkles in the solidified binder were much more noticeable in these samples. These binders seem to have higher viscosities. The binder melt flow decreased as the pressure increases. The binder-oxidizer interface slope is continuous for most

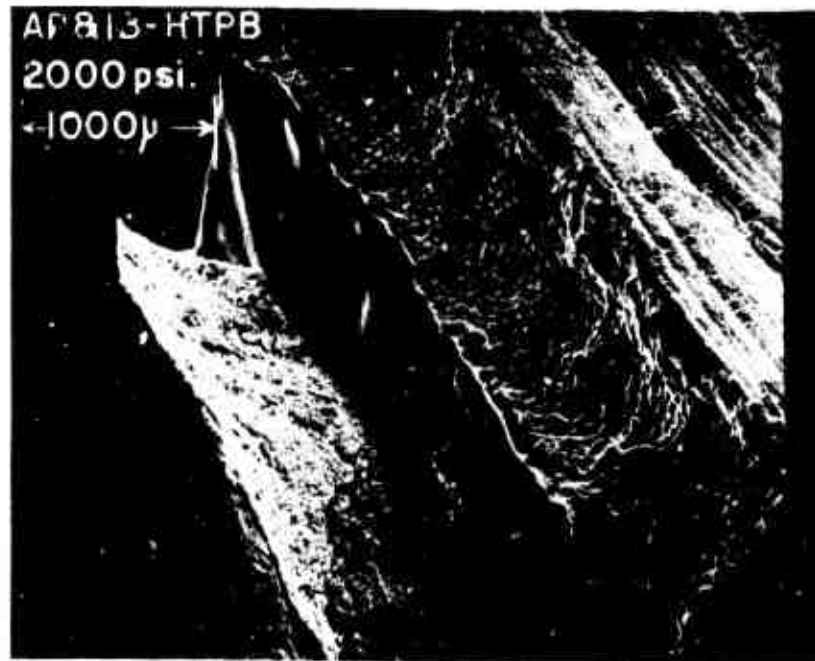


Figure III-51. AP and Iron Blue (IB)-HTPB 2000 psia (x26.5).

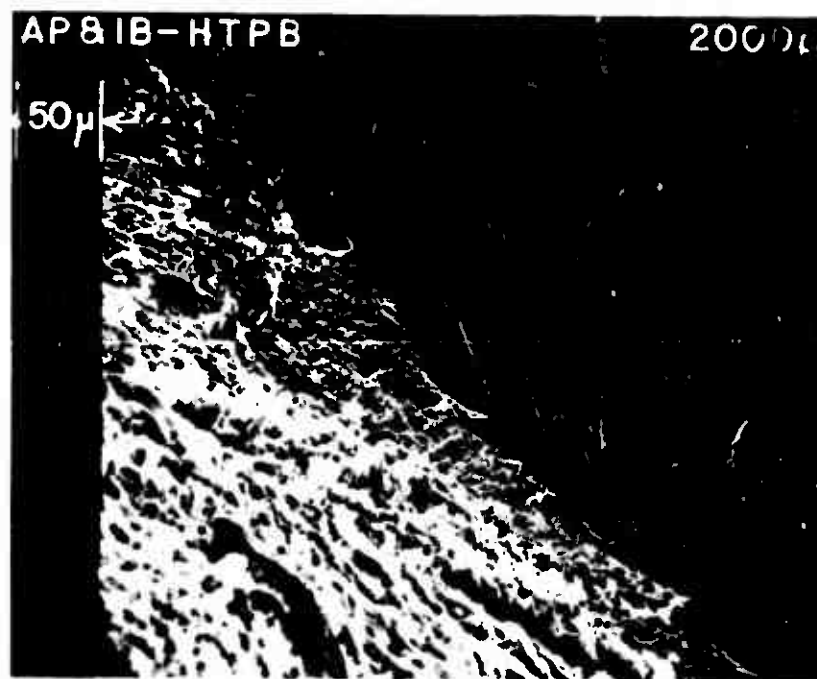


Figure III-52. AP and Iron Blue (IB-HTPB) 2000 psia (x240).

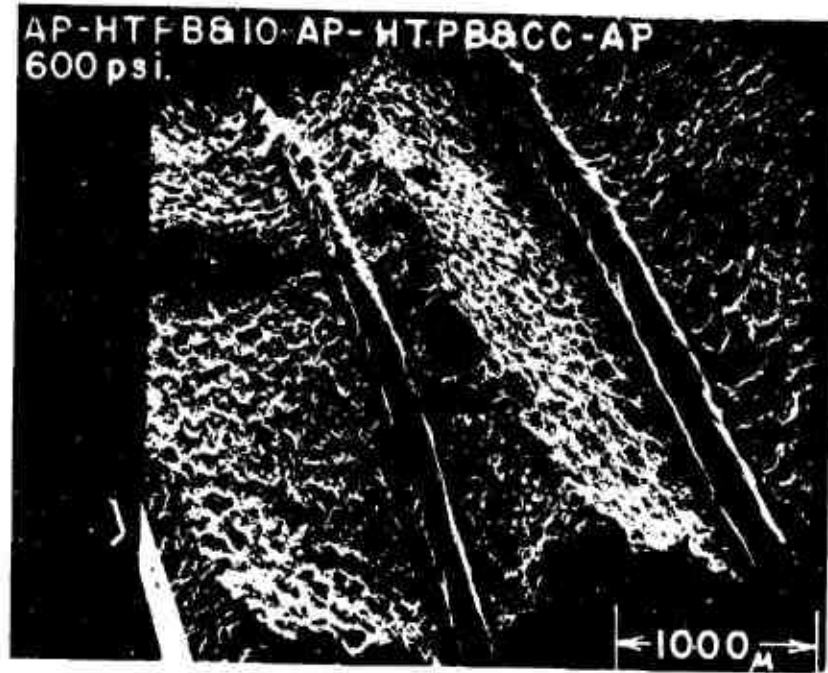


Figure III-53. AP-HTPB and Ferric Oxide (IO)-AP-HTPB and CuO₂O₂ (CC)-AP 600 psia (x28).



Figure III-54. AP-HTPB and CuO₂O₂ (CC)-AP 600 psia (x136).



Figure III-55. AP-HTPB and Ferric Oxide (IO)-AP 600 psia (x139).

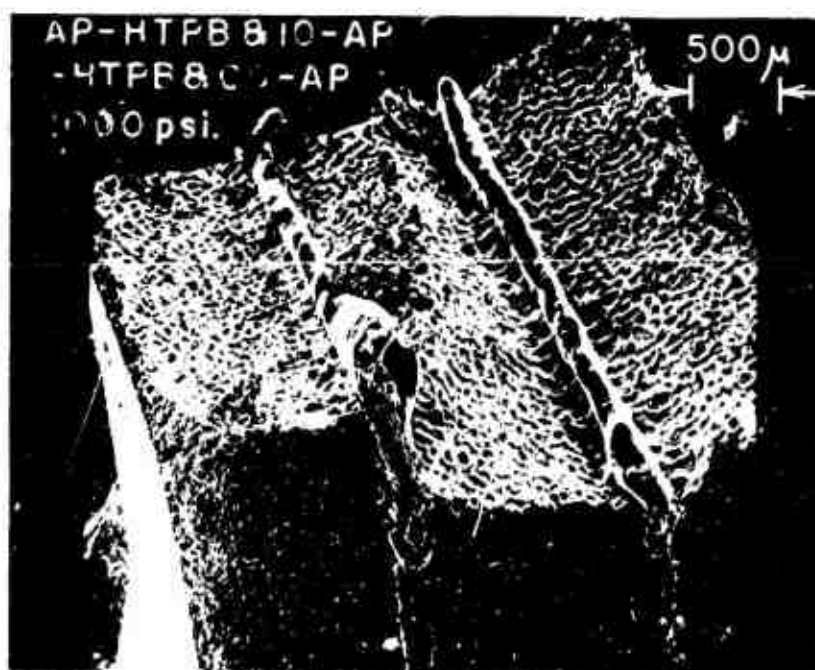


Figure III-56. AP-HTPB and Ferric Oxide (IO)-AP-HTPB and Cu₂O₂ (CC) 1000 psia (x214).



Figure III-57. AP-HTPB and CuO₂O₂ (CC)-AP 1000 psia (x116).



Figure III-58. AP and HTPB and Ferric Oxide (IO)-AP 1000 psia (x116).

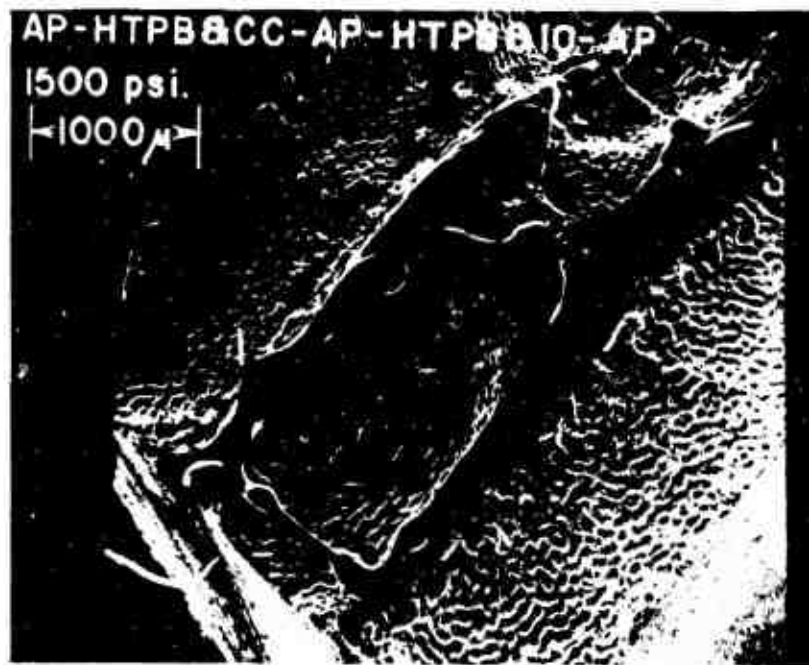


Figure III-59. AP-HTPB and Cu_2O_2 (CC)-AP-HTPB and Ferric Oxide (IO)-AP 1500 psia (x24).



Figure III-60. AP-HTPB and Cu_2O_2 (CC) 1500 psia (x223).

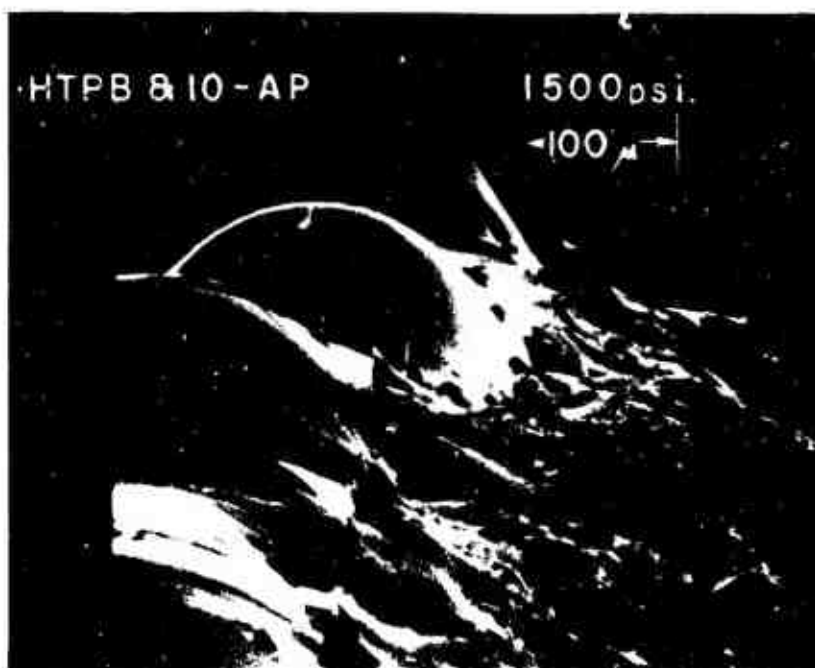


Figure III-61. HTPB and Ferric Oxide (IO)-AP 1500 psia (x210).

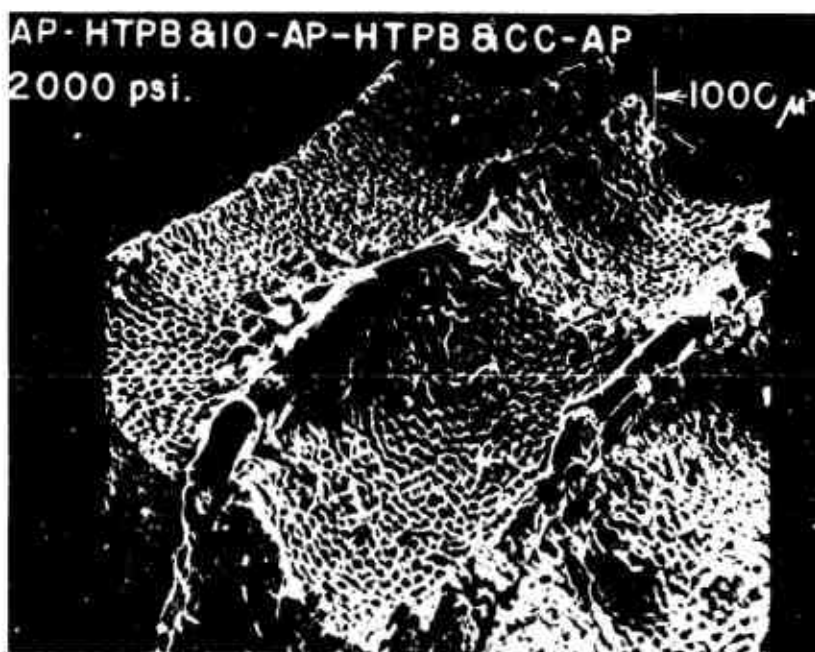


Figure III-62. AP-HTPB and Ferric Oxide (IO)-AP-HTPB and CuO₂ (CC) 2000 psia (x24).

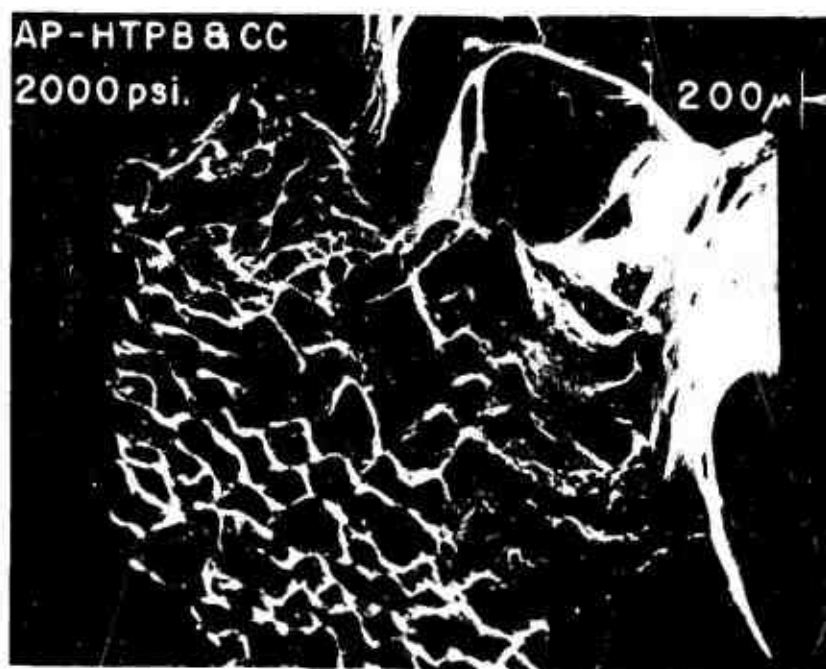


Figure III-63. AP-HTPB and Cu₂O₂ (CC) 2000 psia (x106).



Figure III-64. AP-HTPB and Ferric Oxide (IO) 2000 psia (x200).

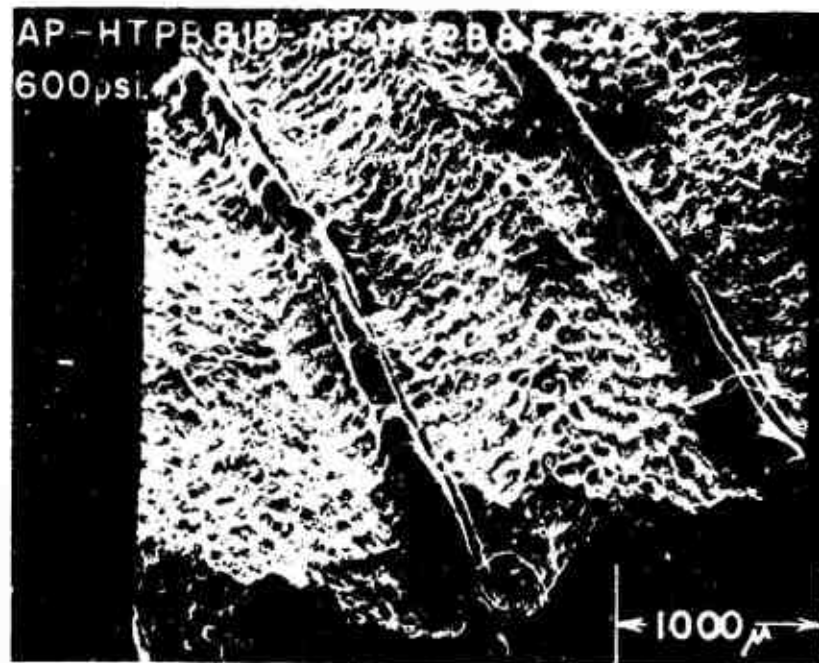


Figure III-65. AP-HTPB and Iron Blue (IB)-AP-HTPB and Ferrocene (F)-AP 1600 psia (x29).



Figure III-66. AP-HTPB and Ferrocene (F)-AP 600 psia (x135).



Figure III-67. AP-HTPB and Ferrocene (F)-AP 600 psia (x136).

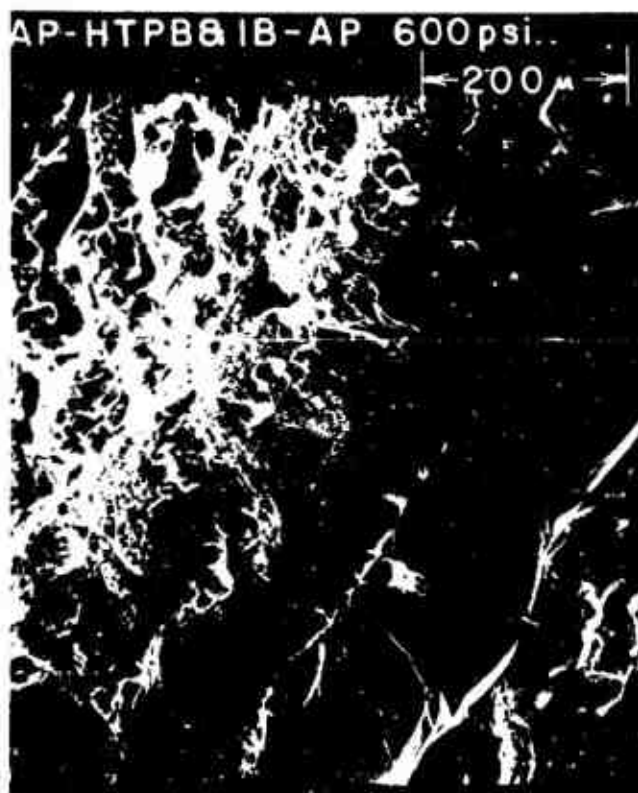


Figure III-68. AP-HTPB and Iron Blue (IB)-AP 600 psia (x143).



Figure III-69. AP-HTPB and Iron Blue (IB) 600 psia (x155).



Figure III-70. AP Bubble 600 psia (x1300).

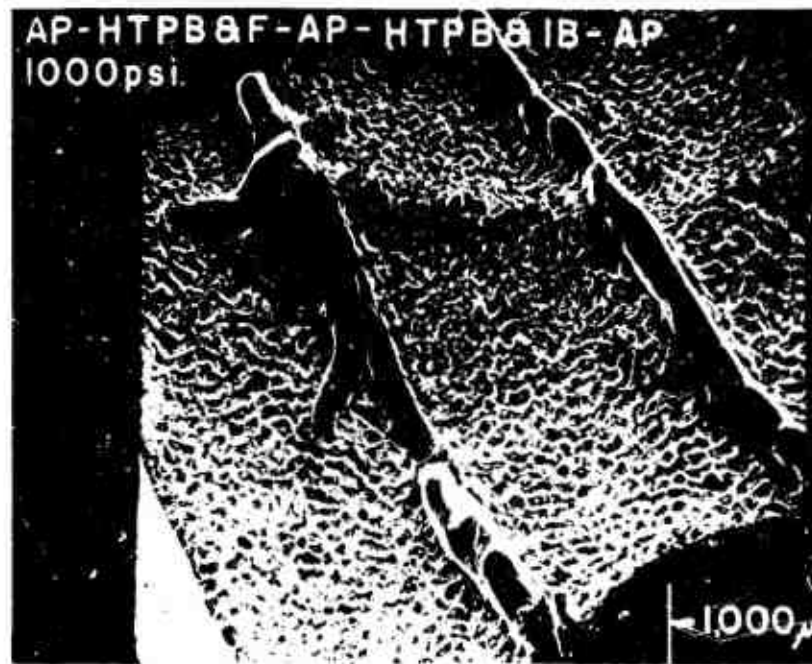


Figure III-71. AP-HTPB and Ferrocene (F)-AP-HTPB and Iron Blue (IB) 1000 psia (x27).



Figure III-72. AP-HTPB and Ferrocene (F) 1000 psia (x140).



Figure III-73. HTPB and Iron Blue (IB)-AP 1000 psia (x130).

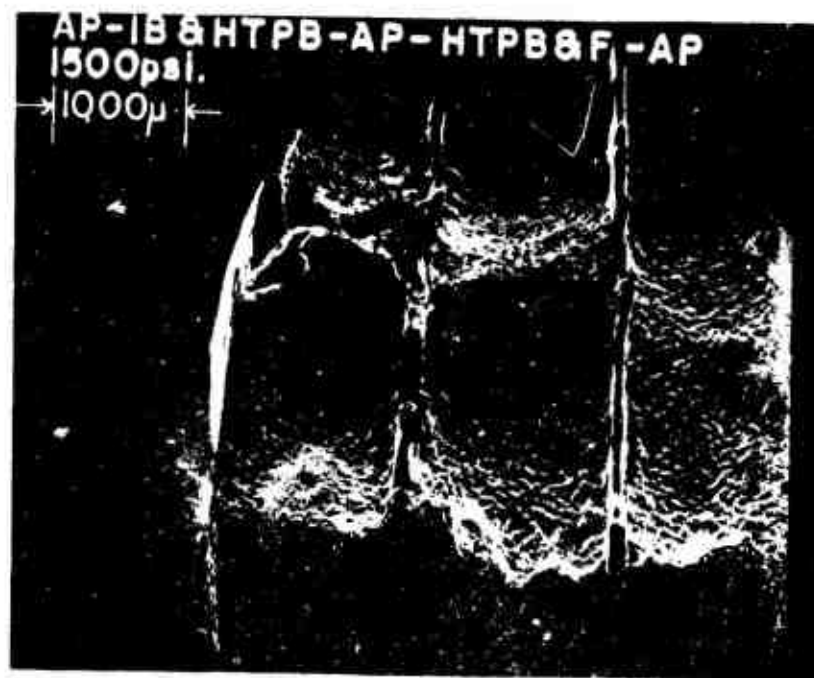


Figure III-74. AP-HTPB and Iron Blue (IB)-AP-HTPB and Ferrocene (F) 1500 psia (x18.7).

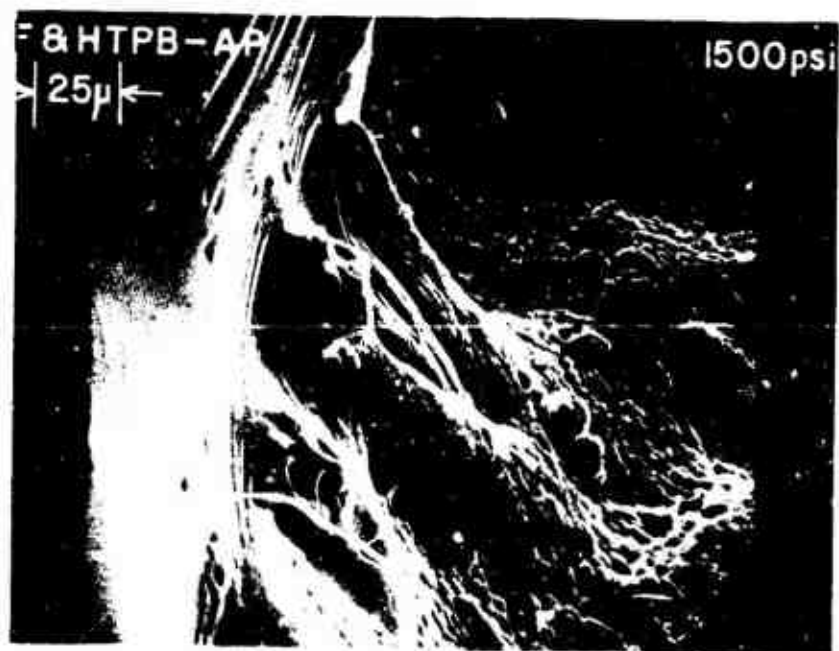


Figure III-75. HTPB and Ferrocene (F)-AP 1500 psia (x476).

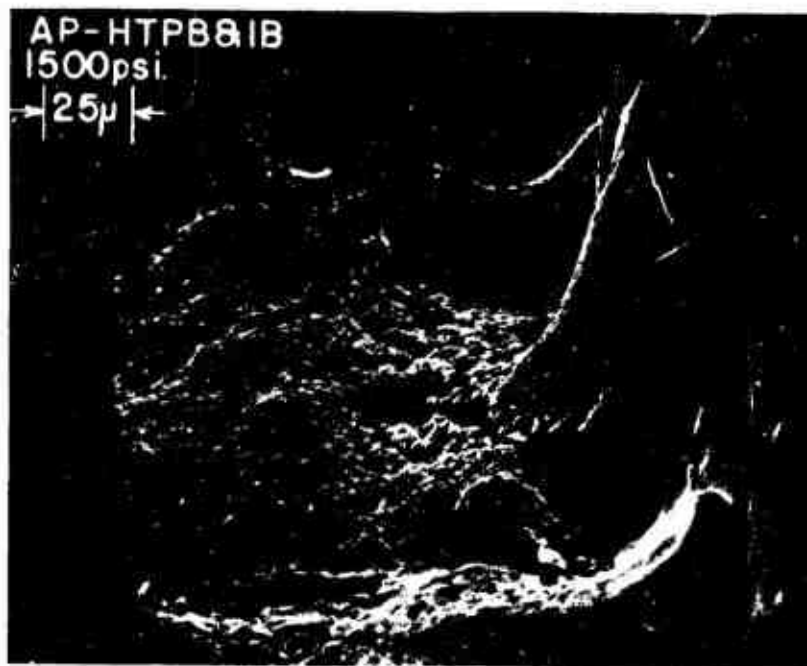


Figure III-76. AP-HTPB and Iron Blue (IB) 1500 psia (x476).

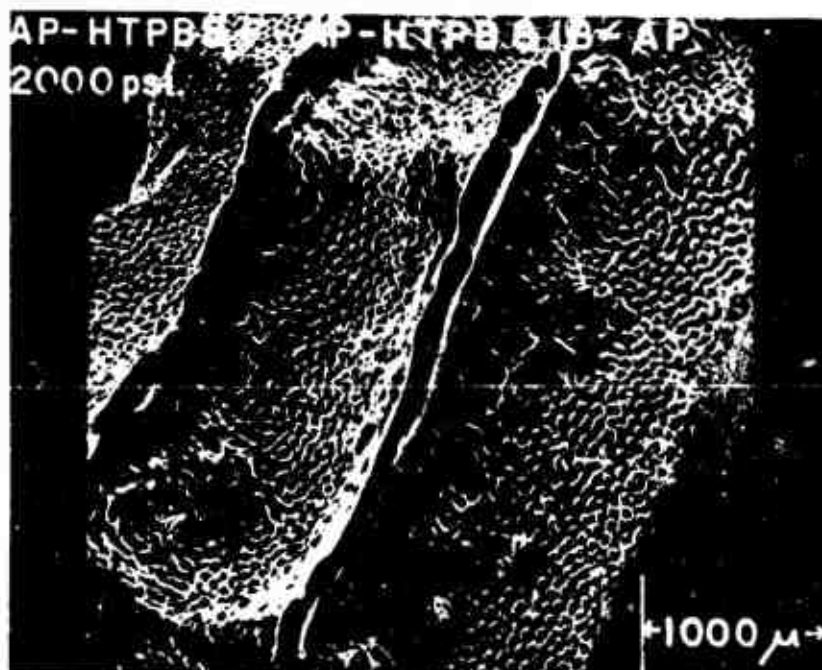


Figure III-77. AP-HTPB and Ferrocene (F)-AP-HTPB and Iron Blue (IB)-AP 2000 psia (x26).



Figure III-78. AP-HTPB and Ferrocene 2000 psia (x98).

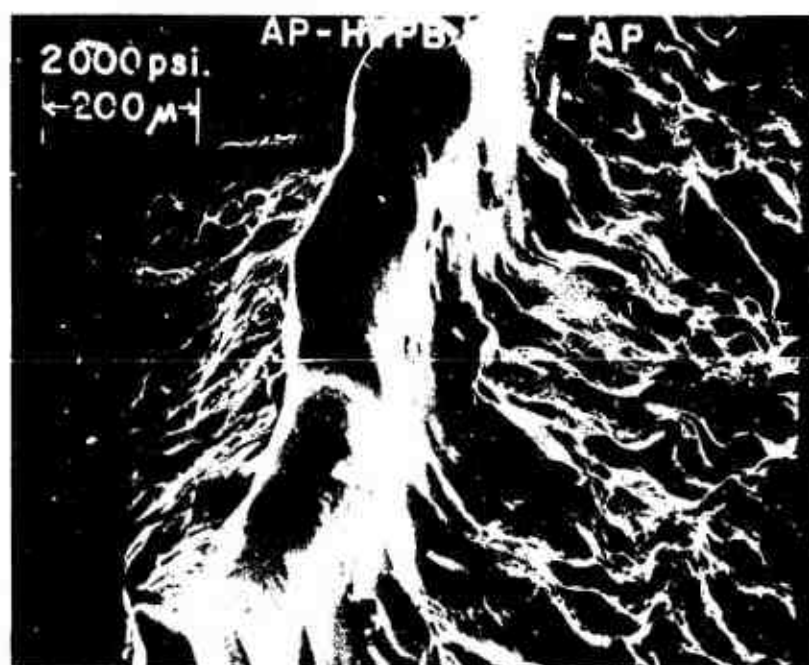


Figure III-79. AP-HTPB and Iron Blue (IB)-AP 2000 psia (x110).

Table III-3

Summary of Results from Scanning Electron Microscopy of Composite
Solid Propellant Sandwiches with Catalyst in the Binder

Catalyst	Location	Pressure psia	Figure No. III-	Binder Melt Flow μ m	Binder Height μ m
CuO ₂ O ₂ (CC)	in HTPB	600	53,54	100	130
		1000	56,57	120	350
		1500	59,60	50	undetermined
		2000	62,63	none	250
Ferric Oxide (IO)	in HTPB	600	53,55	70	170
		1000	56,58	60	190
		1500	59,61	none	120
		2000	62,64	none	undetermined
Ferrocene (F)	in HTPB	600	65,66,67	45	165
		1000	71,72	20	270
		1500	74,75	20	undetermined
		2000	77,78	none	200
Iron Blue (IB)	in HTPB	600	65,68, 69,70	100	200
		1000	71,73	50	280
		1500	74,76	none	undetermined
		2000	77,79	50	250

cases but tends to be discontinuous as the pressure increases.

Summary and Interpretation

The scanning electron microscope observations have both agreed and disagreed with the cinchphotomacrography results. The quenched samples have indicated higher oxidizer surface slopes as the pressure increases when CuO₂O₂ catalyst was added to the AP. This was not indicated by the

high speed movies. This indicates that CuO_2O_2 may be the most effective catalyst for addition in real propellants. The AP and IO quenched samples did not exhibit any variation in surface slope with pressure. This conflicted with a distinct decrease observed in the high speed movies.

The delay times obtained from the sample burn rate curves of Chapter II were used to obtain partially burned samples. There was no disagreement for the cases of catalyst in the binder or oxidizer. Discrepancies were encountered when the catalyst was located at the interface. The micrographs obtained for these samples are included in Appendix A.

The point of maximum regression of the oxidizer surface was always located at the edge of the binder melt flow. The slope of the binder oxidizer interface slope is only discontinuous for the case of no binder melt flow.

A primary observation is that all catalysts at all pressures reduce the binder melt flow extent when either loaded into the AP or into the binder. This is most probably some form of catalytic effect because it occurs at low pressures when the overall sandwich rates are not augmented over the pure HTPB-AP burn rates. Since the binder melt flows retard the pure AP rate, this could be an important mechanism for propellant catalysis.

Although there is some disagreement between surface slopes in catalyzed cases when viewed through cinephotomacrography and scanning electron microscopy, the former results are accepted for determination of catalytic effectiveness in Section V. The reasons for this acceptance are that a) no knowledge of post-quench surface alterations is at hand and b) direct observation of the complete burn during the cinephotomacrography runs has assured that a steady profile was developed.

IV. ELECTRON MICROPROBE EXPLORATORY STUDIES

An electron probe x-ray microanalysis has been performed on two pairs of samples. Both burned and unburned samples of pure AP and AP with 2% Iron Blue were examined. The analysis was performed in the Physical Science Division of the Engineering Experiment Station of the Georgia Institute of Technology using an Acton Laboratories Electron Probe x-ray Microanalyzer, Model MS-64. This analyzer is equipped with a light element detection system. It is possible to detect elements from boron, atomic number 5, to uranium, atomic number 92. This system cannot detect the four lightest elements, hydrogen, helium, lithium and beryllium.

The electron probe x-ray microanalyzer is an instrument used for x-ray spectrochemical analysis of surfaces between 0.5 to 200 μm diameter on the surface of a solid specimen. The instrument consists of three basic components, an electron beam similar to the SEM, an x-ray optical system with a suitable detector, and an optical microscope to select the area to be analyzed. The x-ray optical system is arranged to accept x-rays with an effective emergent angle of 18° from the specimen surface for all wavelengths. The optical microscope has a resolution of better than one μm with a magnification of 400x.

An electron beam size of 100 μm was used to investigate the oxidizer samples. This beam size was chosen to minimize damage to the surface by the electron beam. This would not have been as serious of a problem, if the sample were an electrical conductor. The electrons remain near the irradiation site for a nonconductor and create a negative charge which causes the beam to jump back and forth at random on the surface. This is accompanied by sparking

which rapidly deteriorates the sample surface. This type of damage was noted for all samples.

The electron micrographs of Chapter III were obtained by observing the secondary or backscattered electrons emitted by the sample as the electron beam of .01 μm diameter scanned the sample. These electrons are prevented from reaching the x-ray detector by an electron trap consisting of a permanent magnet with a special pole piece designed to deflect any electrons out of the x-ray path before they can enter the spectrometer chamber. These electrons cause a high background noise level if they reach the x-ray detector.

The analyzing electronics of the electron probe result in a strip chart record of the x-ray spectrum of the sample. These are shown in Figures IV-1 and 2. The ordinate of the spectrum is the variation in intensity of the x-rays, as obtained from a linear ratemeter which displays a signal that has been processed by a pulse-height analyzer system. The abscissa of the trace is the distance from the mica crystal to the sample. The known identification spectra for this microprobe are tabulated in this dimension, which can be converted directly to wavelength by the equation

$$\lambda(\text{\AA}) = 0.3978 L(\text{mm})$$

The pure AP sample spectra are shown in Figure IV-1. The unburned sample exhibited more damage due to the electron beam than the other three samples. No dominant chlorine peak was detected by the strip chart record, but a direct reading of the pulse height analyzer output before beam damage could be appreciable showed equal counts for chlorine for both the burned and unburned samples. A small amount of carbon was indicated in the burned sample. The amount was just above the limit of detectability. A slightly higher indication of oxygen was obtained.

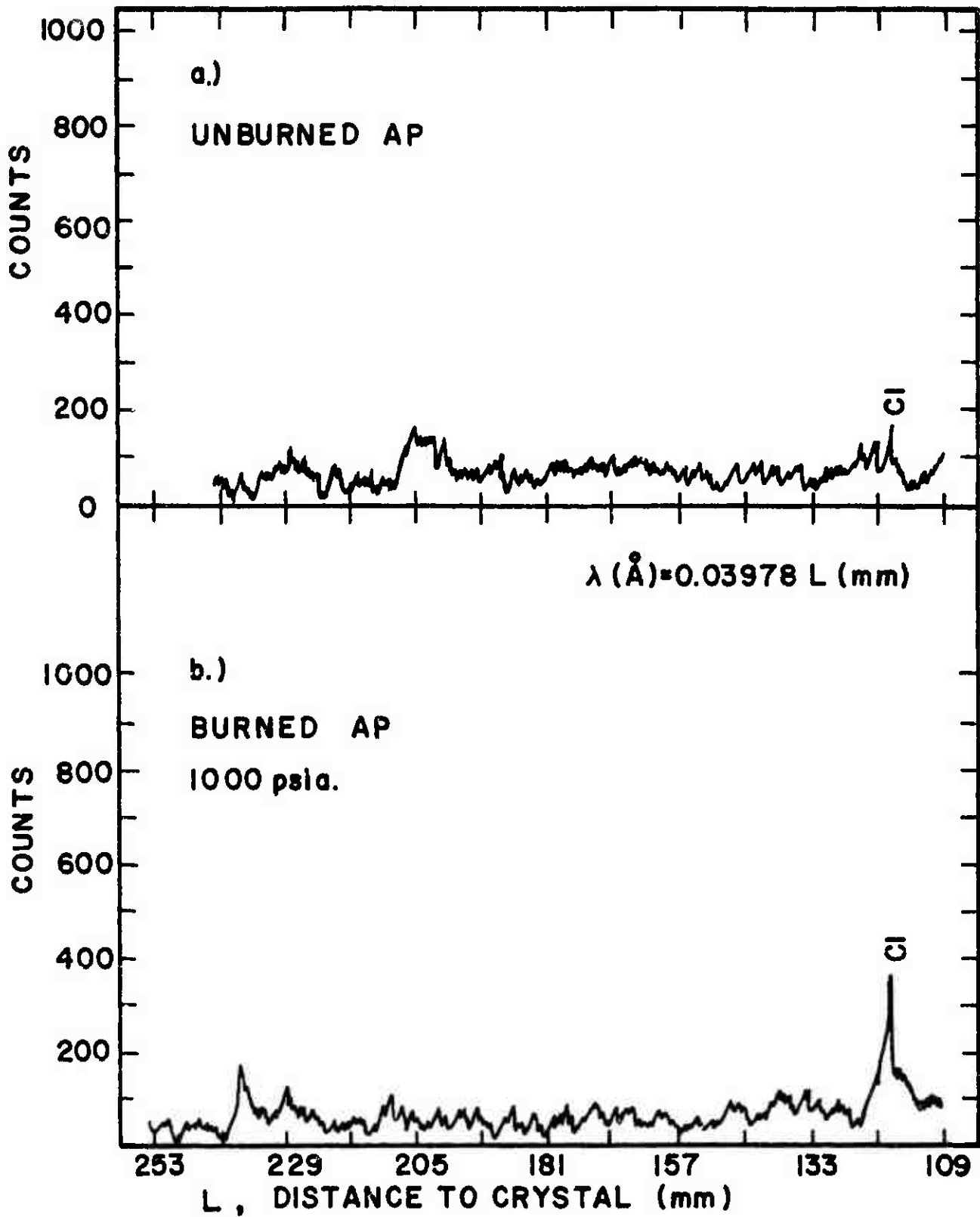


Figure IV-1. Characteristic X-Ray Spectra from Ammonium Perchlorate Samples.

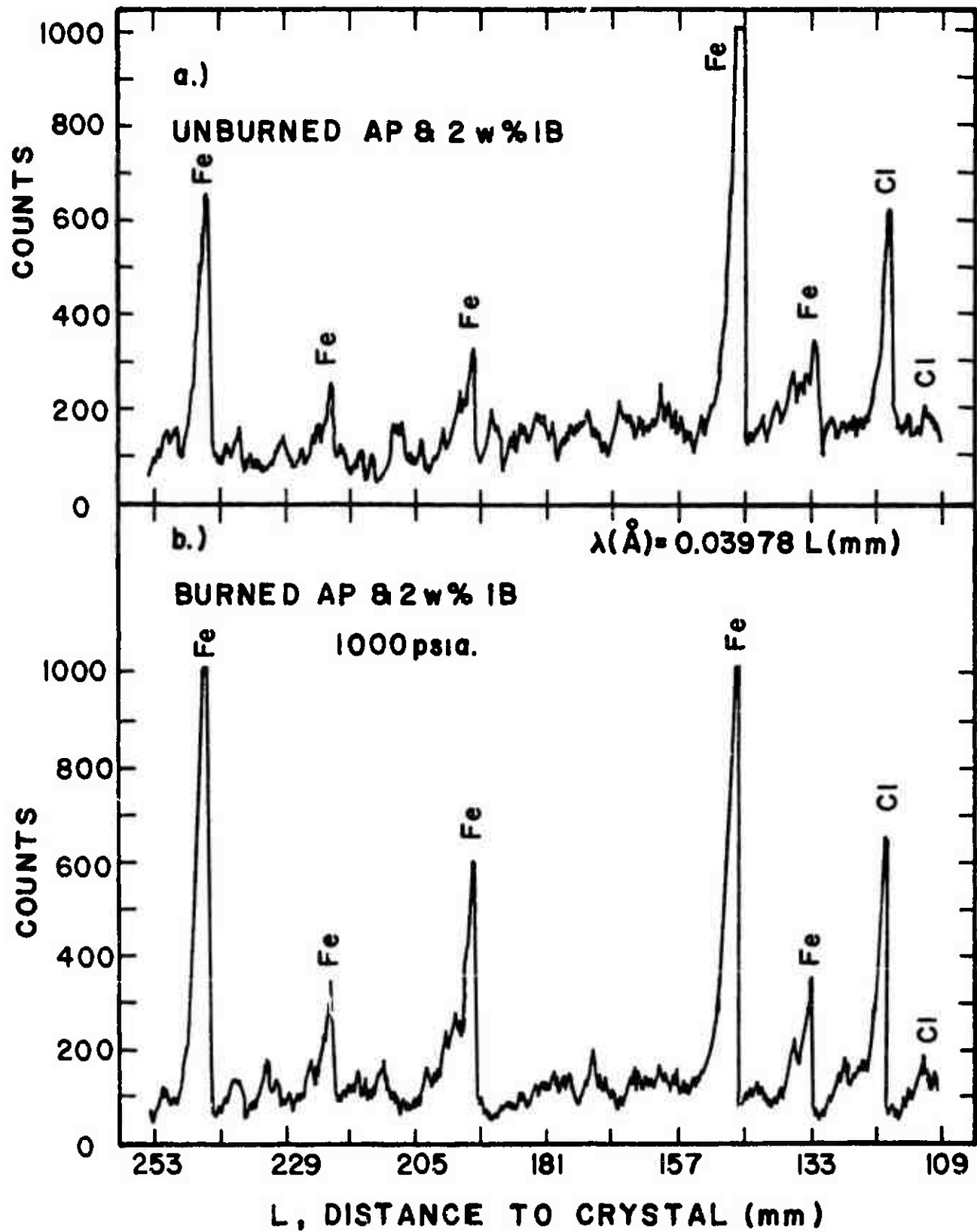


Figure IV-2. Characteristic X-Ray Spectra from Ammonium Perchlorate with 2% by Weight Iron Blue Samples.

The AP with 2% Iron Blue sample spectra are shown in Figure IV-2. The beam damaged these samples also. Quick counts were again taken to obtain a quantitative measure of the iron present in the samples. The unburned sample indicated a count equivalent to 3.06 weight % of a pure iron sample, while the burned sample showed a decrease to 2.60 weight %. This would be assuming the iron standard and the iron in the sample are in the same chemical state. This is not necessarily true here. There was an indication of sulfur present on the unburned sample but it was not present on the burned sample. The difference between the quick counts and the intensity of iron x-rays can be attributed to beam damage of the sample.

The results of the microprobe analysis were disappointing. A long delay was encountered in the analysis time due to equipment changes which had to be made with the light element detection system. It was felt that this time delay would result in quantitative measurements of relative concentrations of carbon, iron, nitrogen and oxygen. It is necessary to use special vacuum path with a 500 Å collodion window to isolate the detector from the sample for elements below an atomic number of 11. Since the only source of carbon and iron would be the iron blue with the chemical formula $\text{Fe}(\text{NH}_4)\text{Fe}(\text{CN})_6$ and the only source of oxygen and chlorine would be the ammonium perchlorate, NH_4ClO_4 , it was expected that a detailed quantitative chemical analysis of the surface layer of a burned and unburned sample would yield sufficient information to postulate the suitable chemical reactions which had taken place near the oxidizer surface. In some cases concentrations of one part in 10^5 have been reported by this type of microprobe analysis. If the reactions were known for the pure AP sample surface, then the significance of the catalyst, iron blue, could also be determined. As can

be seen from Figures IV-1 and 2 along with the discussion this was not possible. Because of the extremely long delay in analysis of these samples, it was not possible to formulate a new series of tests. It may have been possible to obtain suitable results without sample damage, if the electrically nonconducting samples had been coated as for the scanning electron microscope observations. No sample damage was detected during those observations with a much smaller, more intense beam, .01 μm as compared to 100 μm in diameter. The quick counts obtained at fixed detector locations would yield more accuracy than the entire spectrum scans. The fixed detector locations would be at known crystal distances for detection of x-ray radiation from specific elements. Further measurements would not be useful unless the light elements (below atomic number 12) could be detected with more accuracy.

V. RELEVANCE OF SANDWICH RESULTS TO COMPOSITE PROPELLANT BEHAVIOR

This section attempts to illustrate the use of mechanistic results inferred from sandwich tests to predict behavior in an actual composite propellant. The catalytic results mentioned in previous sections may be summarized by a) with the exception of IB and F below 800 psia addition of catalyst to the binder has no appreciable catalytic effect, b) with the exceptions of (i) CC above 1000 psia and (ii) IO above 1600 psia the primary catalytic mechanism appears to be augmentation of the binder-oxidizer gas phase kinetics and c) for the exceptions noted in b) the primary catalytic mechanism appears to be augmentation of the AP deflagration rate. In all cases it appears that through an unknown mechanism catalysts reduce the extent of binder melts and this may also be a rate-augmenting process. However, the primary differences between catalysts appear to lie in their ability to augment either the AP deflagration or the binder-oxidizer reaction kinetics. Furthermore, to make the binder-oxidizer reactions faster it appears desirable to introduce the catalyst from the AP side of the sandwich.

An indication for real propellants, which usually introduce the catalysts through a binder mix, is that the available surface area of AP should be made as large as possible (small particle size) to increase the probability of catalyst particles of reaching the hot gases of the AP decomposition and deflagration. This hypothesis will be tested below.

Since the catalyst is not usually loaded into the AP in a real propellant, the most likely mechanism for propellant catalysis would appear to be the enhancement of the binder-oxidizer reaction kinetics. Consequently, the sandwich indications along this line (separation of dashed and solid curves

in Figure II-2) should be directly applicable to propellant results. Summarizing the sandwich results and interpreting them insofar as propellant behavior is concerned, Table V-1 is constructed. The results of Table V-1 are only uncertain with regard to the strong AP enhancement of CC. If this mechanism does come into play in a real propellant the effects of CC could be underestimated at high pressure. Furthermore, IO behavior above 1200 psia could be underestimated.

Table V-1

Comparison of Catalyst Predictions in a Propellant Environment

Pressure	600-1000 psia	1000-1600 psia	1600-2000 psia
Observation	CC, IB, F, IO all equivalent in enhancing rate	IO, IB, F equivalent in enhancing rate. CC should be somewhat inferior	IB slightly superior to F which is slightly superior to IO which is superior to CC in rate augmentation

In order to test these predictions an unpublished Thiokol correlation formula for burn rate has been used⁽³⁾. Only IO and F catalysts were common to the Thiokol correlation and the current sandwich tests. The formula for HTPB binder reads

$$r(\text{in/sec}) = ap^n$$

$$a = \frac{1}{10} \left\{ \text{antilog}_{10} \left[-.497 + .91\bar{D}_1^2 + A_0\omega + A_1\omega^2 - .28b \right] \right\}$$

$$n = .239 + .744\bar{D}_1 - .707\bar{D}_1^2 + .00085q + B_0\omega + B_1\omega^2$$

$$\left. \begin{array}{l} b = \% \text{ binder} \\ q = \% \text{ AP} \\ \omega = \% \text{ catalyst} \end{array} \right\} \text{ by weight}$$

$$\bar{D}_1 = (q_1 + q_2 + \dots + q_n) / (q_1 D_1^3 + \dots + q_n D_n^3)$$

D_n = weight mean diameter of a given mode

	A_0	A_1	B_0	B_1
IO	-.301	.091	.191	-.049
F	.258	0	0	0

Sample results for a unimodal particle size distribution are shown in Figures V-1 and 2. The remaining ingredient percentage not indicated on the figures pertains to aluminum loading. Defining the catalyst effectiveness as the difference in burn rate between the catalyzed and no-catalysis cases, it is seen that the sandwich prediction of greater effectiveness as the AP size decreases is upheld.

With regard to pressure level the prediction of Table V-1 is correct in the 1000-1600 psia range; there is virtually no propellant difference between IO and F. F is somewhat better than IO at 600 psia, as seen in Figures V-1 and 2. This may be accounted for by the low pressure result with F that it becomes effective when located in the binder (see Figure II-3), in which case Table V-1 should be modified for IB also. In the pressure range 1600-2000 psia the propellant results show virtually no difference between F and IO whereas the sandwich results would predict a slight superiority of F. Again, this may be due to the action of IO on the AP deflagration, which was neglected in the construction of Table V-1. If this is the case, then the prediction for CC should be modified. By and large, however, the sandwich results predict that IO and F should be roughly equivalent and this is borne out experimentally for real propellants.

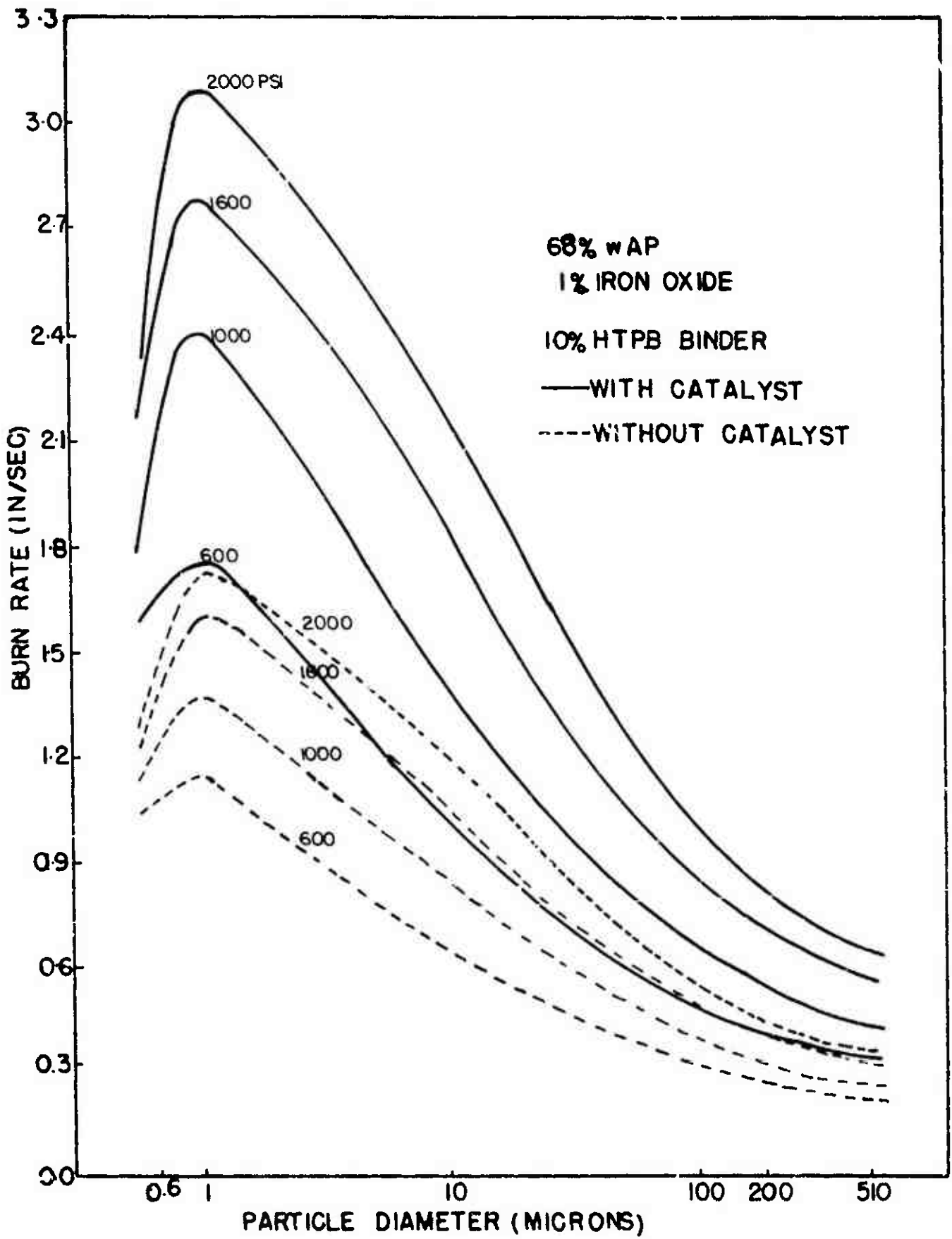


Figure V-1. The Effect of Iron Oxide Catalyst on HTPB-Al-Al Propellant.

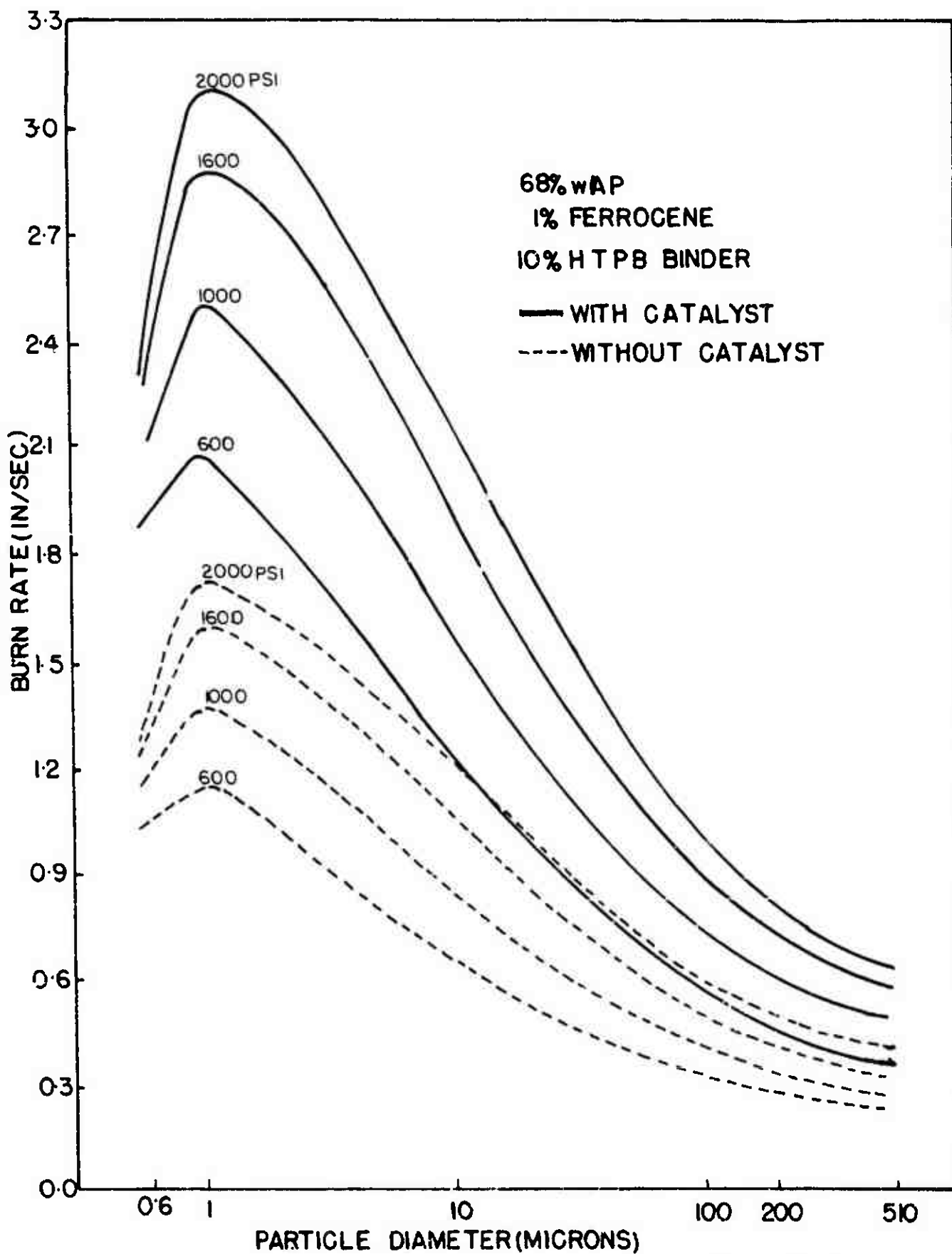


Figure V-2. The Effect of Ferrocene Catalyst on HTPB-AN-Al Propellants.

VI. SANDWICH ANALYSIS

Model Construction and Assumptions

As an aid in interpretation of experimental results it is desirable to have an analytical model of sandwich deflagration. Even in the two-dimensional case, however, the problem is highly complex due to a) an unknown surface shape, b) nonlinearities in the governing equations due to chemical reaction and the unknown surface shape, c) two phase heat transfer, d) multiple chemical reactions and e) a mathematically elliptic problem which reverts to a parabolic problem sufficiently far from the oxidizer surface (as will become apparent later). Accordingly, the maximum use of experimental information is sought which still does not restrict the usefulness of the model in understanding experimental results. The initial model therefore uses the following observations:

a) Far from the binder-oxidizer interface the AP regresses as pure AP. Furthermore, for binder thicknesses of the order used in the experimental studies ($\approx 150 \mu\text{m}$) there is little effect of one side of a sandwich upon the other side even when dissimilar materials are used. Therefore, the initial model development is concerned with a semi-infinite slab of AP against a semi-infinite slab of binder.

b) A steady state is achieved experimentally with AP oxidizer. Consequently, time dependence is assumed absent.

c) For uncatalyzed sandwiches the experimental results show very little effect of the binder-oxidizer reactions upon the surface profile. The initial model is therefore constructed assuming binder-oxidizer reactions to have negligible rate. Furthermore, the effect of catalysis is not treated.

The initial model therefore asks the question of the surface shape attained by a semi-infinite slab of AP which pyrolyzes a semi-infinite slab of binder. Posed in this manner it is immediately recognized that the problem has neither a unique solution nor a steady solution because a) the final shape would depend upon the geometry of ignition and b) it would take an infinite time to establish a steady profile in a semi-infinite slab of inert binder. The ignition problem is seen by imagining two cases - one in which ignition is achieved by a line heat source (say an ignition wire) and a second in which ignition is achieved uniformly over the entire AP surface. In the first case the AP would take on the shape of ever-increasing circular radii from the ignition point. In the second case the AP would deflagrate in a planar fashion except in the vicinity of the binder. For the current analytical model the second case will be assumed. The question of attainment of a steady binder profile can be answered by imposing a "local" steadiness in the vicinity of the binder-oxidizer interface. While it is true that far from the AP surface the binder will continually change shape, as it is eaten away by the hot AP deflagration gases, it is reasonable that for a certain distance (to be suggested by analysis) above the binder-oxidizer interface the binder shape will be time-invariant, after a certain ignition transient.

For this initial model the absence of binder melts will be assumed. The limits of validity will then be determined by comparison of the model and experimental results. For the AP deflagration process the Guirao-Williams model⁽⁹⁾ is accepted with an equilibrium assumption for the gas-solid interface. Some minor modifications are introduced into the model of

Reference (9) for computational convenience; these will be described below. Use of this model will restrict the sandwich theory validity to the pressure range 20-100 atm, because there is no AP theory capable of an explanation of observed phenomena above 100 atm.

Other usual assumptions are made to simplify the analysis which, while they lead to numerical errors of order unity, do not alter significantly the scaling rules developed with respect to other variables. These assumptions are: a) the thermal and transport processes of the solid AP and binder are identical, b) the thermal and transport properties of all gas phase species are identical, c) the Lewis number is everywhere unity in the gas phase, d) the deflagration process takes place at constant pressure, e) heat conduction and mass transfer take place by temperature and concentration gradients, only, respectively, and the transport coefficients are independent of temperature in both the solid and gas phases. A final major assumption is that on any vertical line parallel to the binder-oxidizer interface the ρv product (density times velocity) is that as determined in the solid phase and all lateral velocities are zero (strictly true in the solid phase). This is in the spirit of the Burke-Schumann approximation as expounded in Reference (10). This does yield error in convection effects upon heat transfer, but exact treatment of the problem is too complex.

The configuration is shown in Figure VI-1, in which the coordinate system is rendered stationary by a translation of the interface in the y direction at the rate v . Under the stated assumptions the equations for solution and the boundary conditions are:

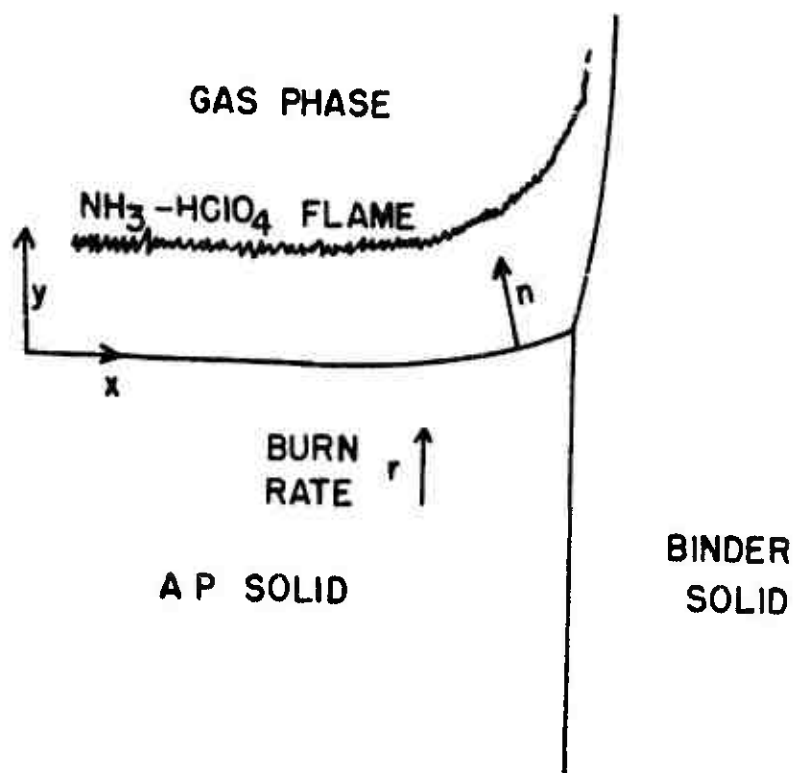


Figure VI-1. Sandwich Schematic and the Coordinate System.

Gas Phase Species Continuity

$$\frac{\lambda_g}{c_p} \left(\frac{\partial^2 Y_F}{\partial x^2} + \frac{\partial^2 Y_F}{\partial y^2} \right) = \rho v \frac{\partial Y_F}{\partial y} - w_F \quad (\text{VI-1})$$

Rate Law

$$w_F = -k Y_F^2 e^{-E_g/RT} \quad (\text{VI-2})$$

Gas Phase Heat Transfer

$$\lambda_g \left(\frac{\partial^2 T}{\partial x^2} + \frac{\partial^2 T}{\partial y^2} \right) = \rho v c_p \frac{\partial T}{\partial y} + 2q_R w_F \quad (\text{VI-3})$$

Solid Phase Heat Transfer

$$\lambda_s \left(\frac{\partial^2 T}{\partial x^2} + \frac{\partial^2 T}{\partial y^2} \right) = \rho v c_s \frac{\partial T}{\partial y} \quad (\text{VI-4})$$

Boundary Conditions

$$\begin{aligned} Y_F(x, \infty) &= 0 & Y_F(-\infty, y) &= \dot{Y}_F(y) \\ T(x, -\infty) &= T_0 & T(-\infty, y) &= \bar{T}(y) \\ T(\infty, y) &= T_0 & T(x, \infty) &= T_0 \end{aligned} \quad (\text{VI-5})$$

$$r_{n_B} = \vec{r} \cdot \vec{n}|_B = b_B e^{-E_{s_B}/RT_s} \quad (\text{VI-6})$$

$$\lambda_s \frac{\partial T}{\partial n}|_{s+} = \rho_s r_{n_B} q_s + \lambda_g \frac{\partial T}{\partial n}|_{s-} \quad (\text{VI-7})$$

$$\rho D \frac{\partial Y_F}{\partial n}|_{s+, \text{Air}} = -\rho_s r_{n_B} \left(\frac{1}{2} - Y_{F_s} \right) \quad (\text{VI-8})$$

$$p_{F_s} = b_F e^{-E_{s_F}/RT_s} \quad (\text{VI-9})$$

$$T \text{ continuous, } \nabla T \text{ continuous within a phase} \quad (\text{VI-10})$$

$$dy_s/dx(-\infty) = 0 \quad (\text{VI-11})$$

The products of AP gasification are assumed NH_3 and HClO_4 which are assumed identical molecules for mass transfer computation. k is a rate coefficient for the assumed second order reaction; $k \propto p^2$. The factor 2 in front of $q_{R,F}$ in Equation (VI-3) occurs because q_R is quoted per unit mass of AP rather than per unit mass NH_3 . The equilibrium interface on AP is specified through Equation (VI-9). This formulation, as far as the AP deflagration process is concerned, differs from that of Reference (9) in the following respects: a) no dilution of the NH_3 and HClO_4 is assumed at the solid-gas interface, although it is tacitly accounted for by the choice of a number for q_s ; b) calculations are simplified by taking the molecular weight of all species to be the same. The constants k and b_F will be so chosen to recover the same burn rate and surface temperature results as in Reference (9).

Equation (VI-6) is the pyrolysis law for the binder, Equation (VI-7) is the energy conservation law at the solid gas-interface, and Equation (VI-8) is the interface diffusion law. Note in Equation (VI-7) that q undergoes a discontinuity at the binder oxidizer interface and Equation (VI-8) is only valid on the AP side of the interface. Shown in Table VI-1 are typical values used in this work for the various parameters.

Mathematical Character of the Problem

In this problem r will be specified from known AP results since the assumption is, as verified by experiment, that far from the binder the AP

undergoes a pure AP planar regression. The quantities k and b_F will be picked to make the analysis consistent, given r . Equations (VI-1 - 4) define an elliptic problem in the sense that what happens at one point in the field affects every other point. Yet, if the binder is hard to decompose and it assumes a nearly vertical surface, it appears obvious that the picture becomes one of a (nearly) flat plate of binder over which hot AP gases are flowing. If the Reynolds number based on distance along the binder were large enough this would revert to a parabolic problem because $\partial/\partial x \gg \partial/\partial y$ would result. However, exactly at the binder-oxidizer interface, the Reynolds number is zero. Since it is precisely this region that is of interest, the full elliptic problem must be solved. In order to gain an idea of magnitudes involved here the equations are nondimensionalized with respect to a distance scale α_s/r and temperature T_0 . Heats of gasification are made dimensionless by $c_p T_0$ and activation energies by RT_0 . The result is the following set of equations and boundary conditions:

$$Y_{F_{xx}} + Y_{F_{yy}} = \xi Y_{F_y} - \tilde{k} Y_{F_e}^2 e^{-\epsilon/g}$$

$$\text{(Gas)} \quad g_{xx} + g_{yy} = \xi g_y + 2q_R \tilde{k} Y_{F_e}^2 e^{-\epsilon/g}$$

$$\text{(Solid)} \quad g_{xx} + g_{yy} = \xi g_y$$

$$Y_F(x, \infty) = 0$$

$$Y_F(-\infty, y) = \bar{Y}_F(y)$$

$$g(x, -\infty) = 1$$

$$g(-\infty, y) = \bar{g}(y)$$

$$g(\infty, y) = 1$$

$$g(x, \infty) = 1$$

$$1/z_B = \tilde{b}_B e^{-\epsilon_{S_B}/g_s}$$

$$\partial g / \partial n|_{s+} = \xi \left[q_s / z + \tilde{\eta} \partial g / \partial n|_{s-} \right]$$

$$\frac{\partial Y_{F_s}}{\partial n}|_{s+} = - \xi \left(\frac{1}{z} - Y_{F_s} \right) \quad (\text{VI-12})$$

$$Y_{F_s} = \tilde{b}_F e^{-e_{s_F} / g_s}$$

g continuous, ∇g continuous within a phase

$$y_s'(-\infty) = 0$$

Table VI-1

Numerical Values for Various Parameters

Quantity	Value	Reference
T_0	300°K	Assumed
ρ_s	1.95 gm/cm ³	9
c_p	.3 cal/gm°K	9
c_s	.3 cal/gm°K	9
q_R	172 cal/gm	[to yield flame temperature] [of 1205°K of Ref. (9)]
$q_{s_{AP}}$	-100 cal/gm	9
λ_g	10^{-4} cal/cm sec°K	9
λ_s	9×10^{-4} cal/cm sec°K.	9
E_g	15 kcal/mole	9
E_s	30 kcal/mole	9
E_{s_B}	8.7 - 17 kcal/mole	11
b_B	1 - 150 cm/sec	11
q_{s_B}	260 - 1004 cal/gm	11

The dimension α_s/r is known to be the "thickness" of the thermal wave which would occur in a planar regression. It is the reference dimension here. The parameter ξ in Equations (VI-12) is nothing more than the ratio of a characteristic solid phase dimension (α_s/r) to the characteristic gas phase dimension (α_g/v). If there were no modification due to the reaction rate term, the gas phase distance over which significant heat transfer would occur would be of the order of α_g/v . Using the parameters of Table VI-1, $\xi = 9.0$, showing that the gas and solid phase characteristic scales are quite different. Furthermore, constructing the Reynolds number based upon y , it is found that $Re_y = \xi y$, so that when y is of the order of $1/\xi$ a transition is taking place between "low" and "high" Reynolds numbers. If important field quantity variations are taking place only over a gas phase distance of the order of $1/\xi$, the problem must be treated as elliptic with no simplifications possible through a boundary layer assumption.

One characteristic of the problem does aid in simplifying the problem, however. The expectation is that fixing x and moving vertically above the surface the temperature would increase, reach a maximum near the point of reaction completion and then slowly decay due to heat transfer to the binder. This suggests the approximation that the temperature maximizes for fixed x at a point y where the reaction is complete. This will be adopted as an assumption and its use will be illustrated below. It is this assumption which allows a rather simple solution to be constructed.

That the problem is nonlinear can be easily seen in the chemical reaction times. A more subtle nonlinearity, arising from an unknown surface shape, can be best seen by changing the coordinate system from x, y to $x, \eta = y - y_s(x)$. Now all boundary conditions may be applied at the point

$\eta = 0$. Equations VI-12 become

$$Y_{F_{xx}} + z^2 Y_{F_{\eta\eta}} - 2y'_s Y_{F_{\eta x}} - y''_s Y_{F_{\eta}} = \xi Y_{F_{\eta}} - \tilde{k} Y_F^2 e^{-\epsilon/g}$$

(Gas)
$$g_{xx} + z^2 g_{\eta\eta} - 2y'_s g_{\eta x} - y''_s g_{\eta} = \xi g_{\eta} + 2q_R \tilde{k} Y_F^2 e^{-\epsilon/g}$$
 (VI-13)

(Solid)
$$g_{xx} + z^2 g_{\eta\eta} - 2y'_s g_{\eta x} - y''_s g_{\eta} = g_{\eta}$$

Since y'_s is an unknown, the nonlinear appearance of Equations (VI-13) is apparent.

Solution by an Integral Technique

Pure AP Deflagration. Far from the binder the AP must undergo a planar deflagration. In this case Equations (VI-13) become

$$\bar{Y}_{F_{\eta\eta}} = \xi \bar{Y}_{F_{\eta}} - \tilde{k} \bar{Y}_F^2 e^{-\epsilon/g}$$

Gas
$$\bar{g}_{\eta\eta} = \xi \bar{g}_{\eta} + 2q_R \tilde{k} \bar{Y}_F^2 e^{-\epsilon/g}$$

Solid
$$\bar{g}_{\eta\eta} = \bar{g}_{\eta}$$
 (VI-14)

with the boundary conditions from Equations (VI-12) as

$$\bar{g}(-\infty) = 1 \qquad \bar{g}(\infty) = \bar{g}_f$$

$$\bar{T}_{\eta}(0) = \xi \left[a_s + \tilde{\eta} \bar{T}_{\eta}(0) \right]_s$$

$$\bar{Y}_F(\infty) = 0 \qquad \text{(VI-15)}$$

$$\bar{Y}_{F_{\eta}}(0) = -\xi \left(\frac{1}{2} - \bar{Y}_{F_s} \right)$$

$$\bar{Y}_{F_s} = \tilde{b}_F e^{-\epsilon/g_s}$$

where the only independent variable is now η . A first integral of Equations (VI-14) subject to Equations (VI-15) is

$$\bar{g}(\eta) + 2q_R \bar{Y}_F(\eta) = \bar{g}_s + 2q_R \bar{Y}_{F_s} = \bar{g}_f \quad (\text{VI-16})$$

To gain an approximate solution to Equations (VI-14) let

$$\bar{Y}_F = \bar{Y}_{F_s} [1 - f(\eta/c)] \quad ; \quad \bar{g} - \bar{g}_s = (\bar{g}_f - \bar{g}_s) f(\eta/c)$$

where $f(0) = 0$, $f(1) = 1$ and c is the flame standoff distance. For simplicity, let $f = \eta/c$ and place this approximate form into the reaction rate expression of Equations (VI-14). Integrating the gas phase equations once and the solid phase equations twice yields

$$\text{(Solid)} \quad (\bar{g} - 1) = (\bar{g}_s - 1) e^{\eta}$$

$$\text{(Gas)} \quad Y_{F\eta} - \bar{Y}_{F\eta}(0) = (\bar{Y}_F - \bar{Y}_{F_s}) \xi - Q(\eta) \quad (\text{VI-17})$$

$$\bar{g}_\eta - \bar{g}_\eta(c) = \xi(\bar{g} - \bar{g}_s) + 2q_R Q(\eta)$$

$$Q(\eta) = \tilde{k} \bar{Y}_{F_s}^2 \int_0^\eta (1 - \eta/c)^2 e^{-\xi} / [\bar{g}_s + (\bar{g}_f - \bar{g}_s) \eta/c] d\eta$$

Furthermore, an overall energy balance yields

$$\bar{g}_f - \bar{g}_s = q_R - q_s - \tilde{\eta}(\bar{g}_s - 1) \quad (\text{VI-18})$$

which is the equation for the adiabatic flame temperature. Evaluation of Equations (VI-17) at $\eta = c$ and applying Equations (VI-15) there results

$$c = \bar{Y}_{F_s} / \xi (1/c - \bar{Y}_{F_s})$$

$$Q(c) = \bar{Y}_{F_s} \left(\frac{1}{c} + \xi \right) \quad (\text{VI-19})$$

$$\bar{Y}_{F_s} = \tilde{b}_F e^{-E_{sF} / \bar{g}_s}$$

The procedure to complete the solution is the following: a) \bar{g}_s as a function of pressure is taken from Reference (9); b) Equation (VI-18) yields \bar{g}_F (which is actually constant here because $\tilde{\eta} = 1$ and q_R and q_s are assumed independent of pressure); c) Equation (VI-16) determines \bar{Y}_{F_s} ; d) Equations (VI-19) determine c , \tilde{b}_F and \tilde{k} .

From the nondimensionalization procedure it may be checked that $\tilde{k} \propto p^2 / \bar{r}^2$. Therefore, if the rate, \bar{r} , is known at one pressure, it is known as a function of pressure. Shown in Table VI-2 are complete calculations for two sample pressures.

Table VI-2

One Dimensional AP Deflagration Results

p (atm)	\bar{r} (cm/sec)	α_s/r (μm)	\bar{T}_s ($^\circ\text{K}$)	\bar{g}_s	\bar{Y}_{F_s}	\bar{g}_F	c	b_F (atm)	\tilde{k}
54.4	.735	20.9	990	2.93	.285	4.022	.1471	4.38×10^8	2.62×10^6
100.0	1.000	15.3	911	3.04	.258	4.022	.1183	4.06×10^8	3.39×10^6

In Table VI-2 it will be noted that b_F is not quite constant. This is due to the use of a slightly higher E_{sF} than in Reference (9). Furthermore, \tilde{k} is not quite proportional to $(p/\bar{r})^2$. This is due to the fact that \bar{r} in Table VI-2 is the experimental value and it is known that between the two

values of pressure of Table VI-2 the theory of Reference (9) slightly overestimates the pressure sensitivity of the deflagration rate. These details are not considered important for the current theory because a precise model for AP deflagration is not sought; only the deviations from a planar regression, due to the binder essence , are required and the above theory appears adequate to serve as a baseline for perturbations due to the binder.

Perturbed Solution. Upon extensive investigation of the partial differential equations for small deviations from the one-dimensional regression it was determined that a) the deviations from the planar case in the gas phase could be expected to be simple deviations from the planar solution, but b) the solid phase deviations may be complex. By "simple" it is meant that the deviation is not oscillatory. Thus, if $g(x,y) = \bar{g}(x) + G(x,y)$ where $G(x,y)$ is the deviation from the pure AP case, $G(x,y)$ may be expected to have monotonic behavior in y between the two end values $G[x,y_g(x)]$ and $G[x,y_f(x)]$. Therefore, it was decided to attempt an integral solution where

$$Y_F = Y_{F_s}(x) \left[1 - \frac{\eta}{c(x)} \right] \quad (VI-20)$$

$$g - g_s(x) = \left[\bar{g}_1(x) - \bar{g}_s(x) \right] \frac{\eta}{c}$$

are guessed forms of the solution. Equations (VI-20) are placed in Equations (VI-13) after an integration over η from $\eta = 0$ to $\eta = c$. The resulting nonlinear ordinary differential equations for the gas phase are

$$\left(Y_{F_s} \frac{c}{2} \right)'' = Q(c) - Y_{F_s} \left(\xi + \frac{z^2}{c} \right) - 2y_s' Y_{F_s}' - y_s'' Y_{F_s} \quad (\text{VI-21})$$

$$\begin{aligned} \left[(g_1 + g_s) \frac{c}{2} \right]'' &= -2q_R Q + \xi(g_1 - g_s) + c'' g_1 \\ &+ y_s''(g_1 - g_s) + 2y_s'(g_1' - g_s') + 2c' g_1' \end{aligned}$$

The unknowns here are Y_{F_s} , c , y_s' , g_1 and g_s . The boundary conditions from Equations (VI-12) become, using the assumed functional form of Equations (VI-20)

$$\begin{aligned} Y_{F_s}(-\infty) &= \bar{Y}_{F_s} & g_1(-\infty) &= \bar{g}_1 \\ g_s(-\infty) &= \bar{g}_s & c(-\infty) &= \bar{c} \\ \bar{y}_s(-\infty) &= 0 \end{aligned}$$

$$\begin{aligned} y_s' Y_{F_s}' &= \xi \left(\frac{1}{2} - Y_{F_s} \right) - \frac{z^2 Y_{F_s}}{c} \\ \left(\frac{g_1 - g_s}{c} \right) z + \left(\frac{y_s' g_s'}{z} \right) &= \xi \left[\frac{q_s}{z} + \tilde{\eta} \frac{\partial g}{\partial n} \Big|_s \right] \end{aligned} \quad (\text{VI-22})$$

$$Y_{F_s} = \tilde{b}_{F_s} e^{-\epsilon_{sF} / g_s}$$

The first five of Equations (VI-22) are the left hand boundary conditions on the five unknowns of the ordinary differential equations, Equations (VI-21). The next two equations of Equations (VI-22) are the surface diffusion and heat transport relations, which form two more differential equations for the unknowns. The last of Equations (VI-22) is an algebraic relation between the unknowns. The system would be closed except for the

appearance of $\partial g/\partial n|_s$, so that the solid phase, of course, must be treated. A major difficulty in solution of the nonlinear problem may be seen in the terms $y'_s Y'_{F_s}$ and $y'_s g'_s$ of Equations (VI-22). At points of zero slope, $y'_s = 0$, a solution for g'_s and Y'_{F_s} is singular.

This singularity may be circumvented by first searching for asymptotic solutions to the problem which consists of the AP solution plus a small perturbation. The problem for the perturbation will be linear and the terms $y'_s g'_s$ and $y'_s Y'_{F_s}$ will be second order quantities (because $y'_s(-\infty)$ and $Y'_{F_s}(-\infty)$ are zero for the AP solution). Since this asymptotic solution would be required anyway because of the inability to carry out a machine integration to $x = -\infty$, this solution will be constructed. It will be seen below that this is all that is required for binder properties of usual interest.

Accordingly, the following forms are assumed:

$$\begin{aligned} Y_{F_s} &= \bar{Y}_{F_s} + v_{F_s}(x) & g_1 &= \bar{g}_1 + G_1(x) \\ g_s &= \bar{g}_s + G_s(x) & c &= \bar{c} + C(c) \\ y_s &= Y(x) \end{aligned}$$

Substituting into Equations (VI-21 and 22), making use of the AP solution properties, and neglecting products and squares of perturbation quantities, there results

$$\begin{aligned} \frac{1}{2} \left(v'_{F_s} \bar{c} + c'' \bar{Y}_{F_s} \right) &= G_1 Q_{g_1} + v_{F_s} Q_{y_{F_s}} + C Q_c - \bar{Y}'' Y_{F_s} \\ \frac{1}{2} \left[G_1'' \bar{c} + G_s'' \bar{c} + c'' (\bar{g}_s - \bar{g}_1) \right] &= -2q_R \left[G_1 Q_{q_1} + v_{F_s} Q_{y_{F_s}} + C Q_c \right] \\ &+ Y'' (\bar{g}_1 - \bar{g}_s) + (G_1 - G_s) \left(\xi + \frac{1}{c} \right) - \frac{C (\bar{g}_1 - \bar{g}_s)}{c^2} \end{aligned}$$

$$y_{F_s} \left(\xi + \frac{1}{c} \right) = C \bar{Y}_{F_s} / c^2 \quad (VI-23)$$

$$\frac{G_1 - G_s}{c} - \frac{(\bar{g}_1 - \bar{g}_s) C}{c^2} = \bar{\eta} \left[\frac{\partial g}{\partial n} \Big|_{s-} - \frac{\partial \bar{g}}{\partial n} \Big|_{s-} \right]$$

$$y_{F_s} = \frac{\bar{Y}_{F_s} \epsilon_{F_s} G_s}{\bar{g}_s^2}$$

$$y_{F_s}(-\infty) = G_1(-\infty) = G_s(-\infty) = Y'(-\infty) = C(-\infty) = 0$$

Here Q_{g_1} , Q_c and $Q_{Y_{F_s}}$ are partial derivatives of the reaction rate integral which may be numerically evaluated.

Equations (VI-23) require a knowledge of the solid phase behavior through $\partial g / \partial n \Big|_{s-}$. The linearized version of the solid phase equation of Equations (VI-13) is

$$g_{xx} + g_{\eta\eta} - g_{\eta} = Y'' g_{\eta} \quad (VI-24)$$

In order to give sufficient freedom to the solid phase temperature profiles it is suggested from solutions to the homogeneous part of Equation (VI-24) to try

$$g = e^{m_{g_1} \eta} \left[G_0(x) \cos m_{g_2} \eta + G_1(x) \sin m_{g_2} \eta \right] + \bar{g}(\eta)$$

where m_{g_1} and m_{g_2} are constants to be determined. Inserting this assumed form into Equation (VI-24) and integrating over η from 0 to $-\infty$ there results

$$m_{g_2} G_1 + (m_{g_1} - 1) G_0 + \frac{m_{g_1}}{m_{g_1}^2 + m_{g_2}^2} G_0'' + \frac{m_{g_2}}{m_{g_1}^2 + m_{g_2}^2} G_1'' = Y'' (\bar{g}_s - 1) \quad (VI-25)$$

Multiplying Equation (VI-24) by η , substituting in the expression for g and integrating from 0 to $-\infty$ there results a second differential equation for the unknowns G_1 , G_0 and Y' :

$$G_0 \left(\frac{m}{S} g_1 - 1 \right) - G_1 \frac{m}{S} g_2 + \frac{m^2 g_2 - m^2 g_1}{S^2} G_0'' - \frac{2m g_1 g_2}{S^2} G_1'' = -Y''(g_s - 1) \quad (\text{VI-26})$$

$$S = m_{g_1}^2 + m_{g_2}^2$$

Note that at $\eta = 0$, $g_s = G_0 + \bar{g}_s$, so that $G_s = G_0$ and G_0 is not a new unknown. Calculating $\partial g / \partial n|_s$ which is equal to $\partial g / \partial \eta|_s$ to the linear approximation $\partial g / \partial n|_s = \bar{g}_\eta(0) + G_1 m_{g_2} + G_0 m_{g_1}$. Placing this result in the interface energy balance relation of Equations (VI-23) there results from Equations (VI-23, 25 and 26) four differential equations and three algebraic relations for the eight unknowns V_s , C , G_1 , $G_s = G_0$, Y' , G_1 and the two parameters m_{g_1} and m_{g_2} . The underspecification of the problem comes from the two arbitrary parameters m_{g_1} and m_{g_2} rather than specification of one of them. This difficulty will be resolved shortly. Consider for the moment that m_{g_1} and m_{g_2} have been specified; then there would be seven equations for the six field variables. By elimination of variables there could be chosen two independent sets of differential equations. But the equations are homogeneous and would possess solutions, for example, like $G_1 = A_{g_1} e^{mx}$. However, the root(s) m would have to be the same for the two independent sets of equations. This provides the condition for one of the parameters, say m_{g_1} . With two unknown parameters allowable roots would be obtained for a variety of $m_{g_1} = m_{g_1} (m_{g_2})$. This arbitrariness has been purposely introduced because this is a highly approximate technique and physical reasoning may have to be involved to choose the correct parameters.

In any event the procedure is the following: a) G_1'' is eliminated from Equations (VI-25 and 26), b) G_1 is solved for in this result and

placed into the interface energy conservation algebraic condition of Equations (VI-23), c) Y'' is solved for from the interface energy condition and placed in the differential equations of Equations (VI-23), d) the other two algebraic conditions are used in the differential equations of Equations (VI-23) to eliminate G_s and C in favor of V_{F_s} , and e) V_{F_s} is eliminated in favor of G_1 to yield a single fourth order, homogeneous differential equation of the form

$$a_1 G_1'''' + a_2 G_1'' + a_3 G_1 = 0$$

Now the a 's are functions of the AP planar deflagration quantities and m_{ξ_1} and m_{ξ_2} . Setting $G_1 = A_{\xi_1} e^{mx}$ the four roots are

$$m = \pm \sqrt{\frac{-a_2 \pm \sqrt{a_2^2 - 4a_1 a_3}}{2a_1}} \quad (\text{VI-27})$$

A second independent differential equation is formed as follows: a) Y'' is eliminated between Equations (VI-26 and 26), yielding a differential equation in G_0 and G_1 , b) the energy conservation condition at the interface and one of the differential equations developed in step d) above is used to generate another differential equation in G_0 and G_1 , c) these differential equations are combined into a single fourth order differential equation of the form

$$b_1 G_0'''' + b_2 G_0'' + b_3 G_0 = 0$$

where again the b 's are functions of the quantities at $x = -\infty$ and m_{ξ_1} and

m_{g_2} . Letting $G_0 = A_{G_0} e^{mx}$, an equation like Equation (VI-27) is developed with the b's replacing the a's. Since the roots m must be the same for a physically realistic result $m_{g_1} = m_{g_1} (m_{g_2})$, if a solution exists. There is no guarantee, however, that a solution satisfying these conditions may be found. Note that the quantity under the inner square root sign must be positive for m to be real. Although m could be allowed to be complex (not pure imaginary because the solution would not decay to the pure AP solution), a non-unique solution would arise. That is, the conditions developed below for attachment to a binder would be underspecified. It is imperative, therefore, that m be real for a realistic solution to be developed.

A numerical search for m_{g_1} and m_{g_2} to satisfy the requirements yields the surprising but satisfying results that a) m is real and b) solutions exist for only a very narrow range of m_{g_1} and m_{g_2} as seen in Figure VI-2. If $m_{g_1} = 1$, this would correspond to choosing the thermal wave "depth" the same as in the unperturbed case. Note also that $m_{g_1} = 1$ corresponds very nearly to the case when the allowable m_{g_2} becomes single-valued. Having confirmed an expectation that $m_{g_1} = 1$ is a reasonable choice, all further calculations assumed this value for m_{g_1} .

The perturbation solution is valid for A_{g_1} positive or negative; however, the only physically realistic solutions occur for negative A_{g_1} since the binder is a heat sink and will cool the gases of AP deflagration. In the perturbation solution (since the x and y origin is arbitrary) A_{g_1} is set equal to -0.01 at $x = 0$ and all other quantities may be computed from the linear differential equations, knowing m . The results for surface shape at two pressures are shown in Figure VI-3. Also shown are the temperature at the "edge" of the AP flame, the surface mass fraction of NH_3 ,

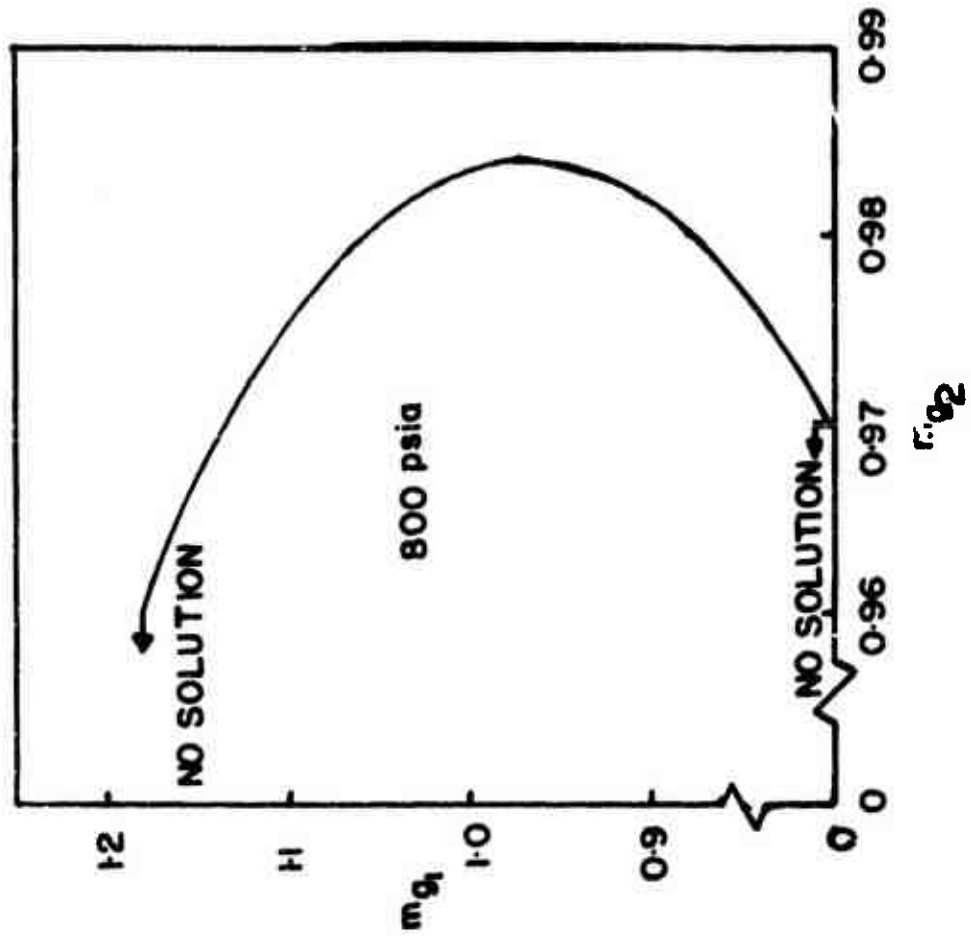


Figure VI-2. Allowable Values of the Solid Phase Temperature Profile Parameters.

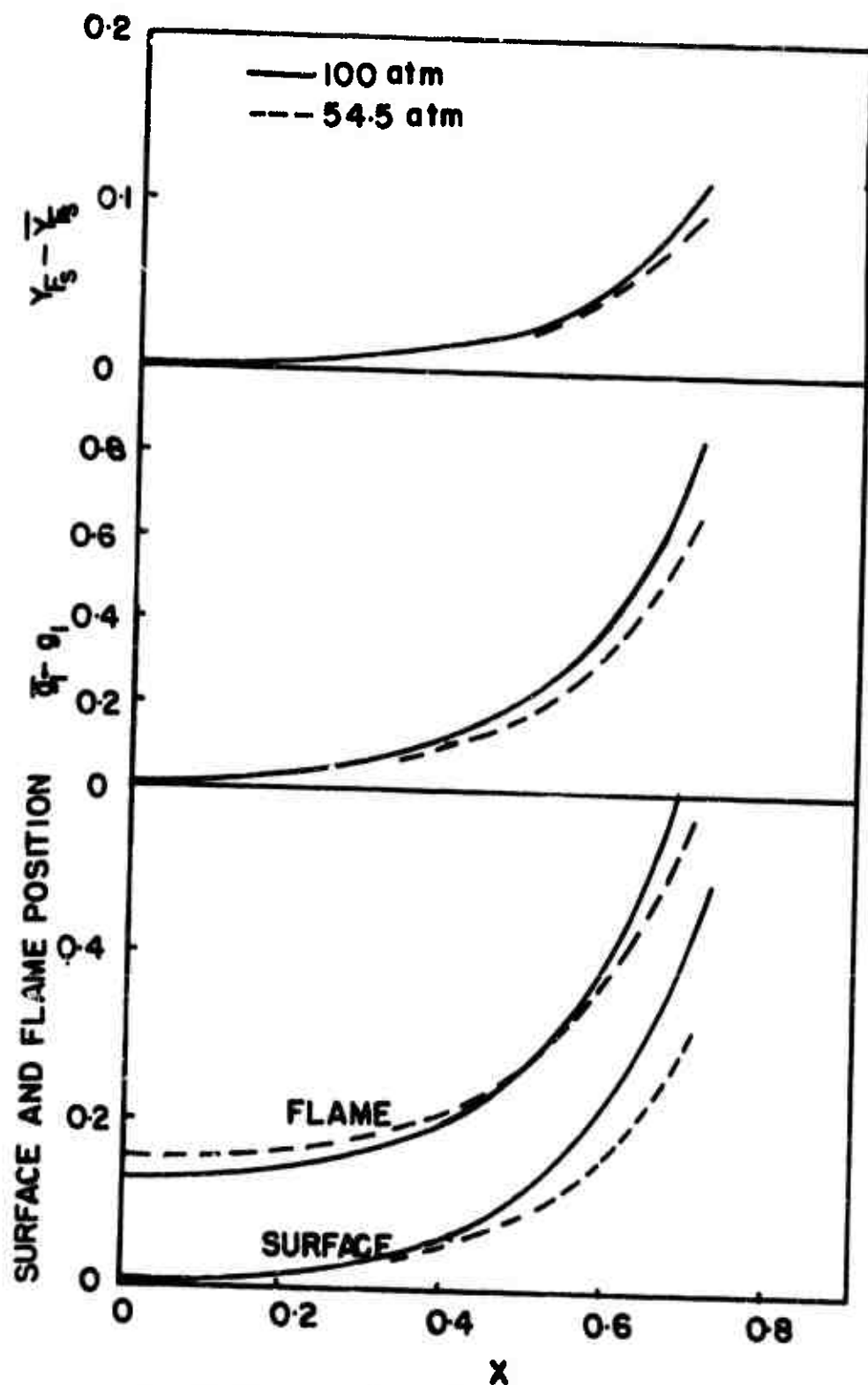


Figure VI-3. Surface, Flame Standoff, Surface NH_3 Mass Fraction and Flame Temperature Profiles.

and the flame height. It is seen that there is very little difference between the two cases when the results are in dimensionless form. The distance scales with which the variables y and x have been made dimensionless are $21 \mu\text{m}$ at 54.4 atm and $15.4 \mu\text{m}$ at 100 atm . Consequently, all surface profile changes are made in a somewhat shorter distance for the higher pressure case. It should also be noted that Y_{F_s} rises as the binder is approached; because of the equilibrium condition at the solid-gas interface this implies the surface temperature is rising as the binder is approached. Therefore, the heat transfer vector component parallel to the interface is toward the AP from the binder. This interesting result implies the maximum solid phase temperature will exist in the binder. It is physically due to the fact that the hot gases from the AP deflagration process sweep past the binder.

The foregoing is an "eigensolution" to the AP problem and is independent of the binder causing the perturbation from a planar regression. However, the location of the binder depends upon the properties of this eigensolution and the physical properties of the binder. A set of matching conditions to locate the binder on Figure VI-3 is now required.

Location of the Binder. At any x position in the eigensolution to the AP problem the heat transfer vector in the gas and solid phases is known. Since this must be a continuous quantity and the temperature is a continuous quantity, but q_s undergoes a discontinuity, there must be a surface slope discontinuity at the binder. In the interface energy conservation relation of Equations (VI-12) the solid and gas phase heat transfer vectors may be computed from the AP solution and this equation

becomes a relation for the binder heat of gasification as a function of its surface slope. The result is

$$q_{s_B} = y_B' G_O' \left(\tilde{\eta} - \frac{1}{\xi} \right) - \tilde{\eta} [m_{g_1} G_O + m_{g_2} G_1 + (\bar{g}_s - 1)] + \frac{(g_1 - g_s)(1 + y_B' y_F')}{c \xi} \quad (\text{VI-28})$$

The pyrolysis condition of Equations (VI-12) gives an additional relation between the surface slope and the binder properties

$$\frac{1}{z_B} = \tilde{b}_B e^{-\epsilon_{s_B} / g_s} \quad (\text{VI-29})$$

At any x position, then, Equations (VI-28 and 29) together with the AP eigensolution define an allowable binder attachment and a functional equation

$$b_B = b_B'(\epsilon_{s_B}, q_{s_B}; x)$$

$$y_B' = y_B'(\epsilon_{s_B}, q_{s_B}; x)$$

For the case of $p = 54.4$ atm these results are shown in Figures VI-4 and 5 for two values of ϵ_{s_B} which correspond closely to HTPB and CTPB binders ⁽¹¹⁾. Also, knowing q_s and b_B for HTPB and CTPB ⁽¹¹⁾ the actual point at which these two binders would attach is shown on Figures VI-4 and 5. There are several points worthy of note. First, for these binders, the x position of compatibility with the AP solution occurs where very little change

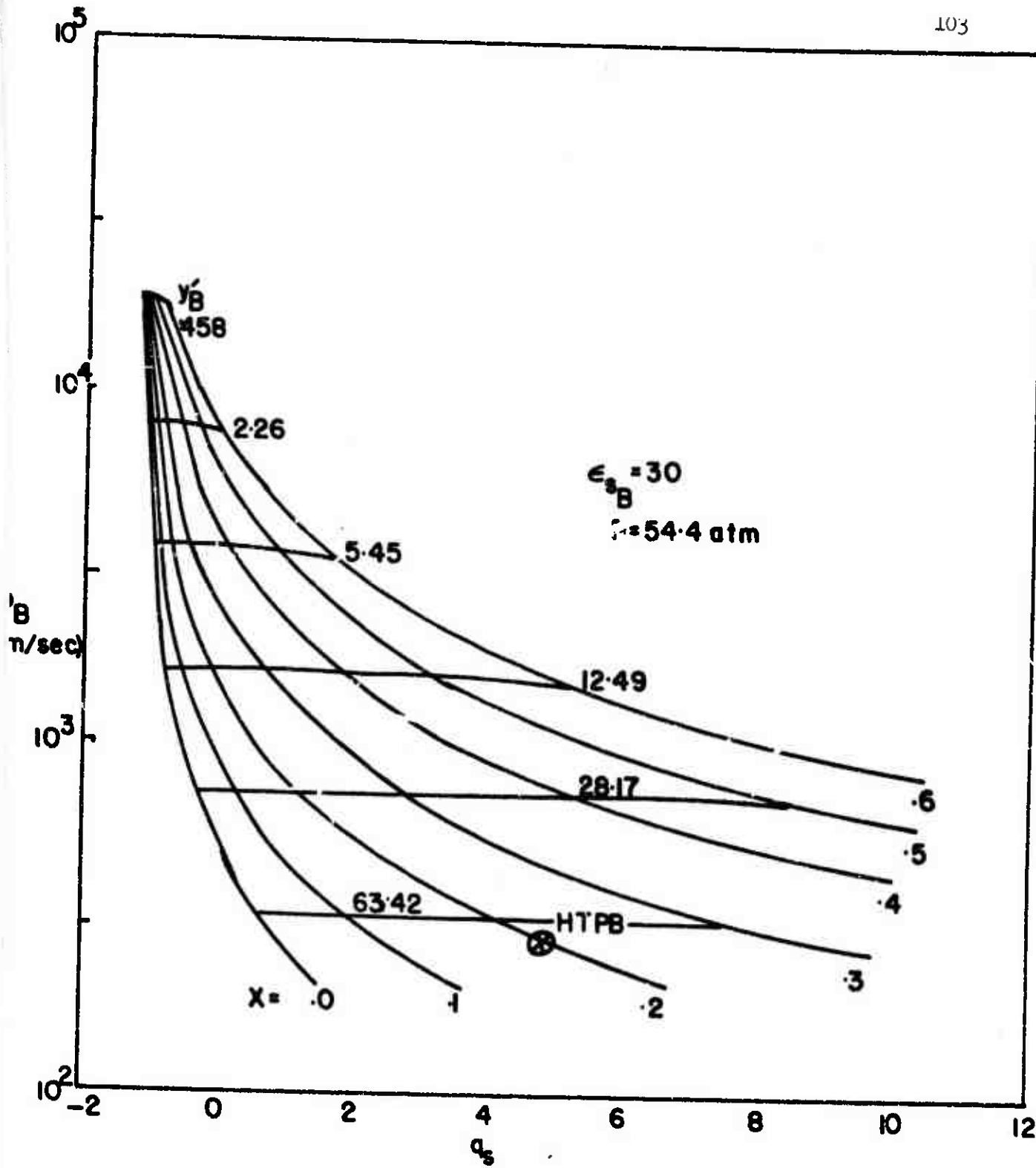


Figure VI-4. Binder Properties for Attachment to the AP Solution -
 $p = 54.4 \text{ atm}$, $\epsilon_{sB} = 15$.

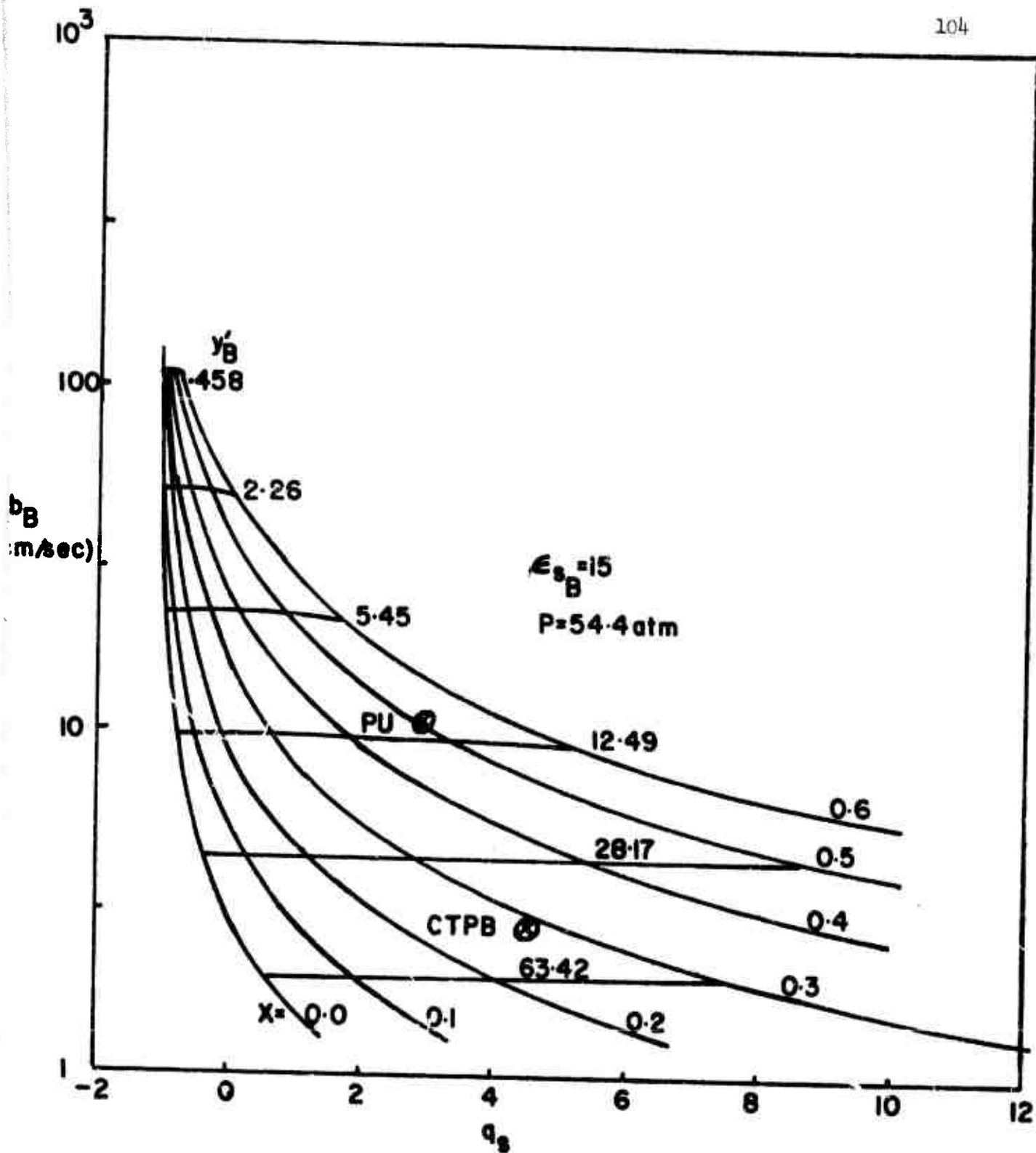


Figure VI-5. Binder Properties for Attachment to the AP Solution - $P = 54.4 \text{ atm}$, $\epsilon_{sB} = 30$.

from a flat AP surface has taken place. Consequently, the linear AP eigensolution can be used with confidence as a good approximation to the solution of the nonlinear problem. Polyurethane, shown on Figure VI-4, would however attach in a region of reasonable surface slope and there is question concerning the adequacy of the solution. Fluorocarbon binder as used in Reference (11) would attach to the left of $x = 0$, or in a virtually flat region. The second point is that the values of y_B' are extremely high for all binders so that the slope would appear nearly vertical. This is the primary information desired, in addition to the AP surface profile, so no attempt is made to continue the solution to find the binder profile.

Shown on Figure VI-6 are the results for $p = 100$ atm for a surface activation energy $e_{s_B} = 30$. Noting the HTPB point, there would be virtually no visible distinction between the result at 100 atm and that at 54.4 atm.

Discussion of Results

A solution has been obtained for the shape of the deflagrating AP surface when it is adjacent to an inert binder. Except for selected binders there would be very little visible effect of the binder upon the surface shape and the result is virtually independent of pressure. The distance scale over which a visible transition would take place from planar AP to the binder is of the order of microns. The current theory assumes a dry binder; it is known, however, that binder melt flows exist for all binders tested heretofore in the sandwich configuration and that these melt flows run several hundred microns onto the AP surface. Consequently, none of the predicted phenomena are capable of being observed. A theory including the effects of melt flows is necessary.

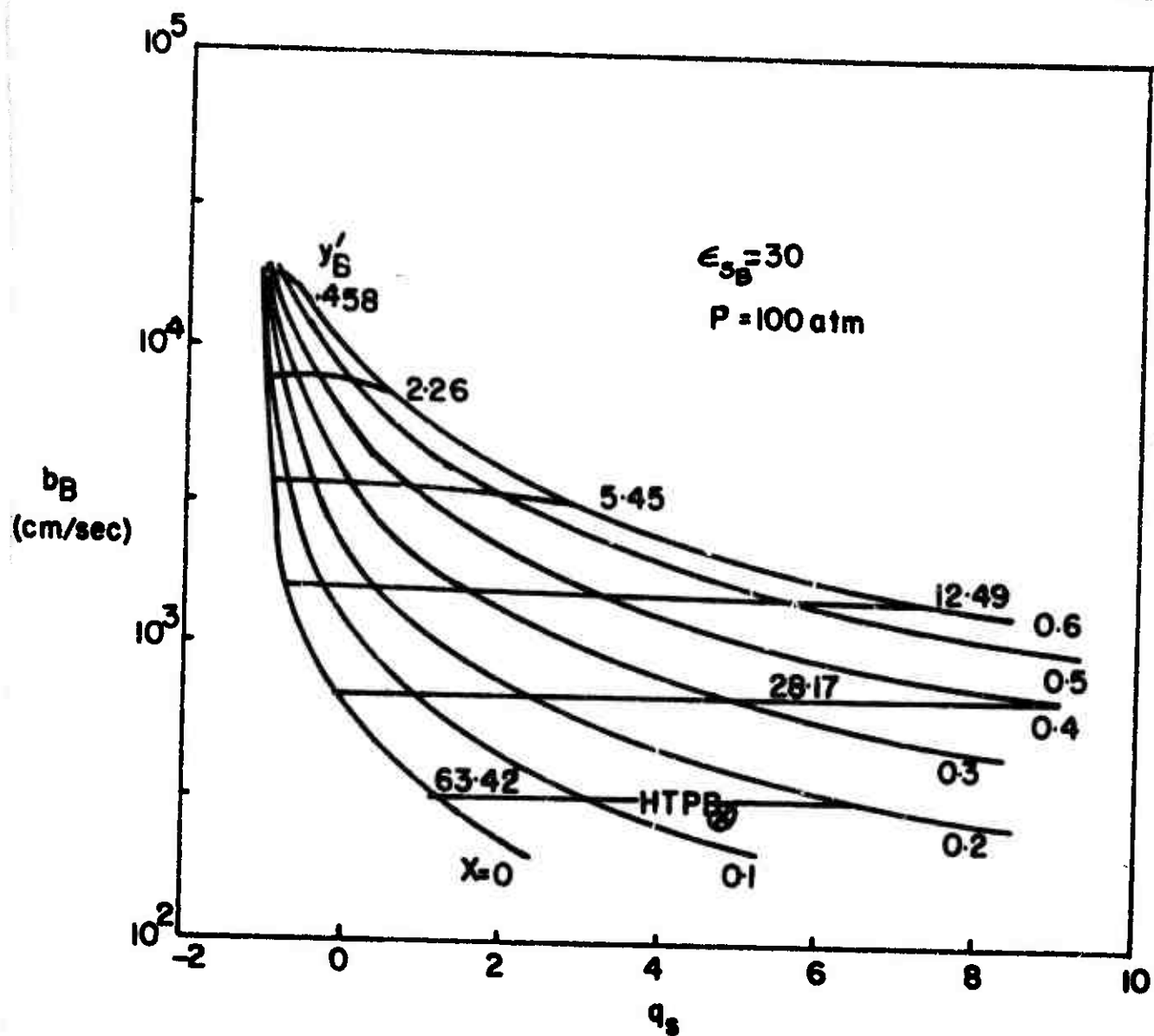


Figure VI-6. Binder Properties for Attachment to the AP Solution -
 $p = 100 \text{ atm}$, $\epsilon_{sB} = 30$.

The theory predicts, however, that if the melts do not occur there should be a sharp discontinuity in slope at the binder-oxidizer interface. This has recently been seen for catalyzed sandwiches (Section III) for which the melt extent is markedly reduced (for unknown reasons). Although the current theory is not directly applicable to catalyzed situations the interface conditions responsible for the slope discontinuity are applicable. It appears that melt flows dominate the development of the surface shape if melts occur.

The current theory points to the fact that the surface temperature should increase as the binder is approached and the maximum solid phase temperature should occur in the binder. This might account for the appearance of "notches" in the binder, sometimes seen on quenched samples (e.g., see Figure III-30). The violence of the quenching process may eject the part of the binder above a surface of a prescribed strength level, which should be temperature sensitive. A rough sketch of isotherms near the interface should convince the reader that a weak binder may exist locally near the binder-AP interface.

The current analysis shows a very weak dependence of surface shape upon pressure. This independence has been observed experimentally, but the comparison between theory and experiment cannot be made precisely because binder melts have occurred in all the experiments.

The present theory contains no eigenvalue because the deflagration rate is determined by the AP deflagration process. If the binder were reactive, however, as occurs in catalyzed sandwiches, the burn rate must become an eigenvalue of the problem. It is not clear at this point how

this will enter the solution to the problem. Current analysis centers about this problem and the incorporation of binder melts into the solution.

SYMBOLS FOR SECTION VI

b	pyrolysis law constant or vapor pressure constant
\tilde{b}	dimensionless pyrolysis law constant or vapor pressure constant
c_s	solid phase specific heat
c_p	specific heat at constant pressure for gas phase
c	flame standoff distance
C	deviation of c from planar AP case
E	activation energy
g	T/T_0
G	deviation of temperature from planar AP case
G_0, G_1	solid phase temperature perturbation functions
k	preexponential factor in reaction rate law
\tilde{k}	dimensionless preexponential factor in reaction rate law
m, m_1, m_2	constants in eigensolution
n	coordinate normal to the solid-gas interface directed toward the gas phase
P	pressure
Q	reaction integral defined by Equations (VI-17)
q	exothermic reaction heat
R	universal gas constant
Re	Reynolds number
r, r_n	burn rate and regression rate normal to surface, respectively
T	temperature
v	gas velocity in y direction
w_F	production rate of NH_3

x, y	coordinates
Y	perturbed y position of solid surface
Y_k	mass fraction of species k
y	deviation of mass fraction from planar AP case
z	$\sqrt{1 + (dy_s/dx)^2}$
α	thermal diffusivity, $\lambda/\rho c$
ϵ	dimensionless activation energy, E/RT
η	c_s/c_p
λ	thermal conductivity
ξ	$c_p \lambda_s / c_s \lambda_g$
ρ	density

Subscripts

B	binder
f	flame temperature
F	NH_3
g	gas phase
o	cold solid
s	solid phase or surface
l	quantity evaluated at flame standoff position

Subscript by independent variable denotes partial differentiation with respect to that variable

Superscripts

$-$	quantity evaluated for the one-dimensional AP deflagration
$'$	ordinary derivative with respect to x

VII. CONCLUSIONS

1. Depending upon the catalyst type there are different degrees of catalysis or inhibition upon the AP deflagration rate and the reactions between the oxidizer and binder. Generally the copper compounds in CuO_2O_2 have a greater catalytic effect upon the AP deflagration rate than do the iron compounds, which often inhibit the AP rate, but the iron compounds appear to have a stronger catalytic effect upon the binder-oxidizer reactions.

2. A significant discovery of this program is the apparent removal or inhibition of the binder melt flow when catalysts are present. While the mechanism of removal is not certain, the melt removal alone may be an important "catalytic" mechanism in the augmentation of deflagration rate.

3. In an uncatalyzed state the binder is effectively an inert substance which inhibits the AP deflagration rate by acting as a heat sink and a source of a melt flow; when the catalysts are present, however, the reactions between the binder and oxidizer become sufficiently fast that heat feedback from these reactions augment the deflagration rate. The most effective placement of the catalyst, to produce this effect, is in the oxidizer, suggesting that the catalytic reactions take place away from the binder surface, whether the actual catalytic reactions are heterogeneous or not, and that the catalytic reactions prefer high temperatures.

4. In the pressure range 600-2000 psia there is very little change in catalytic mechanisms or overall sandwich deflagration behavior with a pressure variation. There is, of course, a general increase in rate of various rate processes with pressure and iron oxide changes from an inhibitor to an augmentor of the AP deflagration rate at about 1200 psia.

5. The surface structure of AP during deflagration changes markedly when catalysts are present, suggesting that alteration of condensed phase reactions may take place in the AP. Electron microprobe studies with iron blue in AP were inconclusive but suggested that iron is removed from the catalyst in the vicinity of the condensed phase surface at a faster rate than other elements.

6. At low pressures (<800 psia) iron blue and ferrocene appear to have a catalytic effect when placed into the binder, which is an effect not seen at higher pressures and with other catalysts. Consequently, the low pressure region should be explored in detail.

7. While it is possible to draw certain conclusions concerning real propellant results from the sandwich experiments with catalysts, especially with regard to pressure and AP particle size effects, there is uncertainty concerning the relative importance of AP catalysis and binder-oxidizer reaction catalysis in a real propellant. The results of this program are able to predict the near-equivalence of ferrocene and iron oxide in propellants, but there is uncertainty as to a comparison of the iron and copper compounds.

8. Regardless of the catalyst it should be most effective in a real propellant if it is a) loaded into the oxidizer, b) operated at high pressure and c) present in a propellant with small AP particle size (high specific area of the AP).

9. Analysis of the sandwich configuration for the case of no binder melt flows and negligible rate of the binder oxidizer kinetics has yielded an explanation for the following observed experimental facts: a) the sandwich shape for uncatalyzed cases should be pressure independent over the

range 20-100 atm; b) there should be very little distinction between the surface shapes for CTPB and HTPB binders, and c) in the case where melts are removed there should be a discontinuity in slope at the binder-oxidizer interface. Furthermore, the maximum condensed phase temperature should exist in the binder which may explain some interesting binder shapes, experimentally observed, caused by binder ejection during the quench process.

REFERENCES

1. Strahle, W. C., Handley, J. C. and Milkie, T. T., "Catalytic Effects in the Combustion of AP-HTPB Sandwiches to 3200 psia," AIAA Paper No. 72-1120 (1972).
2. Jones, H. E. and Strahle, W. C., "The Effects of Copper Chromite and Iron Oxide Catalysts on AP/CTPB Sandwiches," Fourteenth (International) Symposium on Combustion, The Combustion Institute, Pittsburgh (1973).
3. Hightower, J. D. and Price, E. W., "Experimental Studies Relating to the Combustion Mechanism of Composite Propellants," Astronautica Acta, 14, 11-21 (1968).
4. Varney, A. M. and Strahle, W. C., "Experimental Combustion Studies of Two-Dimensional Ammonium Perchlorate-Binder Sandwiches," Combustion Science and Technology, 4, 197-208 (1972).
5. Boggs, T. L. and Zurn, T. E., "The Deflagration of Ammonium Perchlorate-Polymeric Binder Sandwich Models," Combustion Science and Technology, 4, 279-292 (1972).
6. Boggs, T. L., "The Deflagration of Pure Single Crystals of Ammonium Perchlorate," AIAA Paper No. 69-142 (1969).
7. Friedman, R., Nugent, R. G., Rumbel, K. E. and Scurlock, A. C., "Deflagration of Ammonium Perchlorate," Sixth Symposium (International) on Combustion, Reinhold, New York (1957), pp. 612-618.
8. Lyles, B. J., Letter to W. C. Strahle dated 22 September 1972, Thiokol Chemical Corporation, Bristol, Pennsylvania.
9. Guirao, C. and Williams, F. A., "A Model for Ammonium Perchlorate Deflagration Between 20 and 100 atm," AIAA Journal 9, 1345-1356 (1971).
10. Williams, F. A., Combustion Theory, Addison-Wesley, Reading (1965), p. 39.
11. Cohen, N. S., Fleming, R. W. and Derr, R. L., "Role of Binder in Solid Propellant Combustion," AIAA Paper No. 72-1121 (1972).

APPENDIX A

CATALYSTS LOCATED AT THE BINDER-OXIDIZER INTERFACE

The samples for this phase of the investigation were prepared by adding a mixture of 2% AP and 2% catalyst (by weight) to the surface of a lightly pressed AP disk. This composite disk of catalyst and AP was then subjected to the normal disk and sample preparation procedure⁽¹⁾. This narrow-band "interface" catalyst layer adhered well to both the binder and oxidizer. A series of 7 triple sandwiches, each containing two interface disks, is shown in Figures A-1 through 27. The results are summarized in Table A-1. The samples with CC, IB and F at the interface did not consistently exhibit continuous surface slopes at the binder-catalyst-oxidizer interface.

Table A-1

Summary of Results from Scanning Electron Microscopy of Catalyst Located at Binder-Oxidizer Interface

Catalyst	Pressure psia	Figure No. A-	Binder Melt μm	Binder-Catalyst-Oxidizer Interface
CuO2O2	600	1,2,3	none	additional porous material at point of max regression, AP surface smooth.
	1000	5,6	none	uneven burn, porous material at interface, AP surface smooth for 300 μm from interface.
	1500	8,9,10	none	uneven burn, small amount of material at interface, AP surface smooth for 100 μm from interface.
	2000	13,14		same as above.

Table A-1 (Continued)

Catalyst	Pressure psia	Figure No. A-	Binder Melt μ m	Binder-Catalyst-Oxidizer Interface
IO	600	1,4	<50	porous structure visible, continuous interface slope.
	1000	5,7	75	porous structure visible, continuous interface slope.
	1500	8,11,12	20	porous structure visible, continuous interface slope.
	2000	13,15	none	porous structure visible, discontinuous interface slope.
F	600	16,17	200	continuous interface.
	1000	19,20,21	175	continuous interface, bubble.
	2000	24,25,26	50	porous structure at interface, uneven burn.
IB	600	16,18	none	porous material at interface.
	1000	19,22,23	none	porous material at interface, uneven burn.
	2000	24,27	30	porous material at interface, uneven burn.

In most cases this was due to the additional porous or frothy material extending above the leading edge of regression and separated from the solidified HTPB. Some samples exhibited pockets of localized combustion. These were usually noted when several attempts were made to obtain a quenched sample. The delay times for the depressurization were not consistent with the results from the cinephotomacrography. The non-uniformity of the burns was also not expected after viewing the high speed movies.

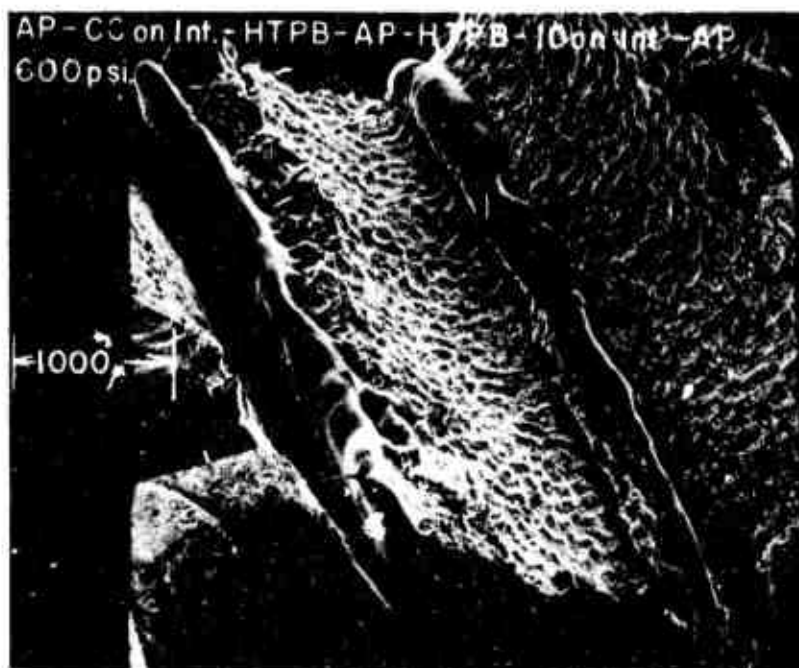


Figure A-1. AP-CC on Int.-HTPB-AP-HTPB-IO on Int.-AP 600 psia (x23).



Figure A-2. AP-CC on Int.-HTPB 600 psia (x105).

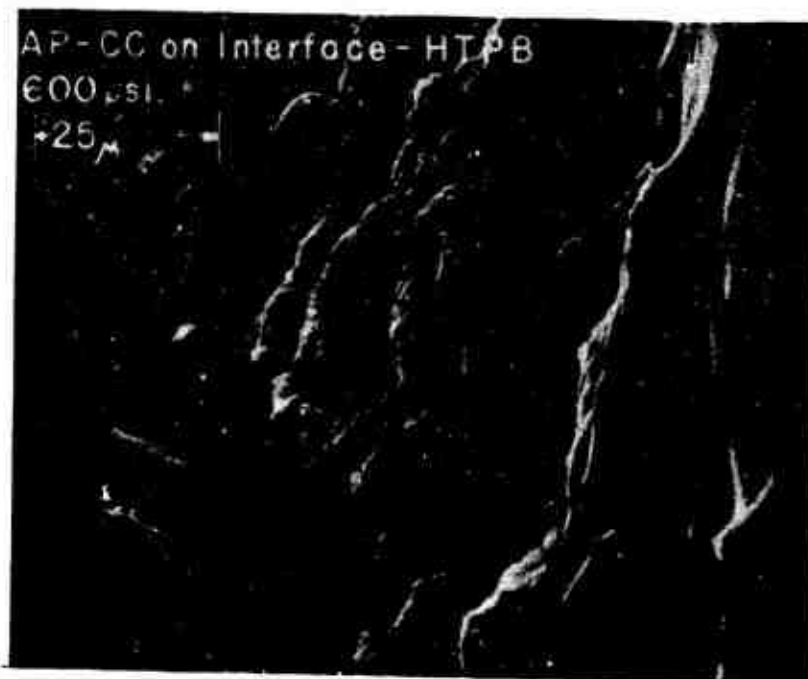


Figure A-3. AP-CC on Int.-HTPB 600 psis (x1050).

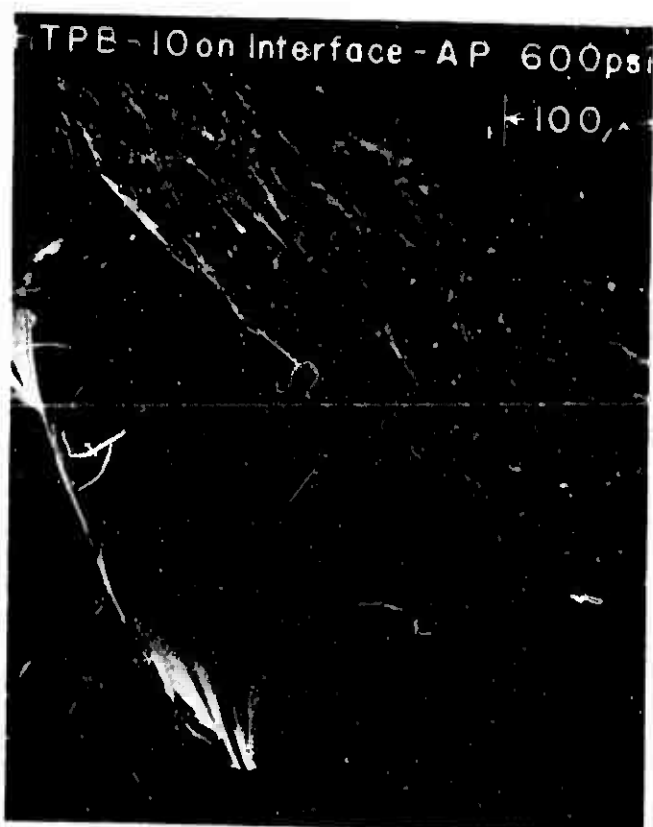


Figure A-4. AP-HTPB-IO on Int.-AP 600 psis (x225).

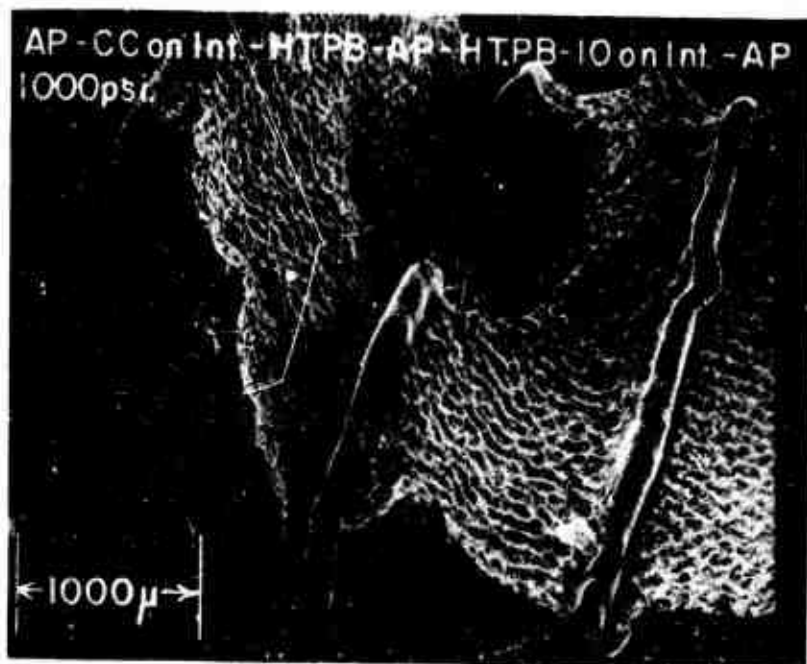


Figure A-5. AP-CC on Int.-HTPB-AP-HTPB-IO on Int.-AP 1000 psia (x26).

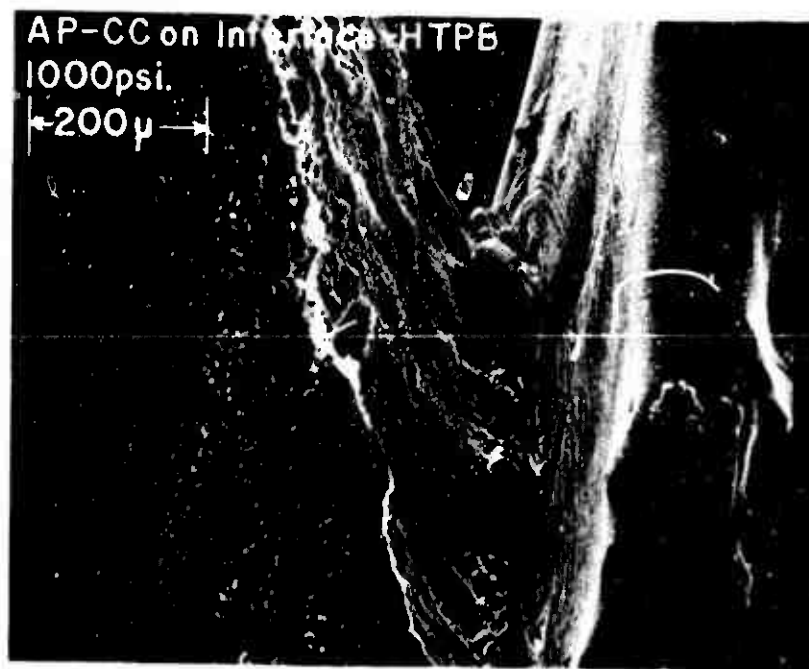


Figure A-6. AP-CC on Int.-HTPB 1000 psia (x125).

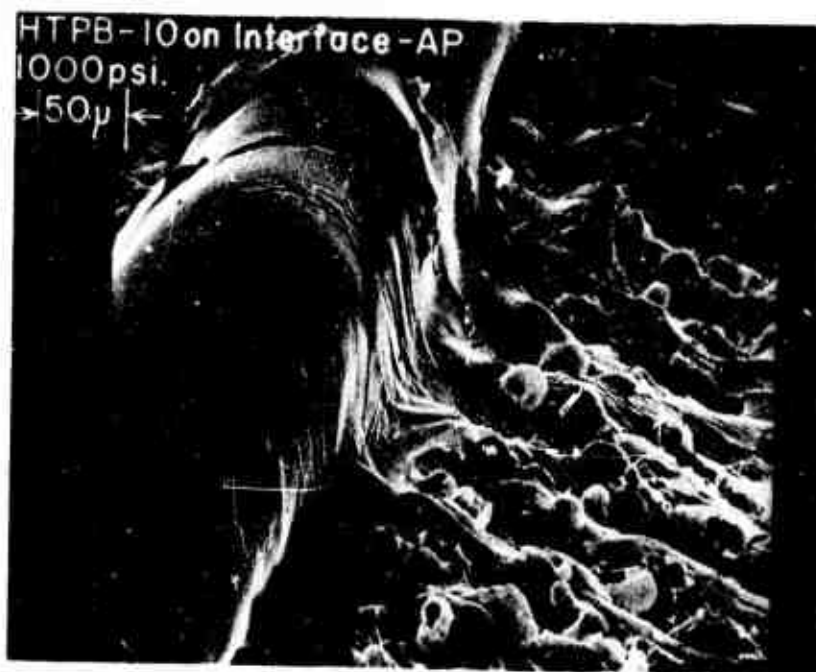


Figure A-7. HTPB-10 on Int.-AP 1000 psia (x250).

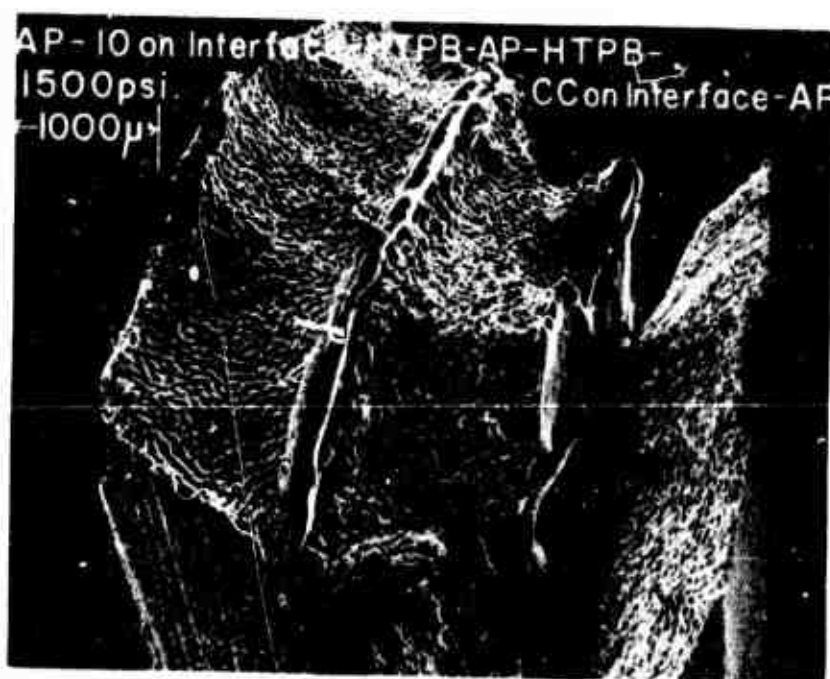


Figure A-8. AP-10 on Int.-HTPB-AP-HTPB-CC on Int.-AP 1500 psia (x20.4).

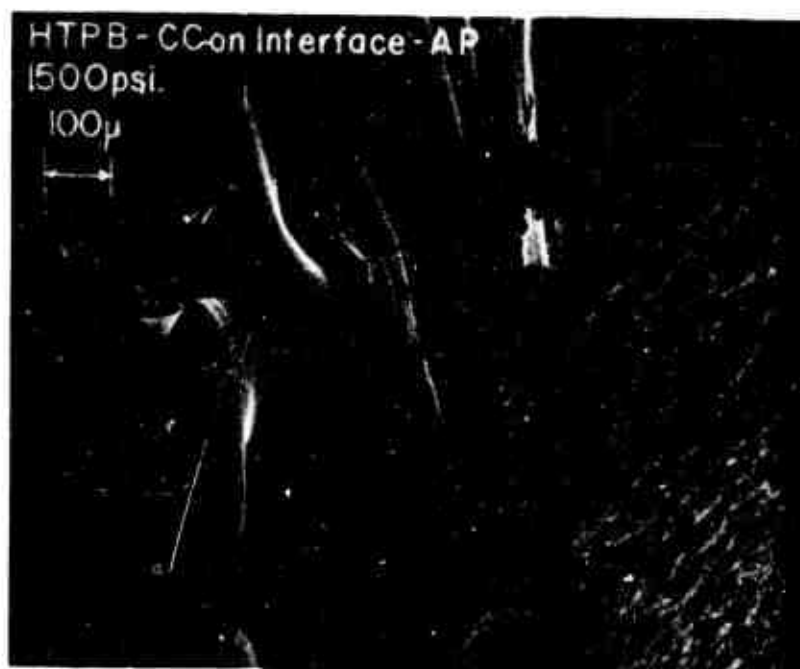


Figure A-9. HTPB-CC on Int.-AP 1500 psia (x90).



Figure A-10. HTPB-CC on Int.-AP 1500 psia (x273).

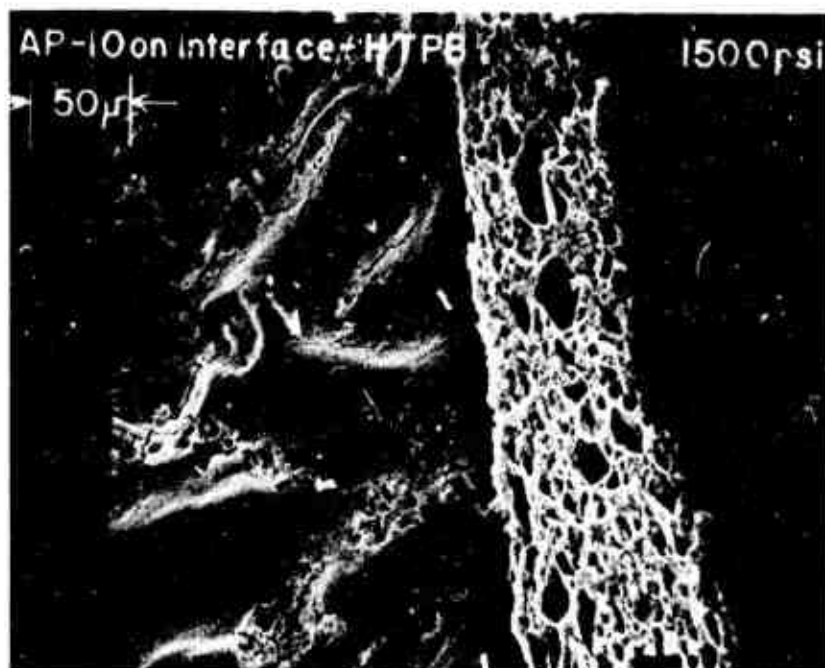


Figure A-11. AP-10 on Int.-HTPB 1500 psia (x280).

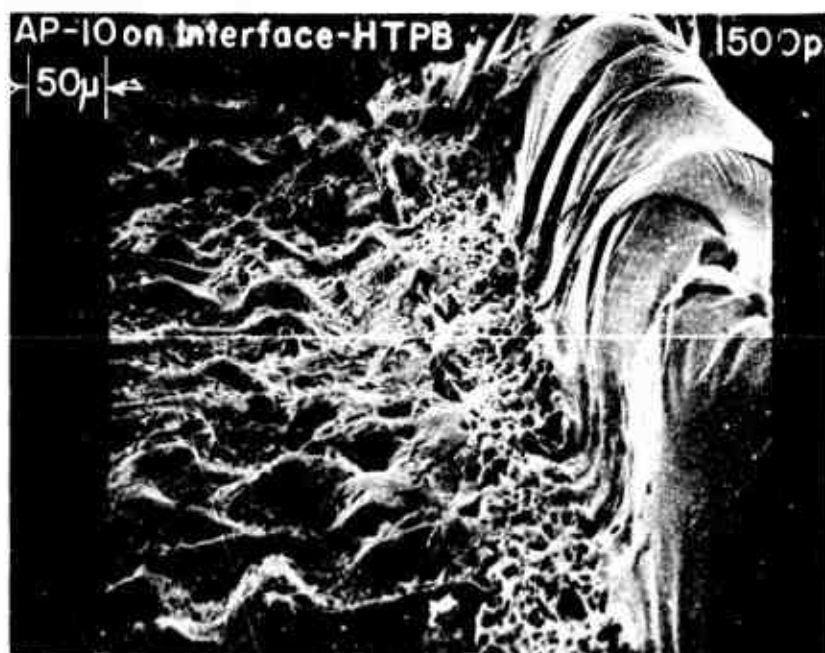


Figure A-12. AP-10 on Int.-HTPB 1500 psia (x228).

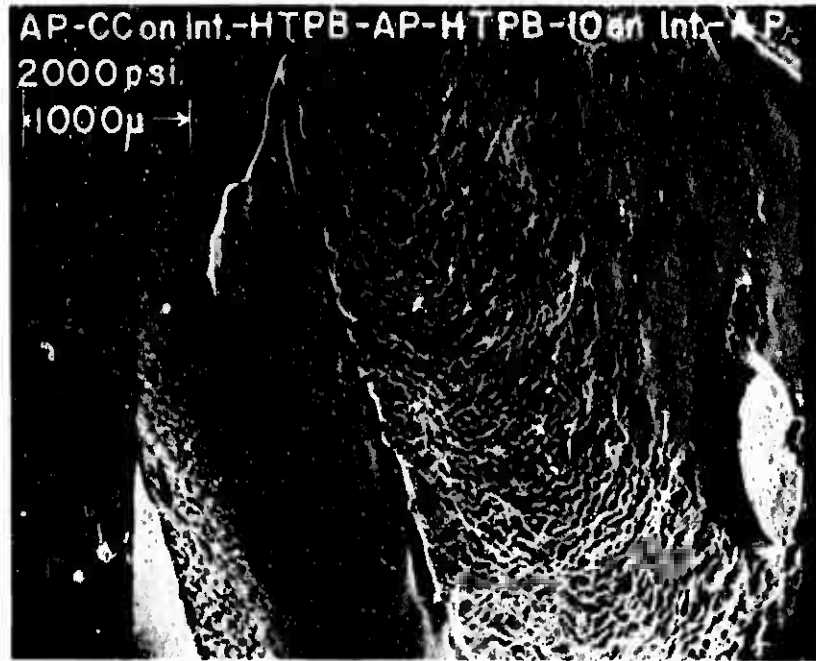


Figure A-13. AP-CC on Int.-HTPB-IO on Int.-AP
2000 psia (x23.5).

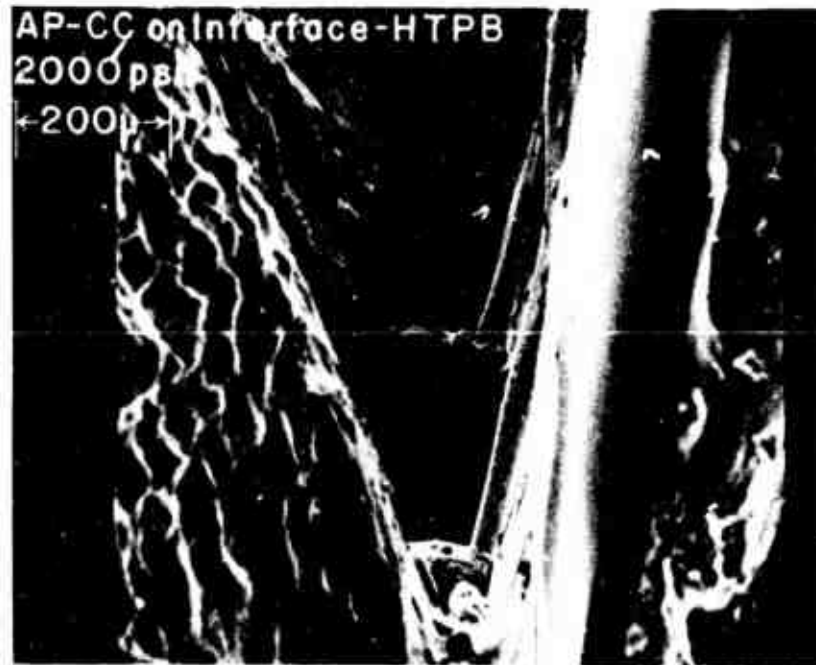


Figure A-14. AP-CC on Int.-HTPB 2000 psia (x108).

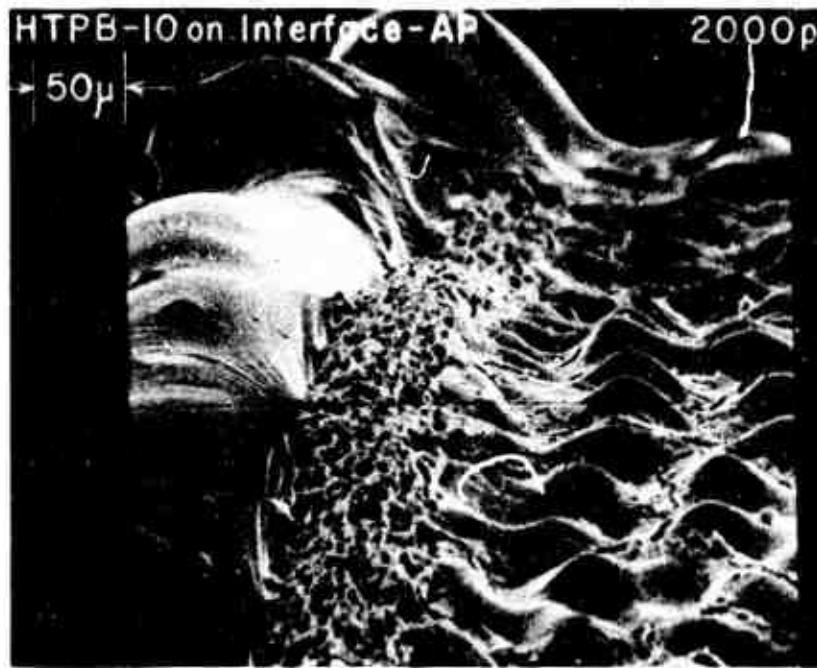


Figure A-15. HTPB-10 on Int.-AP 2000 psia (x260).

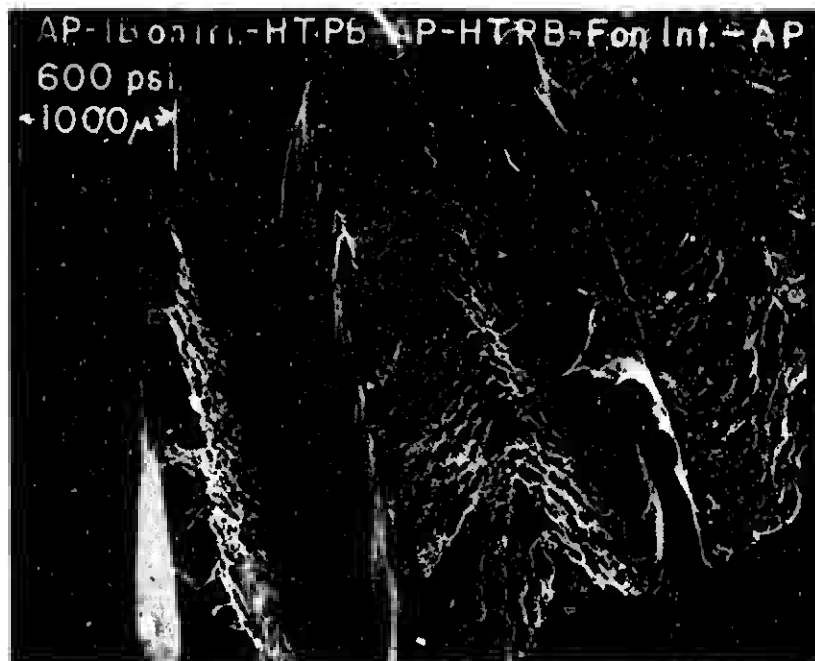


Figure A-16. AP-IB on Int.-HTPB-AP-HTPB-F on Int.-AP
600 psia (x22).

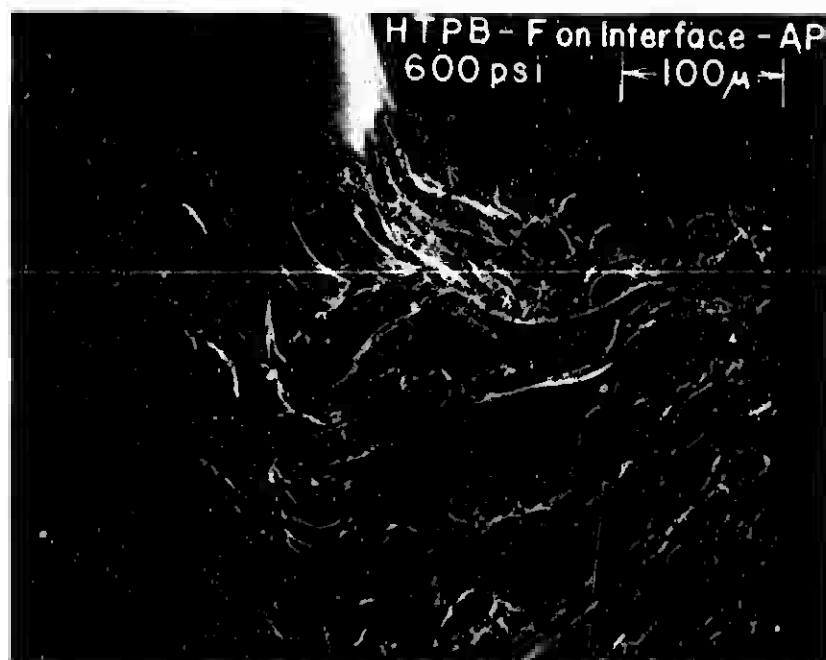


Figure A-17. HTPB-F on Int.-AP 600 psia (x225).

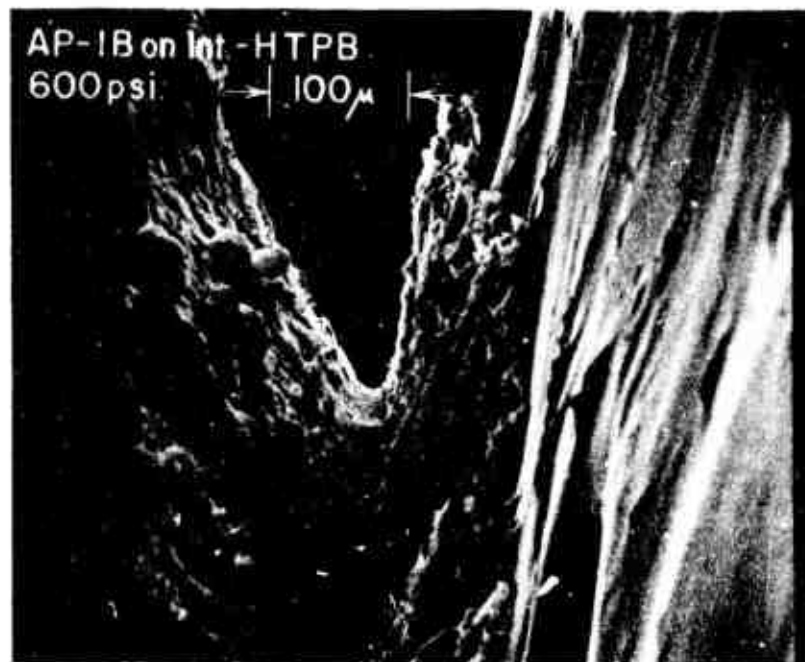


Figure A-18. AP-IB on Int.-HTPB 600 psia (x195).

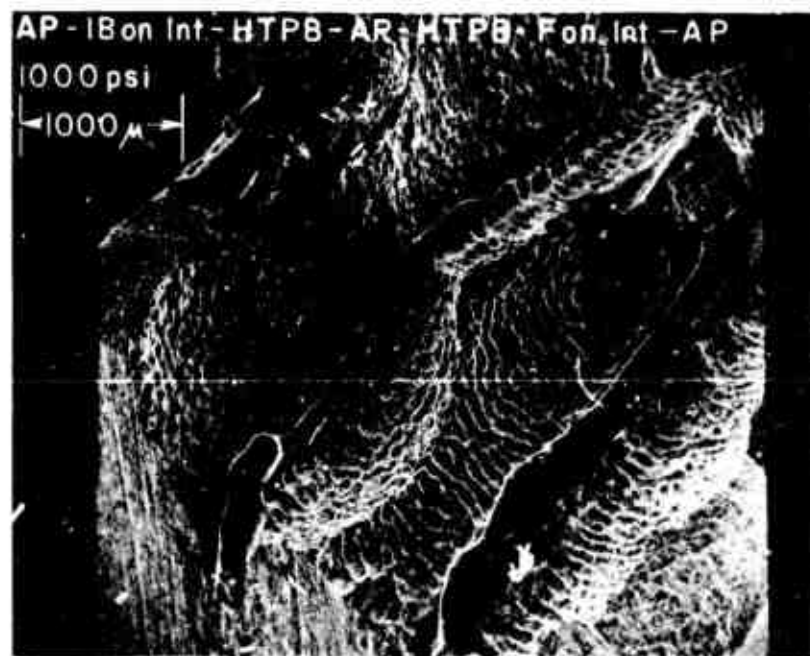


Figure A-19. AP-IB on Int.-HTPB-AP-HTPB-F on Int.-AP 1000 psia (x23).

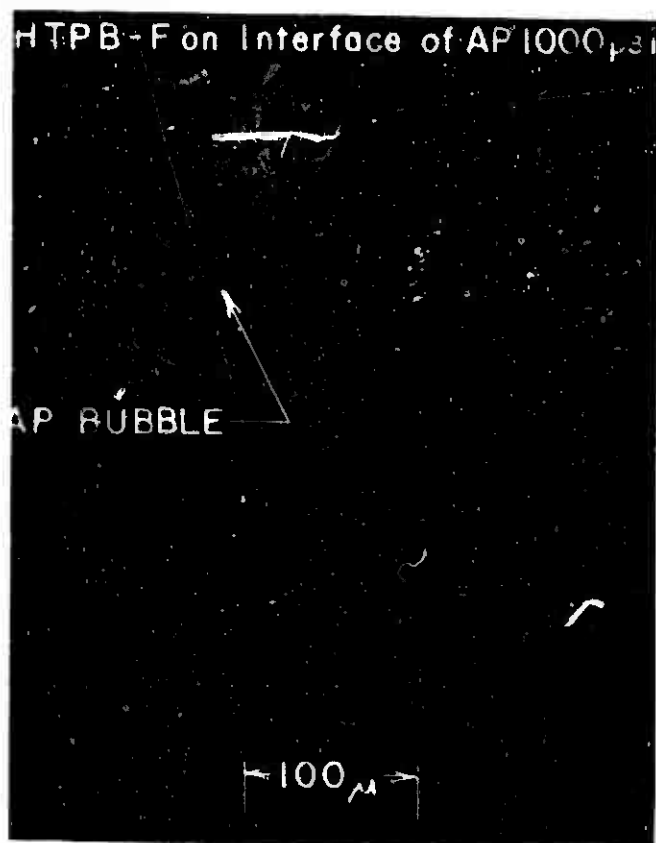


Figure A-20. HTPB-F on Int.-AP 1000 psia (x240).



Figure A-21. HTPB-F on Int.-AP 1000 psia (x1200).

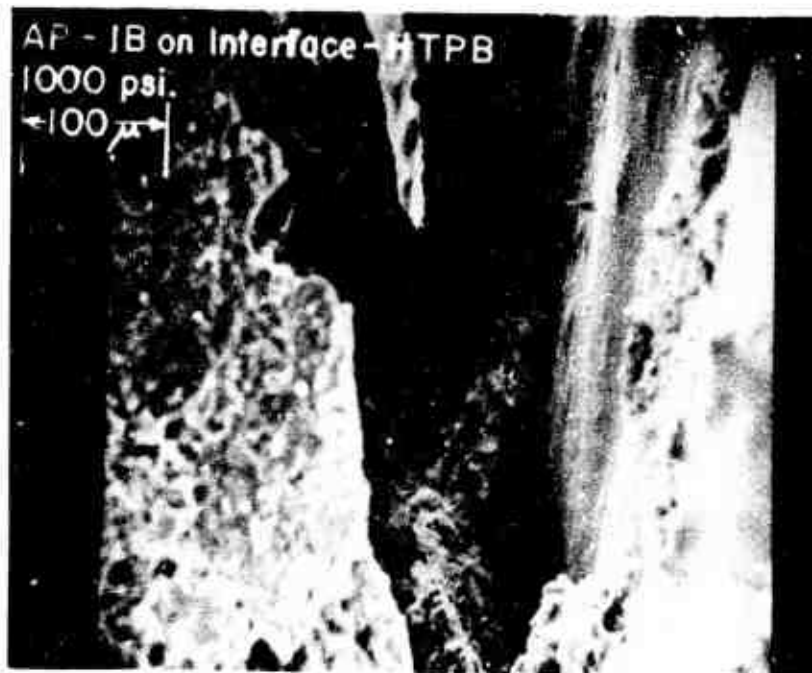


Figure A-22. AP-IB on Int.-HTPB 1000 psia (x208).

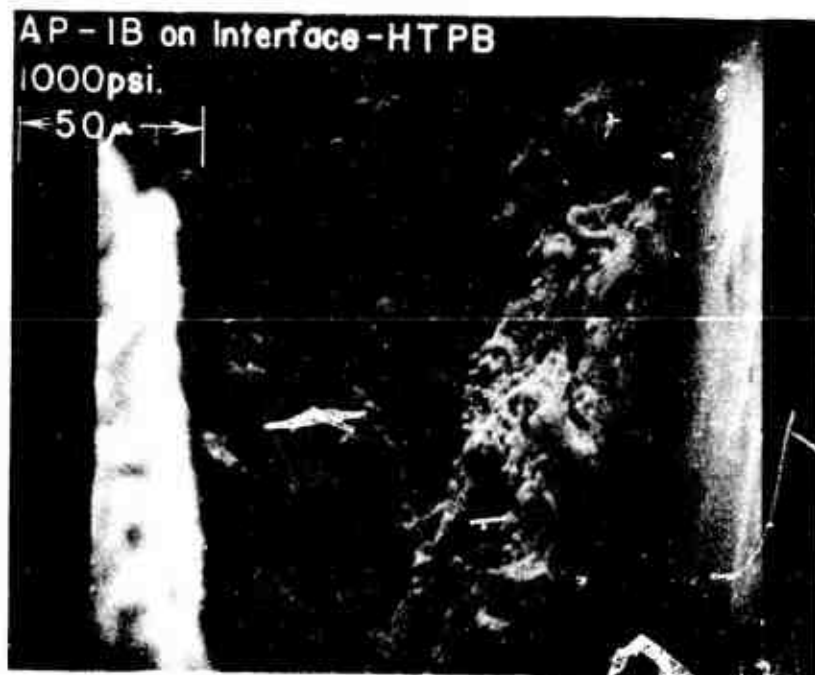


Figure A-23. AP-IB on Int.-HTPB 1000 psia (x20).

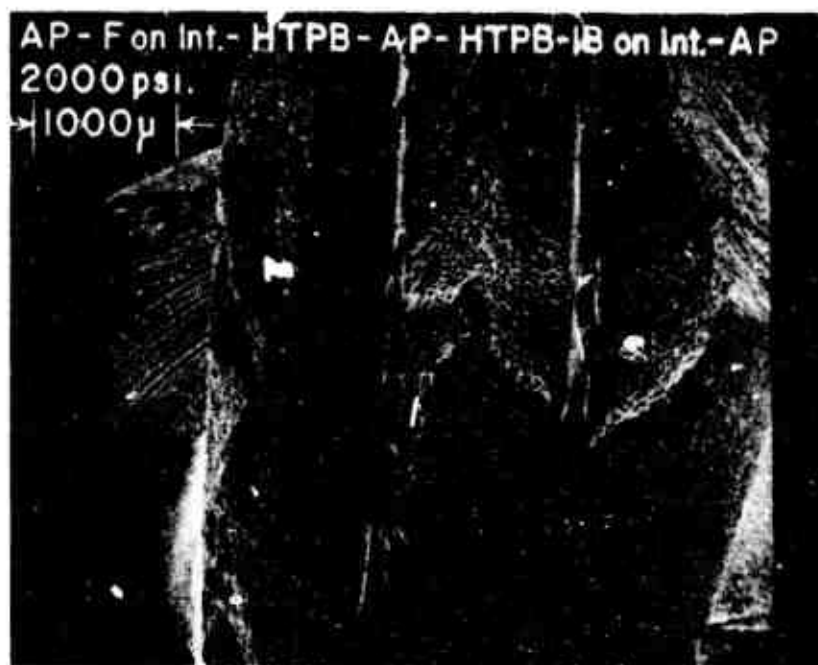


Figure A-24. AP-F on Int.-HTPB-AP-HTPB-IB on Int.-AP 2000 psia (x20.4).

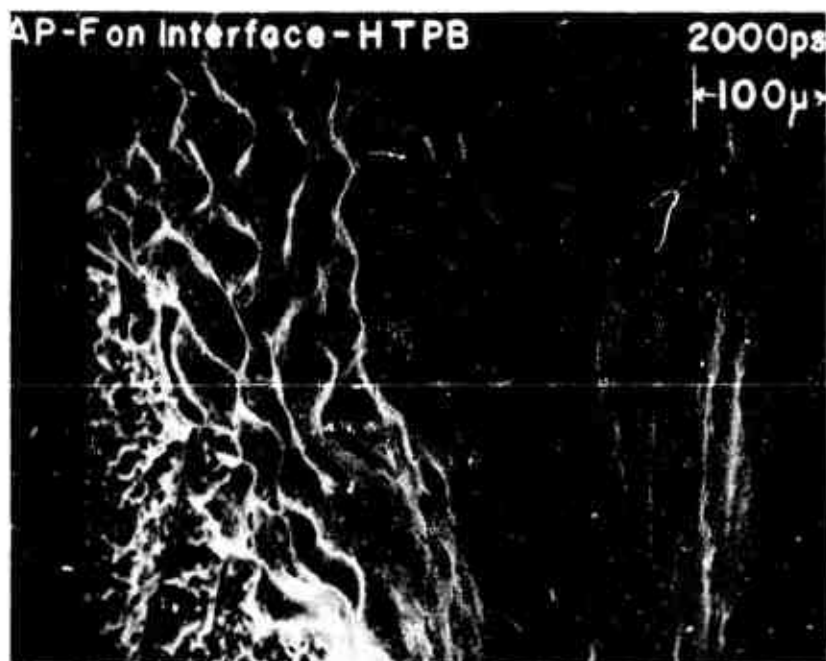


Figure A-25. AP-F on Int.-HTPB 2000 psia (x187).

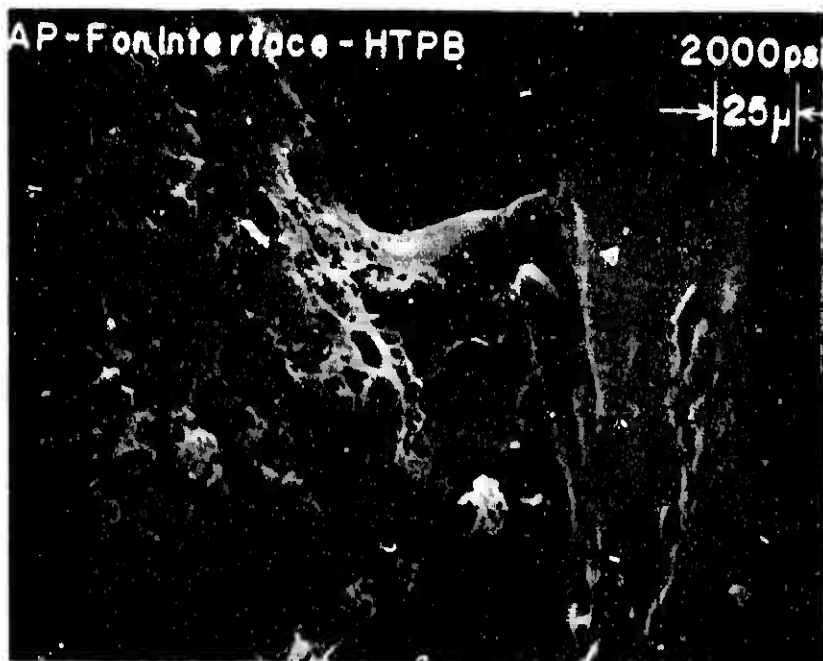


Figure A-26. AP-F on Int.-HTPB 2000 psia (x450).

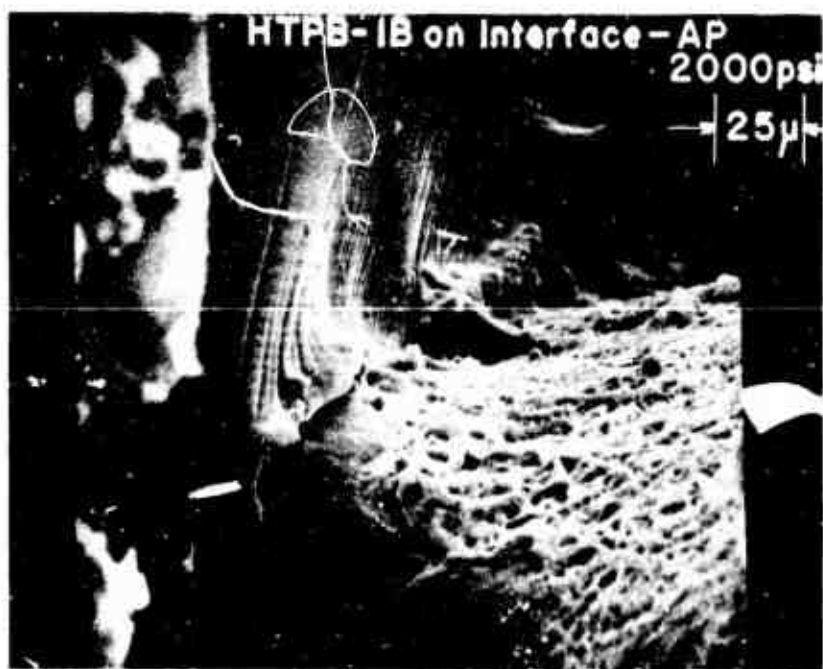


Figure A-27. HTPB-IB on Int.-AP 2000 psia (x484).